Master of Science Thesis

Characteristics of flow through orifices in pipes

An experimental investigation

Vinod Anantharaman

24th September, 2014

Faculty of Aerospace Engineering

Delft University of Technology

Characteristics of flow through orifices in pipes

An experimental investigation

Master of Science Thesis

For obtaining the degree of Master of Science in Aerospace Engineering at Delft University of Technology

Vinod Anantharaman

24th September, 2014

Faculty of Aerospace Engineering · Delft University of Technology

Delft University of Technology

Delft University Of Technology
Faculty of Aerospace Engineering
Department of Aerodynamics

The undersigned hereby certify that they have read and recommend to the Faculty of Aerospace Engineering for acceptance a thesis entitled **“Characteristics of flow through orifices in pipes”** by **Vinod Anantharaman** in partial fulfillment of the requirements for the degree of **Master of Science**.

Dated: 24th September, 2014

Prof. Dr. F. Scarano

Dr. Ir. B.W. van Oudheusden

Dr. N.P. Waterson

Dr. D. Ragni

M. Perçin, MSc.

Abstract

Orifice plates are key components used for flow measurement and control in several industries. For instance, they find applications in gas and liquid circuits of lithography machines, nuclear power plants and aerospace propulsion systems. They are used typically either for measuring flow-rate or to introduce a pressure drop for purposes of flow balancing. The present study focuses on the latter application.

It is widely acknowledged in literature, that the turbulent, unsteady nature of the flow issuing through an orifice can also be a source of structural vibration. In order to understand the nature of the vibration source, the present experimental investigations analyze the time-varying flow field by means of unsteady wall-pressure measurements and time-resolved, planar, particle-image-velocimetry (PIV).

In addition to understanding the dynamics of the flow through a single-hole orifice, this study has assessed the possibility of using multiple-hole orifices as an alternative. It is observed that the overall magnitude and extent of the disturbance levels in the flow are reduced with the multiple-hole orifices, while maintaining similar levels of pressure drop. It is hypothesized that these lower disturbances are a result of the small-scale flow structures associated with the multiple-hole orifice flow (multiple jets as opposed to one).

The measurements give detailed insights into the flow behavior downstream of orifice plates. Results indicate a low frequency flapping motion of the single-hole orifice jet, which is sustained by the surrounding large recirculation regions. For the geometries of the sharp-edged single-hole orifices investigated, the flapping frequency was observed to increase with flow speed and is found to occur at a Strouhal number ≈ 0.02 based on the orifice jet velocity and the difference in internal diameters of the pipe and orifice.

Acknowledgements

This thesis concludes a two year long Master's program at the faculty of Aerospace Engineering, TU Delft and summarizes the research work done between November 2013 and September 2014, as part of a collaborative project between ASML Netherlands and TU Delft. The experiments described in this document were performed at ASML and at the Aerodynamics laboratories of TU Delft. This work would not have been possible without the tremendous amount of guidance and help that I have received at ASML and at the Aerodynamics group during the above mentioned period.

I would first like to thank Prof. Fulvio Scarano for chairing my thesis committee and for his support during this project. His involvement and suggestions were decisive in the realization of the PIV experiments. In addition, his course on Flow Measurement Techniques bolstered my interest in the field of experimental fluid mechanics for which I shall always be grateful to him.

I have been fortunate to have had the supervision and guidance of Dr. Bas van Oudheusden and Dr. Nicholas Waterson during the course of this project. I am extremely grateful to Dr. Oudheusden for taking the time for discussions and for always being ready to help. I would like to acknowledge and thank Dr. Waterson for giving me the freedom to explore the subject and for patiently supporting me throughout this project. I sincerely thank both my thesis advisors for all their valuable remarks and suggestions.

I would like to thank Dr. Güneş Nakiboğlu for his guidance and the interesting discussions. The weekly meetings with Dr. Waterson and Dr. Nakiboğlu helped me make clear short term goals while keeping in mind the bigger picture.

The practical knowledge and experience of Jessica van Amerongen-Verdonschot played a crucial role in the approach taken in this study. I would like to thank her for all the interesting conversations and for helping me get familiarized with the clean-room environment. I am particularly grateful to Mustafa Perçin for his guidance and help all throughout this project. I have learnt a lot from him and his expertise played a pivotal role in the PIV measurements described in this study.

The test sections discussed in this document were designed at ASML by Maria del Carmen Mercado and Kristof van Becelaere. I thank them for their contribution towards the

present study and would like to mention that their innovative design allowed the experiments to be conducted smoothly without any complications. I would like to also thank Marcel van de Laar and the members of the ASML mechanical model shop for building both the test setups.

The experience of Peter, Nico, Fritz and the other technicians of the Aerodynamics lab enabled the experimental setup to be built and function according to plan. I sincerely appreciate all their help during the experiments. I would also like to thank the Aerodynamics group for allowing me access to the high-speed laser and camera systems.

I would like to express my gratitude to Rob Jansen for his support over the last 2 years. I will forever be grateful to him for selecting me for the ASML Henk Bodt Scholarship program that has funded my education at TU Delft. I would sincerely like to thank Dr. Martin Remie for his mentoring over the past two years. His close involvement with my progress and his frequent feedback on my work have always helped me improve. A special thanks to Annet ter Horst and Yide Zhu for making the scholarship program a great learning platform.

Big thanks to Anne for her constant motivation and to Marc van Duijnhoven for all the interesting discussions and for helping me figure out the PAK system. I am grateful to Sylvain Vugts and Frank van Boxtel for lending their complete support to my thesis project.

Thanks to my fellow class mates Jurriaan, Avinash, Guido, Zeno, Jaap and Aabhas for all the good times and for making group projects fun and interesting. I am extremely thankful to Jiggar for his hospitality during the experiments at Delft and to Chidambaresan for all the valuable suggestions.

Finally, I would like to thank all friends and family back home in India for their encouragement and support during the course of my stay here in the Netherlands.

Delft, The Netherlands Vinod Anantharaman
24th September, 2014

Contents

List of Figures

List of Tables

Nomenclature

Latin Symbols

d, d_h	Hole diameter	$[m]$
D, D_p	Pipe diameter	$[m]$
f_s	Sampling frequency	$[Hz]$
K	Pressure loss coefficient	$[-]$
N_h	Number of holes	$[-]$
P'_{rms}	RMS of the pressure fluctuations	$[Pa]$
P_c	Pitch	$[m]$
Re_h	Hole Reynolds number	$[-]$
Re_p	Pipe Reynolds number	$[-]$
St	Strouhal number	$[-]$
t	Plate thickness	$[m]$
U_h	Mean hole velocity	$[m/sec]$
U_p	Mean pipe velocity	$[m/sec]$
X_r	Mean reattachment length	$[m]$

Greek Symbols

β	Plate porosity	$[\%]$
ϵ	Surface roughness	$[m]$
μ	Dynamic viscosity	$[Pa.sec]$
ρ	Fluid density	$[kg/m^3]$

σ	Cavitation number	$[-]$

Subscripts

h	Property based on the orifice hole diameter
p	Property based on the pipe diameter

Abbreviations

PIV	Particle image velocimetry
POD	Proper Orthogonal Decomposition
PSD	Power spectral density
RMS	Root mean square

Chapter 1

Introduction

Orifices are key components in air and water cooling circuits in industries. These devices find widespread applications in pipe-lines of nuclear power plants (Haimin et al., 2013), aerospace propulsion systems (Ahuja et al., 2013), pressurized water reactors and reciprocating compressor systems (Howes & Greenfield, 2002).

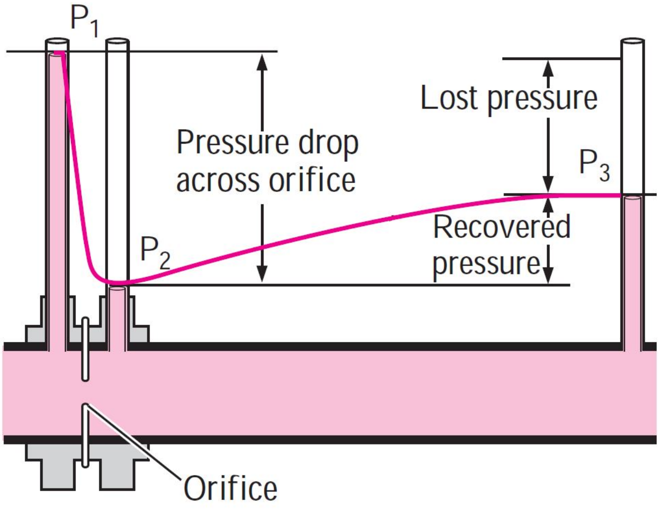

Figure 1.1: Figure illustrating the permanent pressure-loss occurring for a flow through a single-hole orifice taken from Cengel and Cimbala (2006).

Devices like the single-hole orifice plate or Venturi meter are conventionally used for measuring flow rates in fluid channels (Idelchik, 2008; Miller, 1990). The working principle of an orifice plate is that it creates a sudden change in cross-section area in the path of the fluid. Due to conservation of mass, the fluid needs to accelerate to adjust to the change in geometry. This increase in flow velocity is accompanied by a fall in static pressure due to conservation of energy. This process proceeds till the velocity reaches its maximum value (static pressure reaches its minimum value) and this point is referred to as the vena-contracta. It is also worth noting that the location of the vena-contracta is slightly downstream from the orifice.

Conventionally, this difference in static pressure as a result of fluid acceleration is used to determine the fluid flow rate when using orifice plates. After the vena-contracta, the fluid velocity starts to decrease (static pressure increases) and this is referred to as the recovery region. It is observed that the static pressure that is reached after recovery is lower than the upstream static pressure and this difference is the pressure-drop or permanent pressure-loss associated with the orifice plate. These processes (see figure 1.1) are described extensively in undergraduate books of fluid-mechanics and the reader is directed to Cengel and Cimbala (2006) for further information.

Orifice plates are usually calibrated in a laboratory environment (Frattolillo & Massarotti, 2002). However, the conditions in which they finally operate are quite different due to bends, turns and short development lengths present in fluid circuits (E. Laws, 1990). To ensure that the fluid entering the orifice is close to laboratory conditions it is common to make use of flow-conditioning devices like multi-hole orifice plates upstream of the flow-metering device to improve the accuracy of flow-rate measurements (Erdal, 1997; E. M. Laws & Ouazzane, 1994; Spearman et al., 1996). Similar to single-hole orifices, multi-hole orifice plates also create a permanent pressure loss when introduced in a fluid channel (Malavasi et al., 2012).

The permanent pressure loss that occurs in the flow due to turbulence and/or viscous effects, and which strongly depends on the geometry of the device (Maynes et al., 2013) is exploited in industries like nuclear power plants that require a permanent pressure-loss in their fluid channels to release excess fluid pressure (Haimin et al., 2013). Introduction of orifices increases the “resistance” offered to the fluid and leads to a decrease in flow-rate as illustrated in figure 1.2 (Miller, 1990). Coupled with the fact that orifices create pressure drops over short distances make them remarkably useful in parallel fluid-networks for flow balancing.

When the flow passes through the orifice, it accelerates due to mass conservation. Increase in flow velocity is a result of conversion of static pressure head to dynamic pressure. This conversion of energy involves little or no loss. On the contrary, the reverse process occurs in the recovery region, and involves significant amount of energy dissipation (Miller, 1990).

The flow exiting these devices however is a major source of disturbance for the flow in the circuit downstream, due to turbulence and/or cavitation (Weaver et al., 2000). In many instances it has lead to catastrophic failure of systems (Reethof, 1978). These are unwanted effects of these devices which need to be minimized.

Fluid flows in most pipelines belong to the turbulent regime. Turbulent flow comprises of different length and time scales of fluid parcels more-or-less in coherent motion which are commonly referred to as eddies. The spectral dynamics of these eddies are characterized by the so called energy-cascade process where energy transfer from the largest scales to the smallest Kolmogorov scales takes place, as schematically illustrated in figure 1.3 (Pope, 2000; Davidson, 2004). From Richardson’s theory (1922) it is accepted that majority of the energy that is “cascaded” is dissipated in the form of heat by the Kolmogorov scales. This is referred to as viscous dissipation. Its magnitude scales directly with the cube of the velocity and inversely with the length scale of the large eddies ($\epsilon \sim u_0^3/l_0$). This

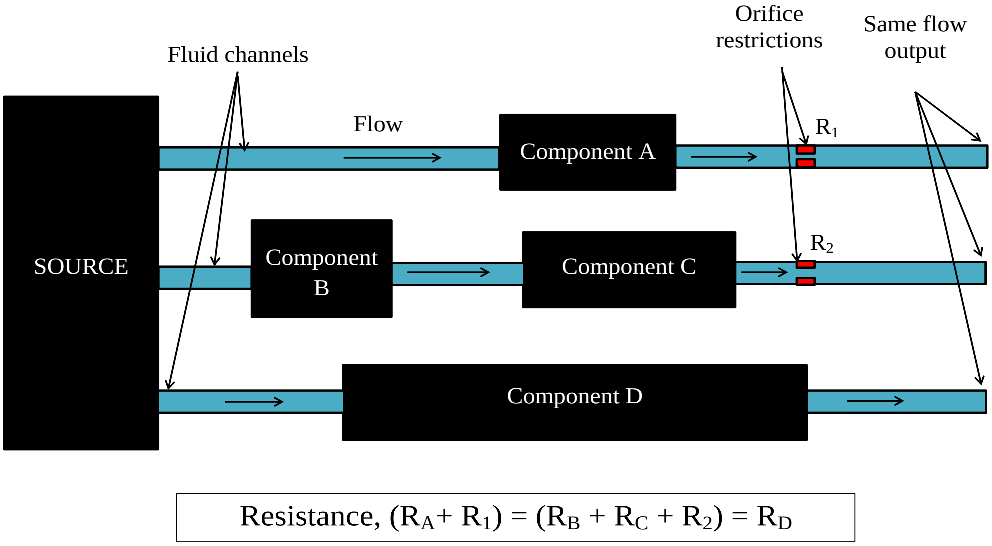

Figure 1.2: Illustration of the use of orifices as a pressure loss device for flow balancing.

dissipation of energy is an inherent property of turbulent flow. By introducing an orifice in the path of the fluid, this process is enhanced thereby achieving a permanent pressure loss over a much shorter distance.

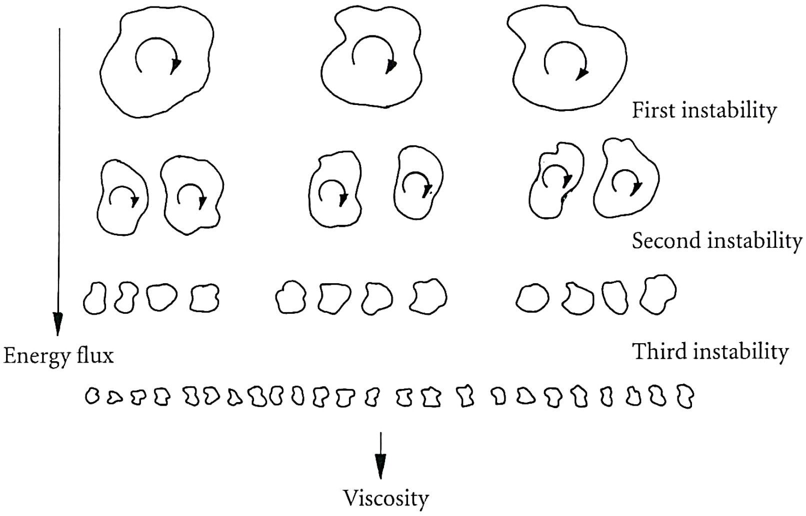

Figure 1.3: Schematic representation of the energy-cascade process taken from Davidson (2004).

An intrinsic property of turbulent flow is the strong unsteadiness associated with it. The presence of a restriction leads to an increase in downstream flow fluctuations. Figure 1.4 shows some features of the fluid flowing through a restriction valve. It is observed that a region of highly turbulent and unsteady flow exists in the vicinity of the device. In case of an orifice, a confined jet flows from the hole(s) of the plate. Additionally, the unsteady force exerted on the orifice gives rise to planar pressure waves that propagate through the system (see figure 1.4). These pressure-fluctuations originating from the turbulence and/or acoustic field can trigger structural resonance if their frequency is close to the structural natural frequency.

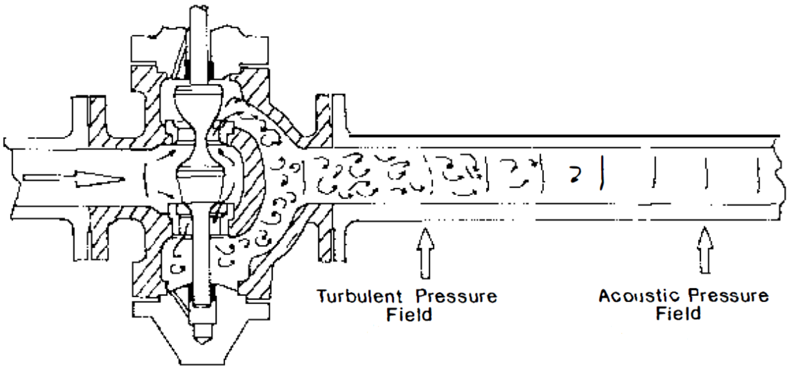

Figure 1.4: Schematic representation of noise generated by a valve taken from Reethof (1978).

1.1 Motivation

Flow issuing through orifices are widely regarded as a major source of vibration. The objective of the present investigation is to aid development of a system that creates a specific pressure-drop and also ensures that flow disturbances are within an acceptable level.

To reach this goal, it is essential to perform a rigorous analysis of the parameters involved and to understand the nature of the vibration source. In collaboration with **ASML**, the industrial partners of the project, the present study aims to generate knowledge that can ultimately be used to develop an optimum pressure-drop[1] system. This document describes results from experimental investigations that brings us a step closer to the above mentioned objective.

---

[1] The terms “pressure-drop” and “pressure-loss” are used in this document to describe the total pressure loss that results in the flow (see (P_1-P_3) in figure 1.1). Though there is fall in pressure just downstream from the orifice(see (P_1-P_2) in figure 1.1), the term pressure-drop here refers to the release (loss) of pressure by the action of orifices.

1.2 Outline of the thesis

This document is divided into nine chapters. Figure 1.5 presents a graphical overview of chapters that form a part of this thesis.

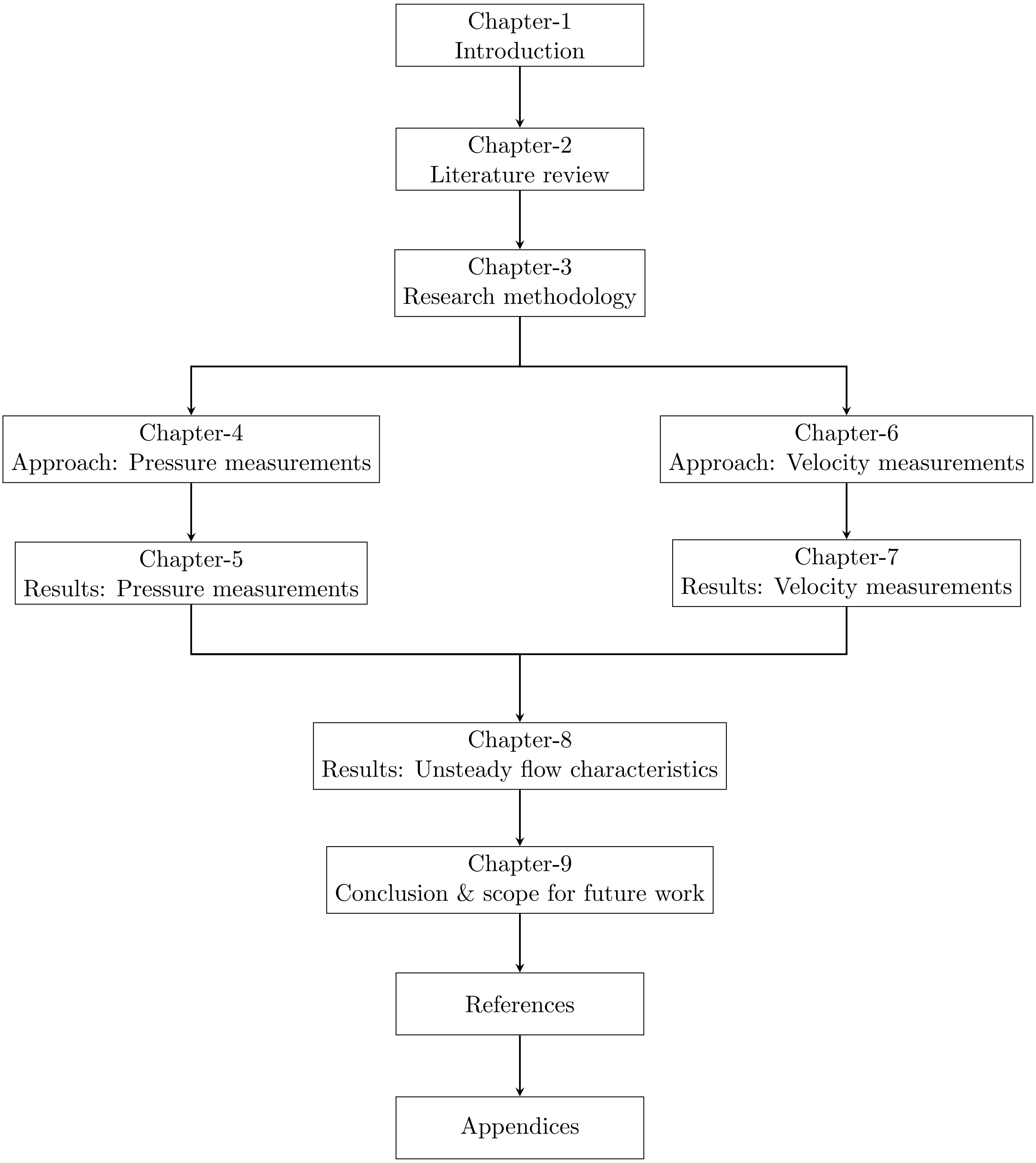

Figure 1.5: Outline of the thesis

Chapter 2 includes a summary of research articles considered relevant for the present investigations. Additionally, some definitions and terminology pertinent to the current study are presented in section 2.1. A summary of observations from literature can be found in section 2.6.

Chapter 3 describes the approach taken towards the current problem. The motivation for the experimental investigations along with the research scope of this study are highlighted in this chapter.

The approach involving pressure measurements that were implemented in this study are presented in chapter 4. A complete description of the experimental setup, instrumentation and experimental conditions are included in this chapter. Chapter 5 discusses the results obtained from these measurements.

Chapter 6 provides a description of the velocity measurements that were conducted. This includes the test setup, instrumentation and experimental conditions used during the PIV measurements. The results from these investigations are discussed in chapter 7.

Some unsteady characteristics of the flow, based on results from the two measurement approaches are described in chapter 8.

Chapter 9 provides the closing remarks for this document with a brief review of some results and scope for further studies in line with the present investigations.

Three appendices form a part of this document. The first, appendix A describes measurement uncertainty and errors. In appendix B and C, testing matrices of the pressure and velocity measurements are described respectively.

Chapter 2

Literature review

This chapter summarizes several research articles that were considered relevant for this study on pressure-loss devices. A major portion of this chapter reports observations from articles on pressure loss and pressure fluctuations created by the action of orifices. Flow over the backward-facing-step configuration has been extensively investigated and some useful observations are mentioned here, in view of their relevance to the orifice plate flow. The final section of this chapter highlights the operating principles of particle-image-velocimetry (PIV) along with some of its applications on cases that are pertinent to the current project.

The first section of this chapter describes some terms and definitions that are used throughout this document. These definitions are based on those frequently encountered in literature. However, the nomenclature used by the authors cited have been retained in their results shown in this chapter thus, the variables will differ from those described in section 2.1.

2.1 Terms and definitions

Consider a pipe of inner diameter D_p $[m]$ carrying an incompressible fluid of density ρ $[kg/m^3]$ and dynamic viscosity μ $[Pa.sec]$ at a mean velocity U_p $[m/sec]$. At some location within the pipe, an orifice[1] having an outer diameter equal to the pipe inner diameter is present. The geometrical variables that define sharp edged single and multi-hole orifices (or perforated plates) are shown in figures 2.1a and 2.1b respectively. Let the orifice of thickness t $[m]$, comprise of N_h number of holes of diameter d_h $[m]$.

A wide variety of terminology is found in literature and some useful terms are defined below to aid discussions in the subsequent sections of this document. The most common non-dimensional numbers that are used are:

---

[1] The term orifice or flow-restriction is used in this document to represent both single and multi-hole orifices. Multiple-hole orifices are also referred to as perforated plates in literature. While expressing distinctive characteristics, the type of orifice is mentioned explicitly.

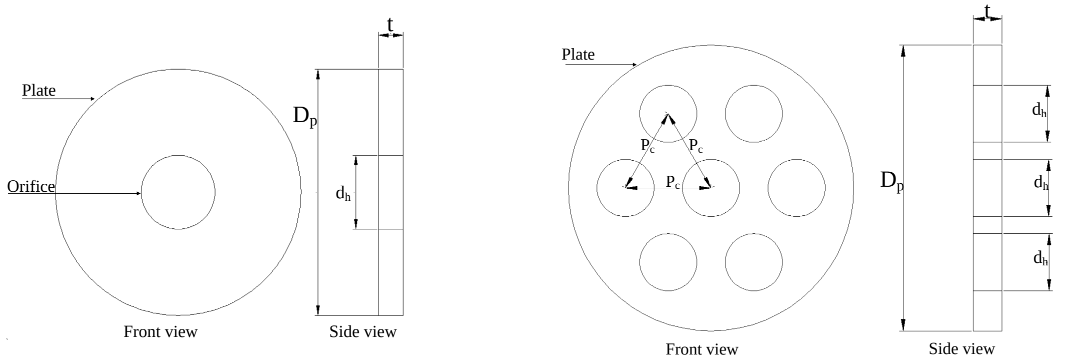

(a) Schematic of a sharp edged single-hole orifice plate

(b) Schematic of a sharp edged multi-hole orifice plate of 7 holes

Figure 2.1: Schematic of a single and multiple-hole orifice.

- **Pipe Reynolds number (Re_p):** Defined in terms of the pipe diameter D_p and mean centreline velocity in the pipe U_p as,

$$Re_p = \left(\frac{\rho U_p D_p}{\mu}\right) \tag{2.1}$$

- **Hole Reynolds number (Re_h):** Defined in terms of the hole diameter d_h and mean velocity through the hole u_h as,

$$Re_h = \left(\frac{\rho u_h d_h}{\mu}\right) \tag{2.2}$$

Let Q_p $[kg/sec]$ denote the mass flow rate of the fluid inside the pipe and Q_o $[kg/sec]$ the total mass flow through the orifice plate. If we assume that the flow is divided equally into each of the holes, then using conservation of mass,

$$\begin{aligned} Q_p &= Q_o \\ U_p D_p^2 &= N_h u_h d_h^2 \\ u_h &= \left(\frac{U_p D_p^2}{N_h d_h^2}\right) \end{aligned} \tag{2.3}$$

Using equation 2.3 into 2.2 results in the following simple relation between the hole and pipe Reynolds number:

$$Re_h = Re_p \times \left(\frac{D_p}{N_h d_h}\right) \tag{2.4}$$

- **Porosity (β) and equivalent diameter ratio (EDR):** Porosity is defined as the ratio of the total open area of the orifice (A_h) to the pipe cross section area (A_p). Some authors prefer to use the equivalent diameter ratio which is the square root of the porosity. For a single-hole orifice, EDR reduces to diameter ratio (DR).

$$\beta = \left(\frac{A_h}{A_p}\right) \tag{2.5}$$

$$\beta = \left(\frac{N_h d_h^2}{D_p^2}\right) = EDR^2 \tag{2.6}$$

- **Thickness ratio (t/d_h)**: The ratio of the plate thickness (t) to the hole diameter (d_h) is commonly referred to as the thickness ratio.
- **Pitch ratio (P_c/d_h)**: In case of multi-hole orifice plates, the pitch ratio represents the ratio of the distance between neighbouring holes to the hole diameter (d_h), (see figure 2.1b). It must be noted that not all multi-hole orifice plates employ holes placed equidistant to each other.
- **Pressure loss coefficient (K)**: It is the ratio of the total pressure-loss to the dynamic pressure of the mean flow and is also referred to as the **Euler number**. If the upstream and downstream flow area over which this difference is computed are equal, then the numerator reduces to the static pressure difference. Thus, it is calculated based on the static pressure difference upstream and *far downstream* from the orifice to indicate the pressure loss in non-dimensional form. This requires the downstream pressure-tap to be located such that the pressure recovery stage is complete (see figure 1.1). Mathematically it is given by,

$$K = \left(\frac{\Delta P}{\frac{1}{2}\rho U_p^2}\right) \tag{2.7}$$

- **Discharge coefficient (C_d)**: In conventional operation of single-hole orifice plates (as flow-rate measuring devices), the discharge coefficient represents the ratio of the actual to the theoretical flow rate. In this configuration, the downstream static pressure tap is located close to the orifice exit (typically $D/2$). The discharge coefficient accounts for entrance losses. It also corrects for the error that is made while using the orifice diameter (see equation 2.8) along with the pressure measured at the vena-contracta. As mentioned earlier, the width of the vena-contracta is expected to be smaller than the orifice-hole diameter.

$$\begin{aligned} C_d &= \frac{Q_{actual}}{Q_p} \\ Q_{actual} &= C_d \times A_h \times \sqrt{\frac{2\Delta P/\rho}{\left(1 - \left(\frac{d_h}{D_p}\right)^4\right)}} \end{aligned} \tag{2.8}$$

In situations where the downstream static pressure-tap is situated far enough from the orifice for the recovery to be complete, the discharge coefficient (C_d) and the loss coefficient (K) can be related as (Kolodzie & Winkle, 1957),

$$K = \left(\frac{1-\beta^2}{C_d^2\beta^2}\right) \tag{2.9}$$

- **Cavitation & Cavitation number (σ)** : The static pressure reaches a minimum in the vena-contracta. If it falls below the vapour pressure of the fluid (P_v), it can lead to a phase change. Using the static pressure far downstream (P_2), this phenomenon of formation of vapour bubbles is characterized in non-dimensional form by the cavitation number.

$$\sigma = \left(\frac{P_2 - P_v}{\frac{1}{2}\rho U_p^2} \right) \tag{2.10}$$

2.2 Studies on pressure losses created by orifices

The experiments of Kolodzie and Winkle (1957) were one of the earliest studies aimed at determining factors effecting pressure-loss over multi-hole orifice plates. They performed extensive measurements on multi-hole orifice plates with an equilateral triangle hole arrangement as shown in figure 2.2a. This ensures that each hole is equidistant from its neighbouring holes. Measurements were performed in a pipe of diameter 3"($76.2mm$) using air as the working medium. Static pressure taps were located $1D$ upstream and downstream from the orifice plate (see figure 2.2b) and were used to determine the pressure difference over the plates tested.

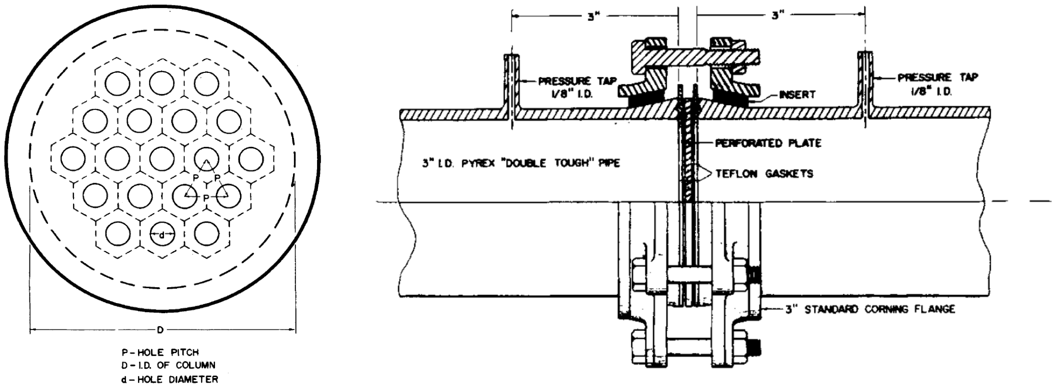

(a) Pattern of holes used in the plates tested

(b) Location of pressure taps

Figure 2.2: Orifice plate and pressure tap locations as described in Kolodzie and Winkle (1957)

Assuming that the pressure recovery is complete over this distance, the discharge coefficient results described by the authors can be related to the loss coefficient as given in equation 2.9. The authors specify that the orifice-discharge-coefficient (C_d) of a multi-hole orifice is a function of the following variables expressed in non-dimensional form as:

$$C_d = f\left[\left(\frac{\rho d_h u_h}{\mu} \right), \left(\frac{d}{P} \right), \left(\frac{t}{d_h} \right), \left(\frac{A_h}{A_p} \right) \right] \tag{2.11}$$

Additionally, the pressure-drop is also a function of the location of the pressure tap and shape of the orifice edge but these were kept constant. Combination of all the above variables were tested and it was observed that the orifice discharge-coefficient remains more or less constant for $Re_h > 4000$ for a given plate geometry. Note that the discharge coefficient is inversely related to the pressure loss coefficient (see equation 2.9). The effect of different parameters can be clearly seen in figures 2.3a and 2.3b. Increase in thickness-to-hole-diameter ratio reduces the pressure losses (higher discharge-coefficient). The authors specify that pressure losses are minimum when $t/d_h \geq 1$, $P/d_h \leq 2$ and porosity $> 60\%$. These were shown to exist for $4000 \leq Re_h \leq 20000$.

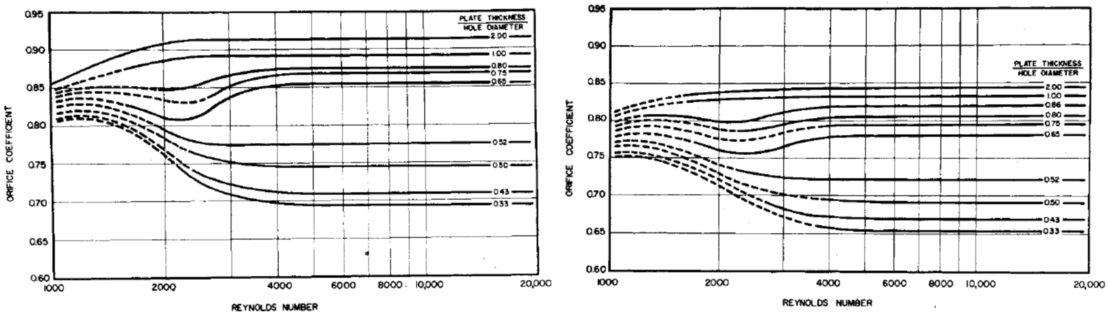

(a) Pitch to hole diameter $P/d_h = 2$, porosity= 14%

(b) Pitch to hole diameter $P/d_h = 4$, porosity= 5%

Figure 2.3: Orifice coefficient as a function of Re_h for different t/d_h (Kolodzie & Winkle, 1957)

Malavasi and Messa (2011) performed CFD computations (RANS using $k - \epsilon$ turbulence model) on sharp-edged, single-hole orifices covering a wide range of Reynolds number. It is suggested that the qualitative behaviour of the pressure loss-coefficient as a function of Reynolds number (Re_h or Re_p) is as shown in figure 2.4. Three distinct regions can be identified, however their boundaries are not well defined.

- Region 1: The author suggests that the behaviour of the curve in region 1 is unclear as the losses may present a local minimum and then increase or decrease monotonically.
- Region 2: This region is commonly referred to as the self-similar region since the loss-coefficient is independent of the Reynolds number here. This implies that flow conditions lying in this region can be used to isolate the effect of geometrical parameters on the pressure loss coefficient.
- Region 3: This domain is characterized by a sharp rise in pressure losses. It occurs due to cavitation as the fluid static pressure in the vena-contracta falls below the vapour pressure of the liquid and leads to a phase change.

The authors propose a numerical model to predict cavitating conditions based on CFD data obtained from a large number of geometries. The flow conditions belong to the self-similar region, $Re_p = 3.85 \times 10^4$ to 1.54×10^5 and the results seem to show good agreement with previous experiments.

Multi-hole orifice plates, as mentioned earlier, are commonly used to remove flow irregularities in pipelines. Malavasi et al. (2012) conducted two experimental campaigns to

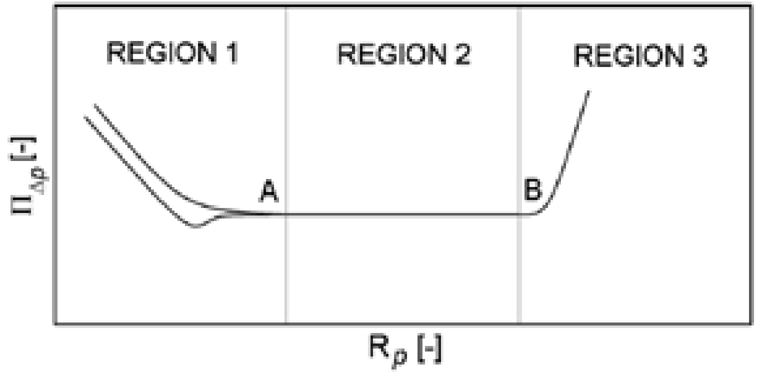

Figure 2.4: Qualitative behaviour of the pressure loss coefficient ($\Pi_{\Delta p}$) as a function of Reynolds number (Malavasi & Messa, 2011).

investigate the dissipation characteristics of multi-hole orifices under cavitation-free conditions. In one setup, pressure drop was measured using absolute and differential pressure transducers $2D$ upstream and $6D$ downstream from the device. In the other setup, pressure taps were located $1D$ upstream and $10D$ downstream from the plate and mercury differential pressure manometer along with bourdon pressure gauges were used. A total of 21 different plate configurations were tested in these experiments that studied the effect of Reynolds number and geometrical parameters on the pressure loss. It is interesting to note that the three regions defined earlier for single-hole orifices were also identified for multi-hole orifices (see figure 2.5). Note, region-1 and region-2 are also evident in the results of Kolodzie and Winkle (1957) in figure 2.3.

For cases tested in the self-similarity range, it was found that the pressure loss coefficient decreases with increasing thickness-to-hole-diameter ratio (keeping all other variables constant). This decrease is however not monotonic as for some range of t/d_h flow instabilities can occur which lead to a non-monotonic decrease in pressure drop. It is observed that the plate porosity (β) is the most dominant parameter effecting pressure losses for conditions belonging to the self-similarity regime. Furthermore, it is stated that it is difficult to assess the effect of hole distribution which controls curvature of the flow streamlines. Another important observation is that while keeping the same porosity and thickness ratio, pressure loss coefficient decreases with increasing number of holes. Malavasi et al. (2012) believe that this is due to a reduction in the size of recirculation zones in the wake.

Recent experimental observations by Maynes et al. (2013) provide valuable insight to the pressure losses that occur while using perforated plates. Static pressure transducers $3D$ upstream and $6D$ downstream from the device were used in their experiments. Additionally, an accelerometer was placed $3D$ downstream to record pipe vibrations. The vibrations in the pipe wall respond directly to the pressure fluctuation changes that occur due to cavitation. Figure 2.6 shows the four regimes that are marked by sharp changes in pipe wall acceleration. The first region ($\sigma > 5$) is the turbulent regime where the vibrations are entirely due to turbulent jets and their interactions. In the second region ($4 < \sigma < 5$) acceleration levels increase dramatically. This regime represents onset of

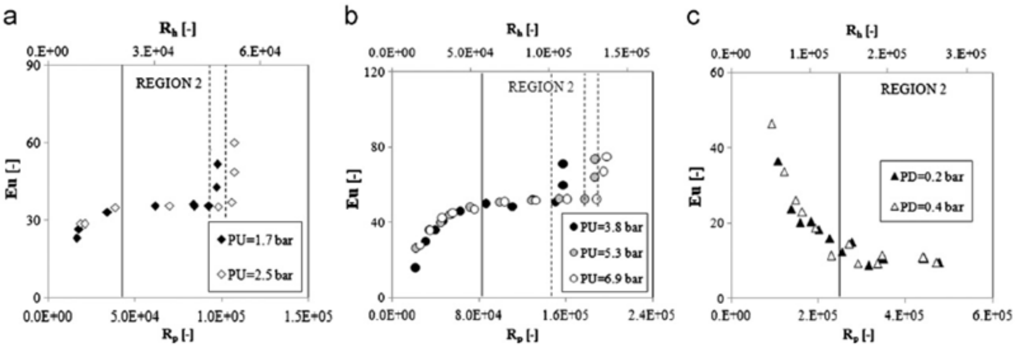

Figure 2.5: Behaviour of the pressure loss coefficient (Eu) as a function of Reynolds number a) $\beta = 16\%$, $N_h = 26$, $t/d_h = 1$ b) $\beta = 16\%$, $N_h = 13$, $t/d_h = 1$ c) $\beta = 16\%$, $N_h = 13$, $t/d_h = 0.72$. (Malavasi et al., 2012)

cavitation, although it is intermittent. The third ($2 < \sigma < 4$) is the regime where the flow is completely cavitating. The fourth ($\sigma < 2$) is said to be the choked regime. Although very interesting, only a few studies on cavitation and its effects will be discussed in this document.

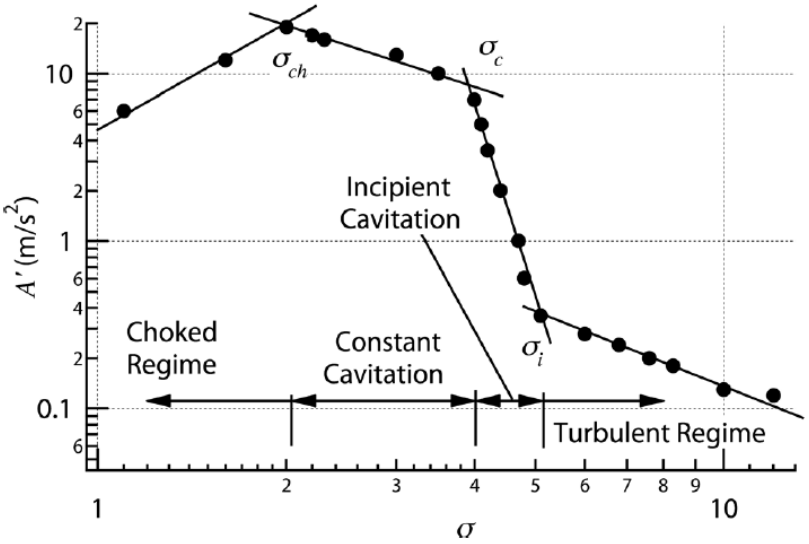

Figure 2.6: A representative plot of wall acceleration A' as a function of cavitation number σ illustrating the four cavitation regimes (Maynes et al., 2013).

Maynes et al. (2013) investigated the effect of plate thickness for flow through multi-hole orifice plates. Here, 16 different orifice plates were used. They compare their results to 2 existing models (Blevins, 1984) depending on whether the flow inside the plate reattaches or not (see figure 2.7). Equation 2.12 shows the loss coefficient for a detached model obtained using an integral momentum analysis. Similarly, equation 2.13 presents the result for an attached flow model. These models of the loss coefficient are a function of the model geometry and α which is the ratio of the area of the vena-contracta to the hole area. It is observed that these existing models form an upper and lower bound to the loss coefficient data measured by several different studies. This is shown in figure 2.8a where the ordinate K_{Lh} is the pressure loss coefficient based on hole velocity and is related to the loss coefficient by equation 2.14.

$$K_{LD} = \left(\frac{1}{\alpha} - \frac{A_h}{A_p}\right)^2 \tag{2.12}$$

$$K_{LA} = 2 \times \left(1 - \frac{A_h}{A_p} - \frac{1}{\alpha}\right)^2 + \frac{1}{\alpha^2} + \left(\frac{A_h}{A_p}\right)^2 \tag{2.13}$$

$$K_{Lh} = K_L \times \left(\frac{A_h}{A_p}\right)^2 \tag{2.14}$$

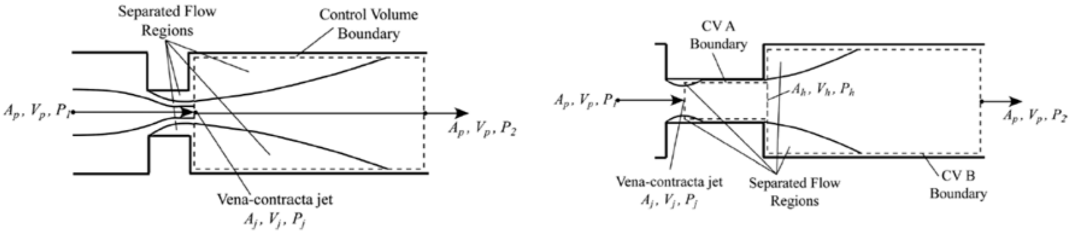

Figure 2.7: Illustration of flow through (left) thin orifice detached model and (right) thick orifice attached model (Maynes et al., 2013).

Figure 2.8b presents the Reynolds number independence of the pressure loss coefficient (behaviour in region 2) for different plate porosities. The authors also observe this behaviour for $Re_h \geq 3000$ as previously reported by Kolodzie and Winkle (1957). At higher hole velocities a sharp increase in the loss coefficient is observed due to onset of cavitation. Figure 2.8c shows the behaviour of the pressure loss coefficient as a function of the thickness ratio (t/d_h). It can be clearly seen that the loss coefficient decreases for increasing thickness ratio. This is attributed to flow reattachment within the orifice. At higher thickness ratios a slight increase in the pressure loss coefficient is observed due to frictional losses. Based on their observations, the authors propose a model that shows good agreement with experimental data (see figure 2.8d). This model is expressed in equation 2.16 where ϕ is determined through statistical analysis and is given by,

$$\phi = (t/d)(A_h/A_p)^{1/5} \tag{2.15}$$

$$\frac{K_{Lh}}{K_{LA}} = F(\phi) = \begin{cases} 2.9 - 3.65\phi + 1.75\phi^2, & \phi \leq 0.95 \\ 0.932 + 0.078\phi, & \phi > 0.95 \end{cases} \tag{2.16}$$

Zhao et al. (2011) performed experiments on both single and multi-hole orifices in order to isolate the most prominent geometrical parameter effecting pressure losses. The setup

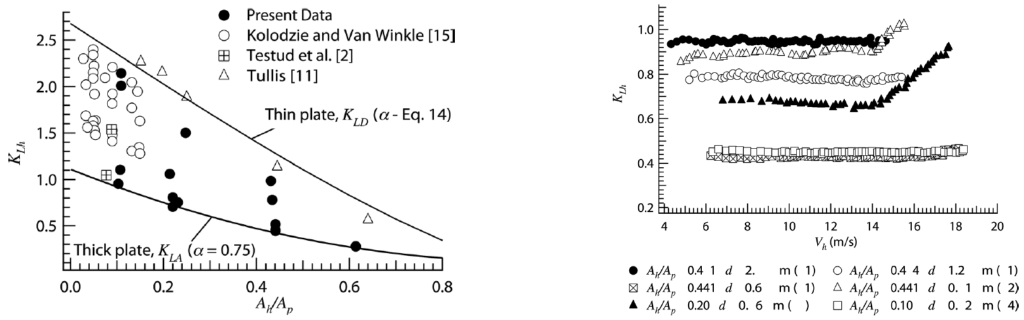

(a) K_{Lh} as a function of porosity

(b) K_{Lh} as a function of hole velocity

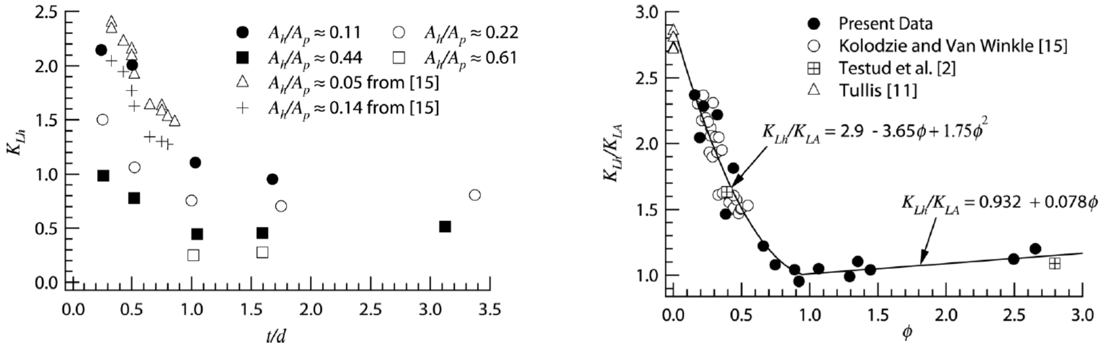

(c) K_{Lh} as a function of thickness ratio

(d) K_{Lh} as a function of ϕ

Figure 2.8: Behaviour of loss coefficient based on hole velocity K_{Lh} reported in Maynes et al. (2013)

comprised of static pressure transducers at upstream locations of $-12D$, $-9D$ and $-6D$ and at downstream locations of $20D$, $24D$ and $28D$. The average static pressure values upstream and downstream are used to determine the loss coefficient. All the plates tested had the same thickness and the multiple-hole orifices had holes of equal sizes. Plates shown in figure 2.9a have the same porosity (16%). Figure 2.9b presents the pressure loss coefficient as a function of pipe Reynolds number for these plates. It is observed that for the range tested, the pressure loss coefficient of the single-hole orifice was the highest. Furthermore, this value seems to be independent of the Reynolds number (self-similar region). It is clear that for the same porosity, the difference in the pressure loss coefficient between single and multi-hole orifices is quite high for lower Reynolds number ($Re_D < 15000$). This difference reduces for higher Re_D. The pressure loss coefficient is higher when there are fewer number of holes (for the same porosity). The results also show that the self-similar region for single and multi-hole orifices of the same porosity can be quite different. Note, the thickness to hole diameter ratio was not kept constant between the plates tested.

Some pipelines make use of multiple orifices in series in order to get extremely high pressure drops. Haimin et al. (2013) performed measurements on a six-stage orifice system by varying the geometric parameters of the first and the last orifice. All plates used have the same thickness however the center of the holes have an offset with respect to the

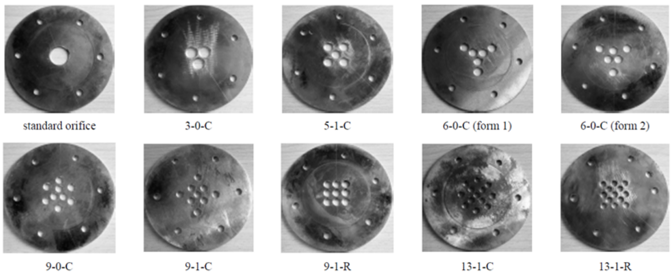

(a) All plates of porosity 16% tested.

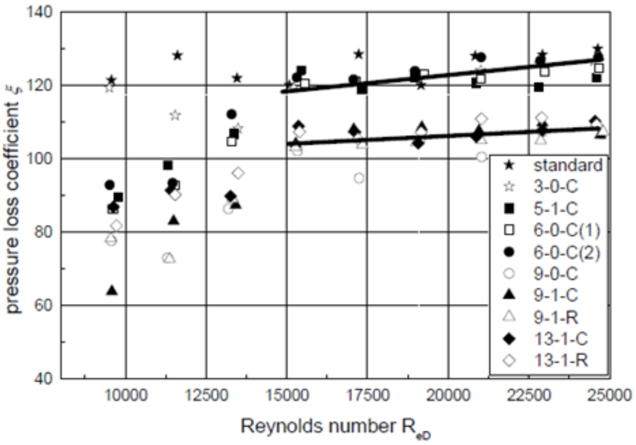

(b) Plot of pressure loss coefficient ξ as a function of pipe Reynolds number Re_D

Figure 2.9: Plates tested and their associated pressure loss coefficients reported by Zhao et al. (2011)

axis of the pipe (see figure 2.10). Furthermore, the distance between the orifices are fixed. The authors do not provide a theoretical motivation for such an arrangement. It is observed that the majority of the pressure loss occurs over the first orifice and smaller orifice diameters lead to higher pressure losses.

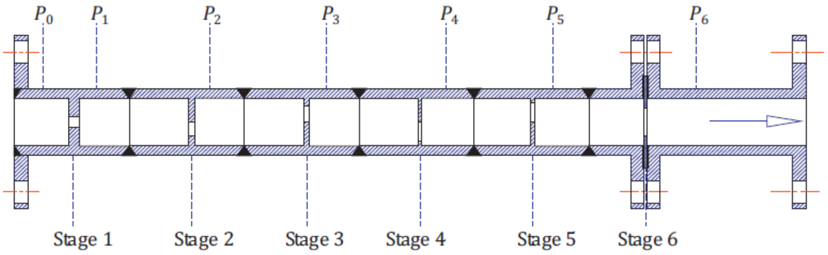

Figure 2.10: Illustration of a six stage orifice tube used by Haimin et al. (2013).

2.3 Studies on pressure fluctuations created by orifices

Moussou (2006) showed that the amplitude of the hydrodynamic pressure fluctuations close to the orifice is higher than the far-field disturbances. This is represented in the form of Power Spectral Density(PSD) curves and is shown in figure 2.11. Three distinct peaks are observed in the curve quantifying fluctuations in the vicinity of the orifice. The first peak at a frequency $\approx 200Hz$ could represent some unsteady phenomenon in the wake of the orifice. However, the author doesn't provide any information regarding this. It is interesting to note, that even though the downstream disturbance levels are lower in magnitude, the peak at this particular frequency still persists and is of significantly higher magnitude.

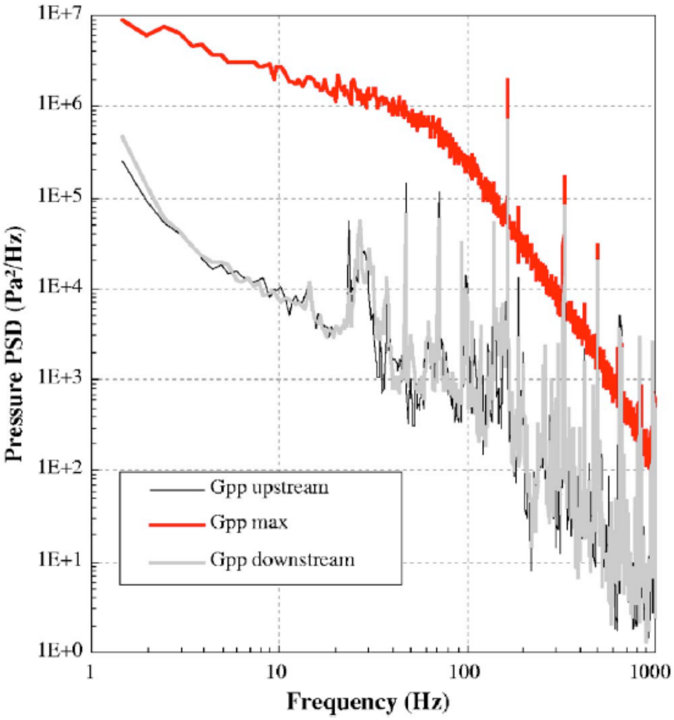

Figure 2.11: Power spectral density curves for an orifice with diameter ratio 0.4 at a flow-rate of 410 m^3/h as reported by Moussou (2006)

Qing et al. (2006) performed measurements of the fluctuating pressure upstream and downstream of single-hole orifice plates. They positioned dynamic-pressure transducers both axially and circumferentially along the pipe. The test facility made use of water-block tanks to absorb pressure waves arising from the pump (see figure 2.12). Three different orifice plates of diameter ratios 0.255, 0.304 and 0.335 were tested at flow-rates of 15, 25 and 40 m^3/h. The readings from the circumferentially mounted sensors indicate that variation in measurements along the radial direction are minimal. The time-series data of the fluctuating-pressure is used to compute the Power Spectral Density (PSD). This is then expressed in a normalized form and plotted as a function of the Strouhal number (non-dimensional frequency) as shown in figure 2.13. The PSD is normalized by the square of the mean dynamic head and using the ratio of the orifice hole diameter and hole velocity. The Strouhal number is defined based on the orifice hole diameter and hole velocity. Figure 2.13 depicts the pressure fluctuations at different measurement points. It is evident that the magnitude of the pressure fluctuations are the highest at location 5. This point is located $1.7D$ downstream from the orifice. The authors mention that the majority of the energy content lies in the frequency range of $0-400Hz$ which corresponds to a Strouhal number of $0-6.2$.

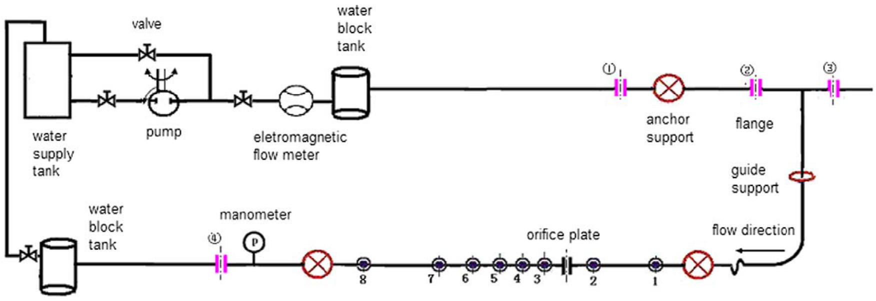

Figure 2.12: Experimental setup of Qing et al. (2006) showing axially arranged pressure sensors.

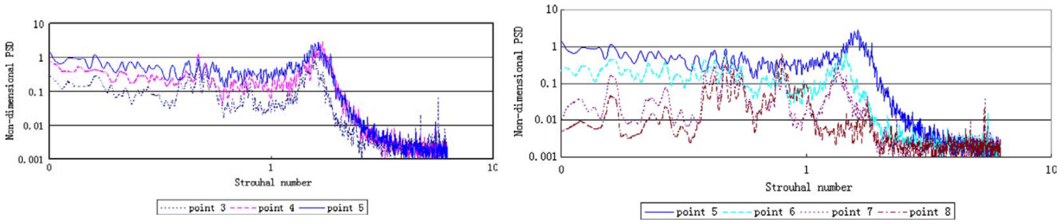

(a) PSD computed at measurement points 3, 4 and 5 (see figure 2.12)

(b) PSD computed at measurement points 5, 6, 7 and 8 (see figure 2.12)

Figure 2.13: Power spectral density (PSD) curves for an orifice with diameter ratio 0.335 at a flow-rate of $25\ m^3/h$ reported by Qing et al. (2006).

One can compute the root mean square (RMS) of the pressure fluctuations by taking the square root of the integral of the PSD in the frequency domain. Figure 2.14a shows that the RMS of the fluctuations are the highest at $1.7D$ downstream from the orifice. The orifice with the smallest hole diameter produced the highest fluctuations. These disturbances reduce significantly far downstream from the orifice. Figure 2.14b shows the expected trend of increase in RMS for increasing flow rates.

There have been a few investigations on pressure fluctuations created by cavitating orifices. Testud et al. (2007) study the acoustical effects of cavitation caused by single and multi-hole orifices. Flow conditions belong to a Reynolds number range 2×10^5 to 5×10^5. Cavitation was observed in all the cases tested. It is assumed that only acoustic plane waves propagate through the system. The objective is to determine p^+ and p^-, the upstream and downstream traveling waves respectively. Using a reference sensor, the authors compute the cross-spectral density $G_{pp_{ref}}(f)$ which is defined as the Fourier transform of the cross-correlation of the two time signals. Whistling is observed in every developed cavitation regime of sharp-edged single-hole orifice experiments (it is never observed for thick multi-hole orifice experiments). Evidence of whistling is found in the upstream

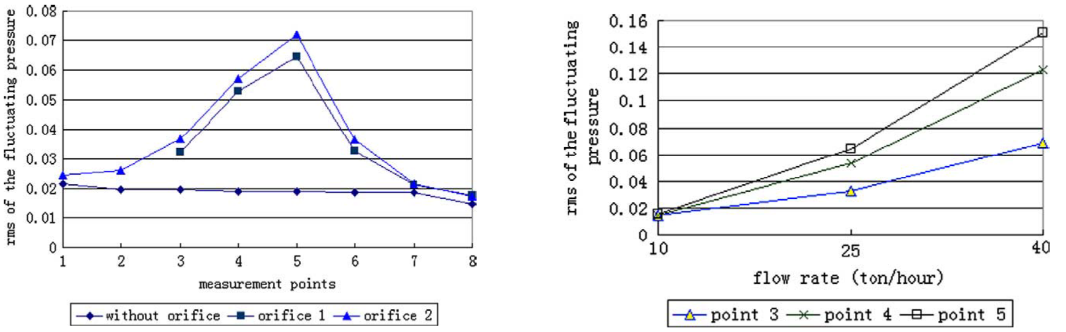

(a) RMS of the fluctuating pressures at different measurement points.

(b) RMS of the fluctuating pressures at different flow rates.

Figure 2.14: RMS of the fluctuating pressures as given by Qing et al. (2006)

acoustical spectra, by the sharpness of the fundamental frequency peak f_0 and the existence of several harmonics at exact multiples of f_0 as shown in figure 2.15. This peak corresponds to a Strouhal number close to 0.2 based on the orifice thickness and orifice velocity.

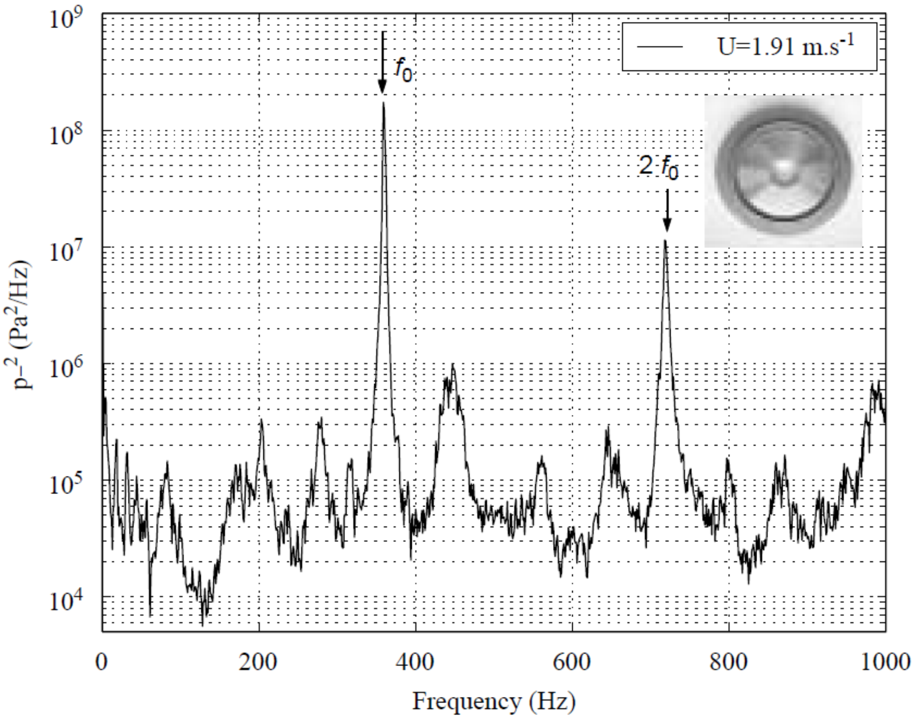

Figure 2.15: Detection of whistling frequency f_0 with harmonics on upstream plane wave spectra p^- (Testud et al., 2007).

2.4 Studies on Backward-Facing-Step

The backward facing step (BFS) is a simple geometrical configuration that produces highly unsteady and separated flow in its wake. This configuration has been studied extensively using both numerical and experimental techniques (Le et al., 1997; Scarano et al., 1999; Schröder et al., 2013). Figure 2.16 illustrates the expected flow features. The point of separation is fixed to the step edge. Immediately after detachment, the flow behaves as a free shear layer, with high-speed fluid on one side and low-speed fluid on the other. At a certain distance downstream, the shear layer impinges on the surface and forms a closed recirculation region containing turbulent, upstream moving fluid. Reattachment occurs over a region referred to as the mean reattachment point, X_r. The flow in this zone is found to be unsteady and highly three-dimensional with large-scale structures (see figure 2.17), of size in the order of the step size passing through frequently (Kostas et al., 2002). Downstream of reattachment, the boundary layer begins to redevelop.

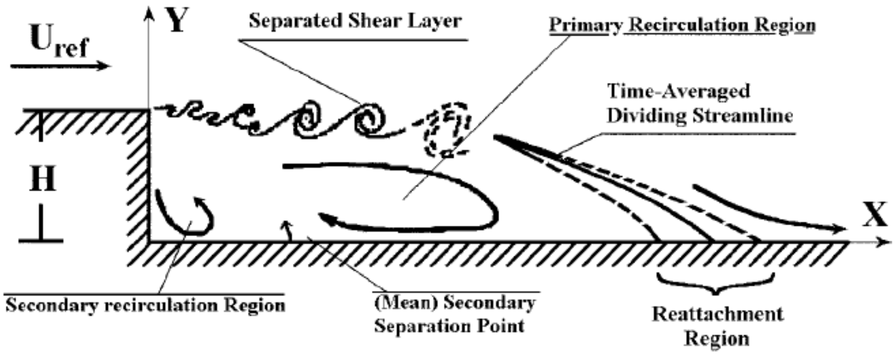

Figure 2.16: Sketch of the expected topology of a backward-facing step flow (Spazzini et al., 2001)

Spazzini et al. (2001) use a skin-friction probe to perform time-resolved measurements in the region close to reattachment. The Reynolds number based on step height were 3500, 5100, 10000 and 16000. The mean reattachment location was defined as the point where the mean skin friction becomes 0 or the point where the forward flow probability (FFP) is 50%. Both these methods were used to estimate the mean-reattachment location X_r (see table 2.1). The data indicate that results from both methods are comparable.

Reynolds number	Distance X/H Method $C_f = 0$	Distance X/H Method 50% FFP
3500	5.05	5.02
5100	5.39	5.39
10,000	6.14	6.14
16,000	6.54	6.54

Table 2.1: Mean position of primary reattachment determined using two methods (Spazzini et al., 2001)

Kostas et al. (2002) perform planar Particle Image Velocimetry (PIV) measurements on a backward facing step flow at a $Re = 4660$. It is observed that the highest values of Reynolds shear stress are found just before reattachment at a height of $0.7h$. The location of the peak turbulent kinetic-energy production occurs further upstream than the location of the peak in any of the Reynolds stress distributions. This is attributed to the dependence of the turbulent kinetic-energy production on both the Reynolds-stress components and the mean spatial-velocity gradients.

Lee and Sung (2001) use 32 microphones in span-wise and stream-wise direction to measure pressure fluctuations occurring downstream of the backward-facing step configuration at $Re = 33000$. It was observed that the root-mean-square (r.m.s) of the pressure fluctuations attains a maximum in the upstream vicinity of the mean-reattachment point.

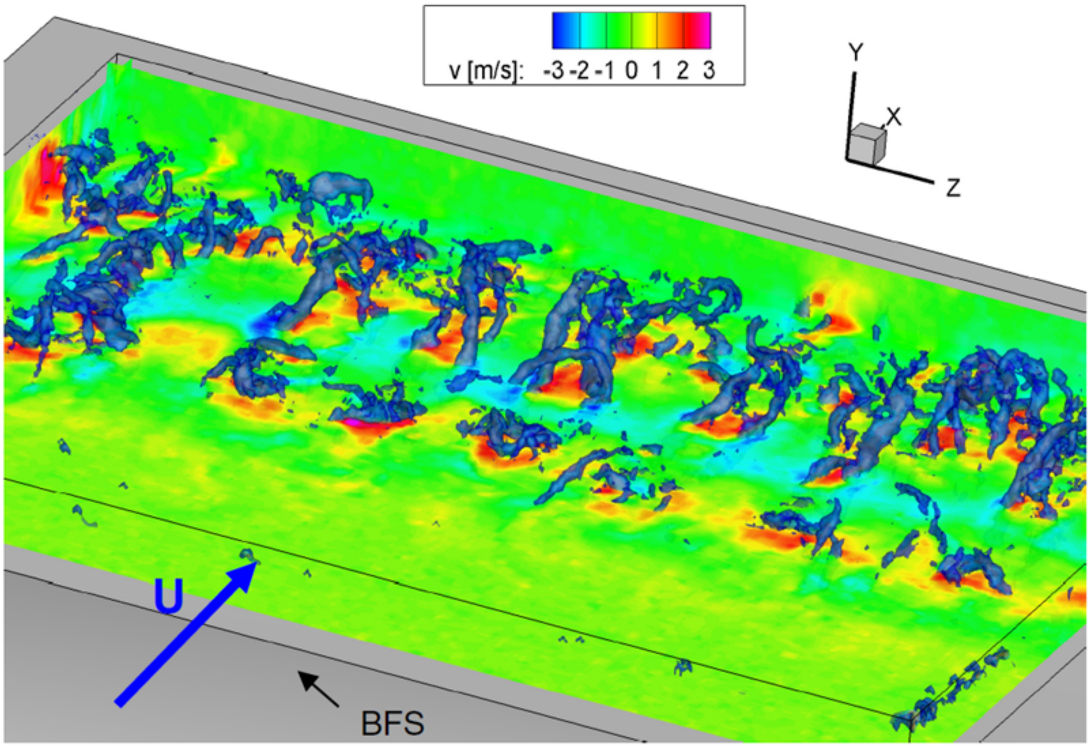

Figure 2.17: An instantaneous 3D-velocity volume depicting flow structures of the shear layer transition behind a BFS by iso-surfaces of 3D- vorticity and selected velocity planes (horizontal plane at y = -h/2, v colour coded, U = 6.4 m/s) reported in Schröder et al. (2013)

2.5 Particle Image Velocimetry (PIV)

Particle Image Velocimetry (PIV) is a powerful whole-field, non-intrusive flow measurement technique that has achieved great success in the field of fluid-dynamics in the last two decades (Adrian & Westerweel, 2011). It has been applied successfully to almost all scales of fluid motion and has helped quantify several complex flow fields (Westerweel et al., 2013). The most attractive feature of PIV is that it is a whole-field technique which allows one to get instantaneous velocity data with high resolution. With recent developments in hardware systems along with improved post-processing algorithms, it is also possible to perform time-resolved-3D measurements (Scarano, 2013b).

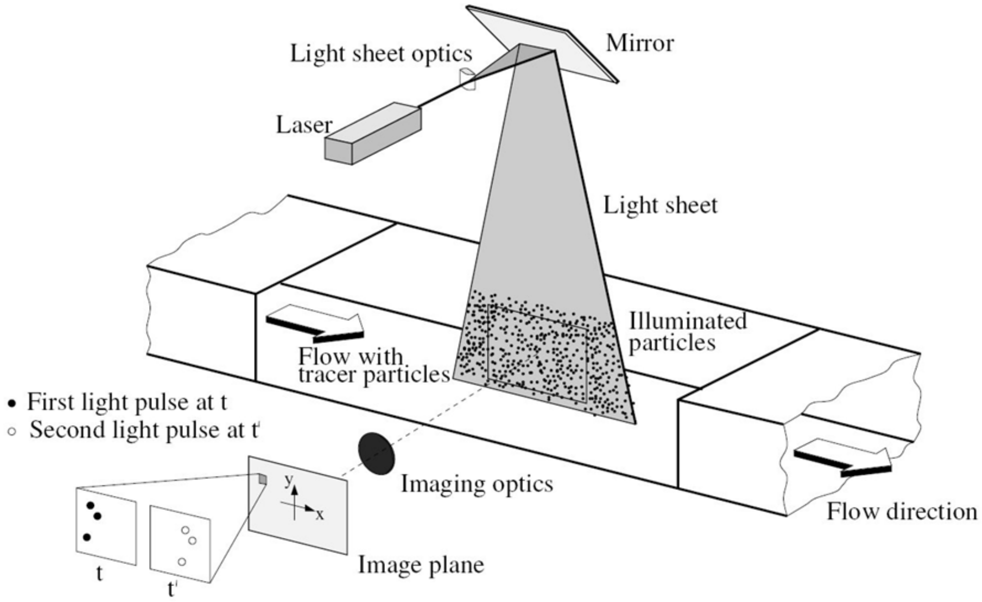

Figure 2.18: Schematic representation of a conventional, planar-PIV setup (Raffel et al., 2007).

The following sub-sections highlight the basic operating principle of PIV and important experimental considerations that need to be taken before an experiment. The final sub-section is devoted to research articles that showcases its application on internal flows.

2.5.1 Working principle

This technique involves the introduction of tracer particles in the flow, which are subsequently detected in the region of interest using optical systems. The basic principle is to measure the displacement of small tracer particles that are carried by the fluid during a short time interval.

The seeding particles are illuminated within a thin light-sheet generated from a pulsed light-source (usually a double-head pulsed laser system). The particles scatter light that allow their position to be detected and recorded onto two subsequent image frames by a digital imaging device. These are usually CCD or CMOS cameras that are placed perpendicular to the measurement plane in case of two-dimensional planar-PIV. Figure 2.18 illustrates the operation of a typical setup for PIV experiments.

2.5.2 Experimental considerations

The successful implementation of a PIV experiment requires consideration of many parameters. The following sub-section highlights some guidelines and fundamentals that need to be understood before performing PIV experiments. These are largely extracted from Raffel et al. (2007); Scarano (2013a) and the reader can find detailed information about the principles of PIV and the hardware involved in Raffel et al. (2007); Westerweel et al. (2013).

- **Seeding particles & seeding generation**
  This measurement technique measures the velocity of the seeding particle and not the fluid directly. Thus, it is imperative that the particles accurately trace the path taken by the fluid and not alter its properties or underlying characteristics.

  When a tracer particle is introduced in the flow, there are several forces that act on it. Assuming small spherical particles, the most dominant force acting on it is the viscous drag or Stokes drag (Melling, 1997). Assuming that particles of size d_p and density ρ_p are travelling with a velocity U_p in a fluid medium of density ρ_f and kinematic viscosity ν moving at a velocity U_f, the particle dynamics equation can be expressed in simplified form as,

  $$U_p - U_f = d_p^2 \left(\frac{\rho_p - \rho_f}{18\mu} \right) \frac{dU_p}{dt} \tag{2.17}$$

  The above expression shows that good tracing requires the right hand side of equation 2.17 to be as small as possible. This condition can be satisfied for liquid flows, however the difference in particle and fluid density becomes quite large for measurements in air. As a result, measurements in air employ particles of size $0.5\mu m \leq d_p \leq 5\mu m$.

  Table 2.2 describes the properties of some common tracer particles used in PIV measurements.

Fluid	Material	Mean diameter (μm)	Particle density (kg/m^3)
Air	DEHS	$0.5 - 1.5$	10^3
Air	TiO_2	$0.1 - 5$	$1 - 4 \times 10^3$
Air	Vegetable Oil	$1 - 3$	10^3
Water	Sphericell®	$10 - 100$	$0.95 - 1.05 \times 10^3$
Water	Silver coated hollow glass spheres	$10 - 100$	$> 10^3$

Table 2.2: Properties of some commonly used tracer particles in PIV experiments (Raffel et al., 2007)

Small particles are required to fulfil the fluid mechanical requirements of good flow-tracing. However, as an opposing requirement the particles should also be large enough to scatter sufficient light in order to be visible. Particles with high refractive index show excellent scattering properties. The most common approach is to select the largest particles that can accurately follow the flow.

Introduction of seeding particles and achieving uniform seeding concentration is one of the major challenges for PIV measurements. For experiments in water it is just required to mix the particles in solid or suspension form with water. For experiments in air, seeding generators like the Laskin nozzle, cyclone generators and fluidized-bed generators are commonly used (Raffel et al., 2007).

- **Light source**
  A PIV measurement relies on a finite observation time Δt to detect particle motion. The particle tracers need to be illuminated and observed twice within this time separation. Furthermore, it is important that the particles appear as dots and not as streaks. This requires the light pulse duration (δt) to be small.

  Lasers are used as illumination sources as they can produce a pulsed, collimated and monochromatic beam of light. The beam direction can be controlled using mirrors and it can be easily shaped into thin sheets using lenses.

  The most common light source used for PIV experiments is the solid-state frequency-doubled neodymium-doped yttrium aluminium garnet laser (Nd:YAG) that emits light at a wavelength of 532 nm. The repetition rate of Nd:YAG systems ranges between 10 and 50 Hz. Recent advancements in the area of solid-state lasers has led to the development of lasers with high repetition rate. Neodymium-doped yttrium lithium fluoride (Nd:YLF) laser systems are used for performing time-resolved measurements as these lasers offer a repetition rate between 1 to 5 kHz.

  It is important to note that these are Class IV lasers. The direct beam and reflections can be extremely hazardous to the eyes and skin. It is crucial that proper safety procedures are adhered to while operating these devices.

- **Imaging**
  Images of tracer particles that are illuminated by the laser are recorded onto the image sensors of recording devices like CCD and CMOS cameras. The imaging system is characterized by its focal length f, $f_{\#} = f/D$ (where D is the lens aperture diameter) and image magnification M which is the ratio of the size of the image to that of the object.

  When the particles of diameter (d_p) are in focus, their final image diameter comprises of two components. Firstly, due to the geometric optics such that $d_{geo} = M \times d_p$ and additionally, due to diffraction such that $d_{diff} = 2.44\lambda(1+M)f_{\#}$. The effective particle image diameter d_i can be estimated by the Euclidean sum of the individual components as:

  $$d_i = \sqrt{(M \times d_p^2) + d_{diff}^2} \qquad (2.18)$$

  The typical size of a pixel in camera sensor is in the order of 10 μm. If the image size of the particles are smaller than the sensor resolution, then the particle position cannot be detected with sub-pixel accuracy. This causes position errors up to 0.5

pixels and this condition is commonly referred to as peak locking or pixel locking. This means that particle position and the measurement displacement tend to be locked to integer values. To minimize errors arising due to peak-locking, it is advised to achieve an optimum particle image size of approximately 2 pixels.

- **Vector calculation and optimization rules**
  The recorded images are partitioned into small cells called interrogation windows of size ranging from 16 × 16 pixels to 128 × 128 pixels. Every interrogation window is an individual measurement volume where the local velocity vector is evaluated. Statistical cross-correlation operation allows the computation of average particle displacements in each interrogation window. This corresponds to the integer pixel location at which the correlation-map has the maximum value. The velocity vector can then be computed by dividing the displacement with the time-separation and image magnification. The entire sequence of events is shown graphically in figure 2.19.

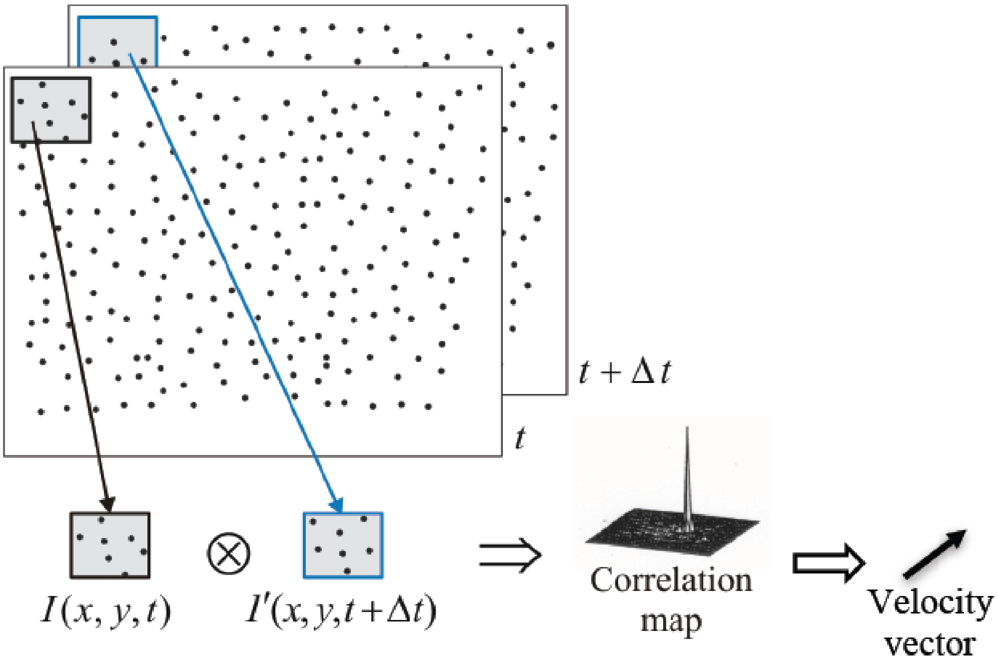

Figure 2.19: Schematic representation of image-windowing and cross-correlation to compute vector field (Scarano, 2013a)

Several guidelines are recommended that increase the probability of a successful measurement. Following these steps ensures that the time separation between exposures are chosen in such a way that the majority of particles are imaged in the same window in both exposure images. This ascertains that the number of particle image pairs are large enough for accurate cross-correlation analysis.

1. The maximum in-plane displacement should be smaller than one-fourth of the window size.

2. The maximum out-of-plane displacement should be less than the light sheet thickness. This condition is particularly important in experiments where the out-of-plane velocity component is strong.
3. The maximum in-plane variation of particle image displacements within an interrogation window should not exceed the particle image diameter. Multiple displacement peaks appear in the correlation map when this condition is not satisfied.

2.5.3 Studies on Particle Image Velocimetry (PIV)

Given the abundant literature available in the field of particle-image-velocimetry, studies summarized in this section are confined to only those that are directly relevant to the current investigation. A majority of these studies provide insight into possible ways of performing PIV measurements on internal flows and were helpful in the realization of the experimental setup used during the present measurements. For a more comprehensive and generic overview on studies done using PIV, the reader is directed to recent review articles by Scarano (2013b) and Westerweel et al. (2013).

PIV has been implemented successfully to study internal flows through pipes and channels. For measurements in geometries with curved inner and outer surfaces, optical access to the region of interest can be obtained by refractive-index matching of the solid model and the fluid. In these measurements, a view-box with flat walls surrounds the model. The box is filled with the same fluid that flows through the model but is in a quiescent state. The region of interest can be viewed without refraction errors from directions perpendicular to each face of the view-box. Budwig (1994) provides an excellent overview of solid and fluid systems that allow for refractive index matched measurements. A few are tabulated in table 2.3 and 2.4. Note, some values are missing as these were not reported by the author. Many liquids can be toxic and corrosive, and need to be handled with extreme care.

Material	RI (n)	Comments
Borosilicate glass	1.47-1.49	Available in sheets, tubes and rods.
Optical glass	1.45-1.96	Expensive and difficult to work with.
Acrylic	1.49	Plexiglass or Perspex.
Polycarbonate	1.58	-

Table 2.3: Properties of some model materials described in Budwig (1994)

Scholz et al. (2012) give an application of the refractive-index matching technique to quantify the flow field inside the intake port of an automobile combustion engine. The model was made using PMMA(acrylic) with a refractive index of 1.49 and a 62.5% aqueous solution of sodium iodide (NaI) was used as the matching fluid medium. The authors indicate some unfavorable properties of NaI solution and these are summarized below. It must be noted that refractive index matched experiments between acrylic and NaI have been performed successfully (for e.g. Uzol et al., 2002; Yuki et al., 2011), but it requires a careful selection of components of the test rig.

Material	RI (n)	ρ/ρ_0	μ/μ_0
Glycerin	1.33-1.47	1-1.26	1-1490
Aqueous Zinc Iodide solution	1.33-1.62	-	-
Aqueous Sodium Iodide solution	1.5	-	-
Aqueous Potassium thiocynate solution	1.33-1.49	1-1.39	1-2.4
Kerosene	1.45	0.82	-
Turpentine	1.47	0.87	1.49

Table 2.4: Properties of some matching fluids, ρ_0 and μ_0 are the density and absolute viscosity of water at $20°$ taken from Budwig (1994)

- The solution tends to decolorize into yellow-red when exposed to UV-light and/or oxygen. This red colour does not allow the green laser light to transmit through the medium.

- Sodium iodide is highly corrosive to ferrous metals. For example, they found that metallic screws were rusted and inoperative in less than two days.

- Sodium iodide tends to colour everything that it gets in contact with.

To circumvent using the method of refractive index matching, it is possible to minimize refraction errors by making use of models with extremely thin walls. Westerweel et al. (1996) measure the fully-developed turbulent-flow profile at a $Re = 5300$ using planar PIV. The test section was a square water-filled box enclosing a section of glass-pipe of inner diameter $40mm$ and thickness of $0.18mm$ ($t/d = 0.5\%$). This was sufficiently small to minimize errors due to wall curvature. van Doorne and Westerweel (2007) perform stereoscopic PIV measurements to measure the instantaneous velocity field for laminar and turbulent pipe flow of water. The light sheet is positioned perpendicular to the flow direction and the transverse cross-section of the pipe is the region of interest. The authors use a glass tube of thickness $1.6mm$ and internal diameter of $40mm$ ($t/d = 4\%$) within their view-box containing water. The authors mention that the errors due to wall curvature are maximum in regions that are very close to the boundary of the glass. Due to the difference in refractive index of the glass wall and water, the image of the particles are shifted by a constant value and can be estimated using Snell's law.

Mi et al. (2007) perform planar PIV measurements on a turbulent jet issuing from a round sharp-edged orifice plate into unbounded surroundings. The tests were performed at $Re = 72000$. They conclude from their measurements that the near flow-field is highly three-dimensional due to the upstream flow-separation point at the orifice inlet edge. The primary coherent structures are distributed asymmetrically from the centerline and occur close to the orifice (see figure 2.21). Comparison with previous hot-wire anemometer measurements indicates that similarity of mean-flow-field is achieved for $x \geq 8D$, while the turbulence field is far from similar even at $16D$ from the plate.

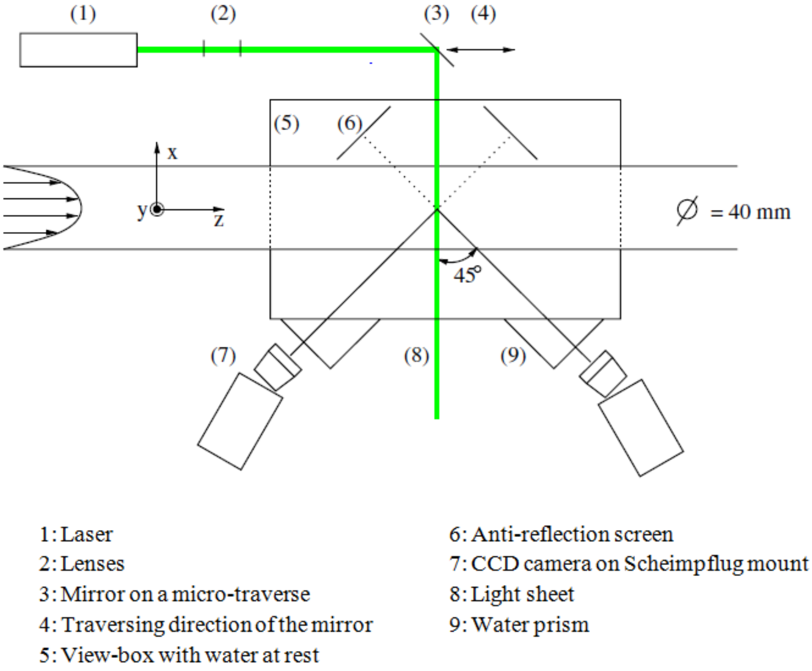

Figure 2.20: Schematic of the stereo-PIV system used by van Doorne and Westerweel (2007)

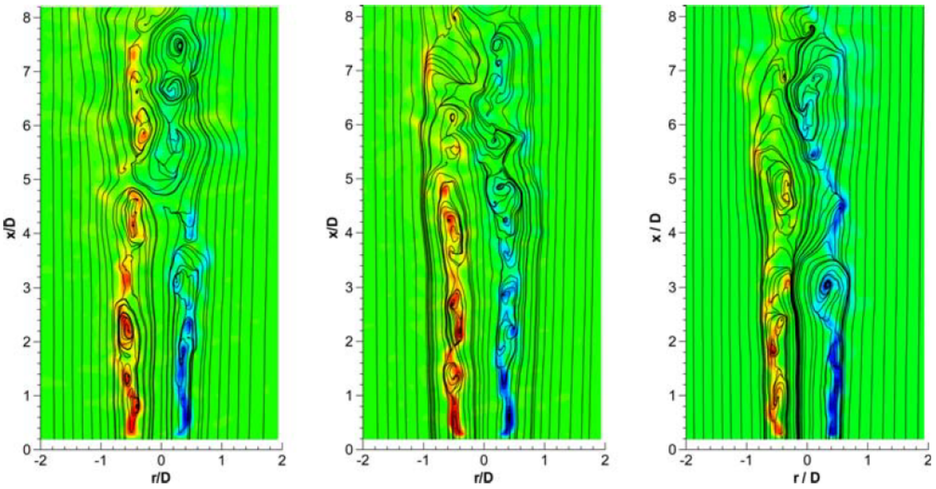

Figure 2.21: Instantaneous streamlines in the coordinate system translating at a speed of $0.6U_0$ reported by Mi et al. (2007). The flow exits a sharp edged single hole orifice into unbounded surroundings.

2.6 Summary

From the literature covered so far it can be established that the parameters affecting pressure losses over single and multi-hole orifice plates are:

- Nature of flow entering the device, defined using the pipe/hole Reynolds number. The pressure loss is also effected by the velocity profile of the incoming flow.
- The porosity or the equivalent diameter ratio is observed to be the most dominant factor affecting pressure losses.
- The thickness-to-hole-diameter ratio affects the behaviour of the flow within the orifice hole(s) and in turn influences the pressure losses.
- For multiple-hole orifices, the number of holes and its distribution on the plate also influence the pressure losses.

There have been many studies that investigate the influence of geometrical parameters on the pressure loss occurring in the flow through an orifice. It is known that the highest pressure loss is achieved using sharp-edged single-hole orifices, with increasing porosity leading to a decrease in losses. For a given hole diameter, increasing the plate thickness leads to reduction in pressure losses as the flow can re-attach within the orifice. A small increase is observed for very high plate thickness values due to viscous losses within the orifice holes.

The largest hydrodynamic pressure fluctuations are expected to occur close to the orifice, with one study showing that the fluctuating pressure reaches its peak value at about two pipe diameters from the plate. Since both hydrodynamic and acoustic pressure perturbations exist, the challenge lies in differentiating one from the other.

Studies on flow over the backward-facing-step configuration provides a nice visualization of the flow mechanisms involved during flow separation. Though the flow through a sharp-edged orifice is a confined jet, abundant literature on the backward facing step provides some interesting observations that can assist the current investigation.

Some features of Particle Image Velocimetry were highlighted that illustrates its strength for measuring turbulent separating flows. For measurements in internal flows, refractive index matched investigations can be performed, which requires a careful selection of the test components with many of the working fluids have unfavorable properties. An alternate approach is to employ models with extremely thin walls that minimize refraction errors occurring at the solid-fluid interface.

Chapter 3

Research methodology

Flow through orifices used in pipelines are a major source of vibration and the aim of the current research work is to aid development of a pressure-drop system, that produces minimum flow disturbances.

The variables of interest are first outlined in brief. The subsequent sections of this chapter gives an overview of the two measurement approaches taken towards the problem.

3.1 Parameters of interest

- **Pressure loss**
  Orifices are used to create a pressure loss and thus, it is important to quantify this variable during an analysis. This pressure loss depends on the orifice geometry and the incoming flow conditions, as discussed in the preceding chapter (see section 2.2).

- **Pressure fluctuations**
  The pressure fluctuations quantify the disturbances existing in the flow. Analysis of their spectral content will facilitate the understanding of the flow mechanisms involved. Data at several locations downstream will help understand the extent up to which these disturbances exist.

- **Velocity field**
  The fluid issuing from the orifice, is a strong, unsteady jet whose dynamics are expected to be the primary source of disturbance in the vicinity of the orifice plate. It is vital that a large portion of the downstream velocity field starting from the orifice exit is quantified effectively. Given the highly unsteady nature of the flow, it is essential to have time-resolved data.

3.2 Approach

This document describes a detailed analysis of turbulent flow of water through orifices in pipes. Given the low Mach numbers of the flow considered here, the fluid medium is taken as incompressible. Furthermore, only non-cavitating flow conditions are of interest in the present study.

The parameters mentioned in section 3.1 can be determined either numerically or experimentally. By selecting an experimental approach to the problem, setups that are capable of quantifying the variables of interest were designed and constructed. Two experimental campaigns, based on two different approaches to the problem were carried out. They are classified as:

1. **Pressure measurements approach**
   This approach involved measuring the pressure loss and the downstream wall pressure fluctuations created by the flow issuing through an orifice. Following the approach of Qing et al. (2006); Testud et al. (2007) the disturbances in the flow are measured directly using unsteady pressure sensors. This approach is detailed in chapter 4 and a portion of the results are presented soon after in chapter 5.

2. **Velocity measurements approach**
   The unsteady velocity field, up to several pipe diameters downstream of the orifice is measured using time-resolved, planar, Particle Image Velocimetry (PIV). The investigations are confined to a planar measurement of the vector field in the central longitudinal plane of the pipe. These measurements are meant to identify flow mechanisms and flow structures occurring in the downstream vicinity of the orifice. Furthermore, the generated experimental data can be used to validate RANS based CFD computations that are commonly used in industries.

PIV requires optical access to the region of interest and pressure sensors need to be mounted on the walls of the cylindrical channel. Thus, two separate test rigs were designed and constructed.

3.3 Hypothesis

Single-hole orifices are currently in use to generate pressure losses in fluid circuits. In addition to understanding the underlying physics of the flow emerging from single-hole orifices, the present investigation assesses the possibility of using multi-hole orifice plates as its replacement.

It is expected that multi-hole orifice plates of geometries comparable to single-hole orifice plates create lower disturbances in the flow as the flow structures associated with the former are smaller (multiple jets as opposed to one). It is hypothesized that these smaller flow-structures are less effective in imparting forces onto the surrounding structure and dissipate faster. Therefore, both single- and multi-hole orifice plates are investigated and a comparison between the two is made wherever possible.

3.4 Research questions

Some research questions that the present investigations aim to answer are:

- Can multiple-hole orifices create pressure losses comparable to the single-hole orifice? If yes, what criteria must be taken into account to achieve this? Are the resulting flow disturbance levels lower?
- What effect do the geometrical parameters governing orifices, have on the magnitude and extent of the flow disturbances they create?
- What flow features are characteristic of these devices? What flow mechanisms may be responsible for the large disturbance levels that are encountered while using single-hole orifices?
- To what extent does the flow remain separated? What would be a suitable length scale that could provide estimates for using a multi-stage pressure-loss system?

From the articles summarized in chapter 2, it is clear that many studies in the past have analysed geometrical parameters affecting pressure losses created by orifices. By simultaneously measuring both the pressure loss and wall pressure fluctuations for a wide range of geometries, the present study extends this available knowledge significantly.

Studies on pressure fluctuations created by orifices under non-cavitating conditions are limited. The flow conditions described in this document are different from those used in large industrial pipelines. Consequently, the magnitude of pressure fluctuations that are of interest here are much lower, though still significant for the current application in high-precision mechatronics.

This document also describes the successful implementation of PIV to study internal flows through orifices. To the author's knowledge, no previous PIV measurements on pipes containing orifices have been reported. This could perhaps be attributed to the complex nature of the PIV technique.

It is believed that the results described in this document will add to the understanding of these commonly used devices and ultimately support the development of an optimum pressure loss system.

3.5 Summary

This chapter outlined the research methodology that was implemented in the present study. The motivation to perform experimental investigations along with the parameters that are of interest were highlighted. Some research questions motivating the analysis described in this document were discussed.

The subsequent chapters describe the two measurement approaches and the associated results. The outline of this thesis can be found in section 1.2.

Chapter 4

Approach: Pressure measurements

4.1 Introduction

This chapter gives a detailed description of the pressure measurements performed on orifices in this study. A test setup to perform pressure-drop and unsteady pressure measurements was constructed and its details are first presented. A wide range of orifices were investigated and their geometries are outlined in section 4.3. Section 4.4 presents the classification of the experiments performed along with some preliminary results. The final section (see section 4.5) is devoted to describing the processing of the measured data.

4.2 Experimental setup for pressure measurements

The components of the setup used to perform pressure loss and wall pressure-fluctuation measurements are shown schematically in figure 4.1. Starting with a working overview of the entire setup, the subsequent subsections give a detailed description of the experimental apparatus used during these measurements.

4.2.1 Setup overview

A continuous flow of water is supplied by a pump which is channeled into the test section using connecting hoses. Within the test section, the fluid passes through an orifice plate. Sensors are positioned upstream and downstream of the orifice. The signals from the transducers are recorded using a data-acquisition-system. From the test section, the flow is channeled back to the pump reservoir using connecting hoses. A flow-meter and transparent-hose-pipe are included to measure the flow-speed and check for presence of air bubbles respectively. A differential pressure manometer measures the steady pressure difference between the flow inlet and outlet.

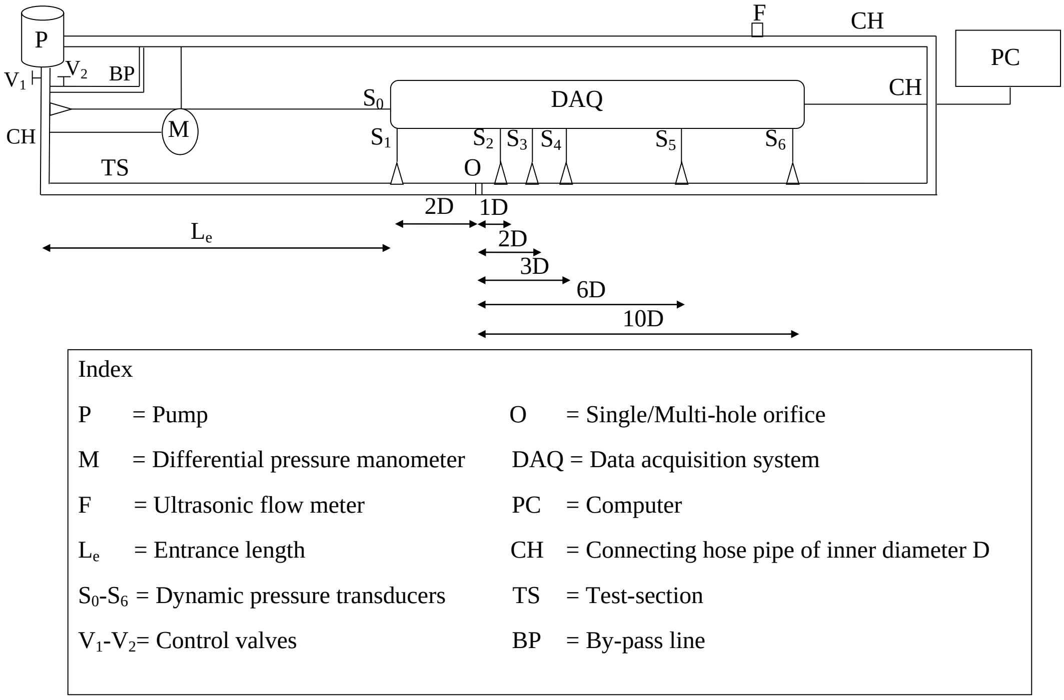

Figure 4.1: Schematic of the experimental setup used for pressure measurements.

4.2.2 Experimental instrumentation and arrangements

- **Pump and control valves:**
  A ten stage, multi-stage centrifugal pump supplies water at 22°. The flow from the pump is divided into two separate channels, one directed to the test section and the other through the by-pass line back to the pump reservoir. In addition to the electronic-flow-control which is part of the pump, ball-valves on each of the lines allow regulation of the flow between $0.5 - 3.0\ m/sec$ ($Re_p = 4500 - 27000$) into the test section. The maximum attainable flow-speed depends on the orifice in use. In the above mentioned Reynolds number range, the flow is expected to be **fully turbulent** (White, 2006).

- **Connecting hoses:**
  Flexible polyurethane (PU) hoses of internal diameter 9 mm and 1.5 mm wall thickness are used to connect the pump to the test section. A hose of length 13 m connects the supply side of the pump to the entrance of the test section (**supply hose**). Such a long hose length helps dampen the pressure pulsations arising from the pump (Qing et al., 2006). The effect of the pump is discussed in further detail in section 4.4.1.

  The flow from the test section is carried back to the pump by pipes spanning a length of 12 m. This includes 11 m of flexible polyurethane hose (**return hose**) and 1 m of stainless-steel pipe. The return hose comprises of a small section of transparent hose that is 1 m long. The stainless-steel pipe is introduced to mount the transducers of the ultrasonic flow meter and the transparent hose is included to check for air bubbles in the flow.

A by-pass hose connects the entrance of the supply hose to the exit of the return hose (see figure 4.1). The by-pass hose is provided to direct excess flow from the pump back to the reservoir.

- **Differential pressure manometer:**
  A digital differential pressure manometer, MONOX $D10000$ is connected to the supply hose on one side and to the return hose on the other. Table 6.1 outlines the specifications of the manometer.

  Within the setup, it determines the steady pressure difference between the flow at the entrance and exit thereby measuring the pressure loss occurring over the entire layout.

Property	Value
Dimensions	$150 \times 80 \times 30$ mm
Measurement range	$0 - 1000$ kPa
Accuracy	0.5% of measured value

Table 4.1: Specifications of the MONOX $D1000$ differential pressure manometer as reported by the manufacturer.

- **Test section:**
  The flow from the connecting hose enters the test section made of stainless steel. It has an internal diameter D of 9 mm (see figure 4.2). To ensure 1-way coupling between the flow and the structure (that is, not taking into account the effect of structural deformations on the flow), the test section is built with thick walls. The setup weighs about 7 kg such that the ratio of its mass to that of water inside is about $220 : 1$.

  The test section comprises of two segments that are fastened together using bolts. It can be operated without an orifice plate; or an orifice plate of external diameter D can be introduced between the two segments. The upstream segment is designed such that the flow is expected to reach fully developed conditions before entering the orifice. This entrance length for turbulent pipe flow is approximated using the following relation (Kundu et al., 2011)

$$L_e \approx 4.4 \times D \times Re_p^{1/6} \tag{4.1}$$

  Assuming that the maximum flow speed of interest is 3.5 m/sec, the above relation results in a length of 0.2 m. Since equation 4.1 is an approximate expression, a sufficient additional length is provided such that the total entrance length is 0.3 m. The length of the downstream section is 0.2 m.

  The test-section contains drilled geometries at specific locations to mount the pressure-sensors ($S_1 - S_6$). The dimensions of these holes are specified by the manufacturer of the pressure sensors.

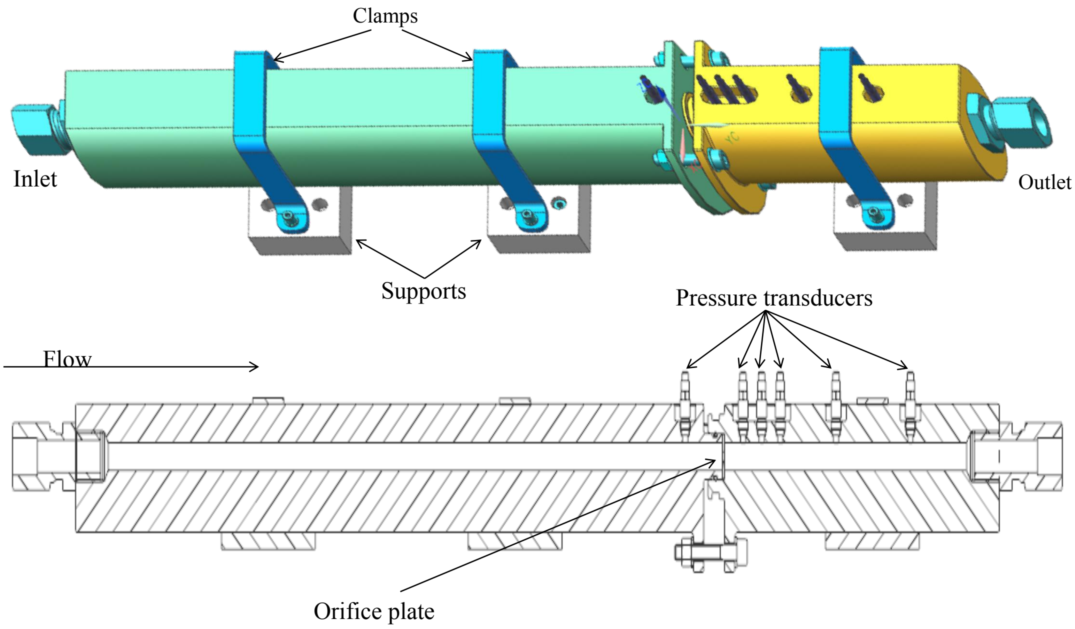

Figure 4.2: 3D model (top) and the cross-sectional view (bottom) of the stainless-steel test section depicting flush mounted pressure sensors and the orifice plate. ***Design courtesy ASML***.

The first section, contains one pressure transducer at a distance of $2D$ upstream from the orifice. This sensor is introduced to capture the base level fluctuations in the flow before it enters the orifice. The downstream section holds five sensors at distances of $1D$, $2D$, $3D$, $6D$ and $10D$ respectively from the orifice. Using insight from the investigations of Qing et al. (2006), the first three sensors are positioned such that the peak pressure fluctuations are expected to occur at one of these locations. The last two sensors are positioned to measure the downstream extent of disturbances in the flow.

Clamps help fasten the test section to movable supports that can slide on X-section beams. These beams are equipped with vibration isolation pads to dampen external disturbances.

- **Pressure transducers**
  Six PCB Piezotronics 105C02 ICP® sensors are used to measure time varying static-pressure of the flow inside the test section. These sensors have a high temporal resolution and belong to the sub-miniature, high-sensitivity class of pressure transducers supplied by PCB. The sensor has a stainless-steel housing with a sensing element of diameter 2.5 *mm* made of Quartz. Each sensor has an in-built amplifier and is connected to the data acquisition system using coaxial cables. Table 4.2 summarizes the specifications of the PCB sensor.

Property	Value
Sensitivity	7.3 mV/kPa
Maximum pressure	1720 kPa
Resolution	0.035 kPa
Resonant frequency	≥ 250 kHz
Rise time	≤ 2 μsec
Operating temperature range	$-73°C$ to $+121°C$

Table 4.2: Specifications of the PCB 105C02 reported by the manufacturer.

In addition to the six pressure sensors mounted on the test section, a KISTLER type-7261, dynamic-pressure sensor is recess-mounted on the inlet connecting hose (see S_0 in figure 4.1). By mounting a sensor close to the pump, its effect on the measurements can be ascertained.

- **Data acquisition system & Software**
  All sensor data are sampled and conditioned using a PAK MKII data acquisition system by Müller-BBM VibroAkustik Systeme GmbH. The system is controlled using the PAK 5.8 software.

- **Ultrasonic flow meter**
  A FLEXIM FLUXUS® F601 ultrasonic flow meter is used to measure the rate of flow within the setup. The flow meter has two transducers that send ultra sonic signals through the pipe. The signals emitted by the first transducer are reflected by the wall and received by the second transducer. These signals are emitted alternatively in and against the direction of flow. The transit time in the direction of the flow is shorter than that against the flow direction. Thus, the flow speed is determined by measuring the time difference between the signals travelling with and opposite to the flow, since the distance between the transducers are known. The working principle of the flow meter is depicted in figure 4.3 and its relevant specifications are tabulated in table 4.3

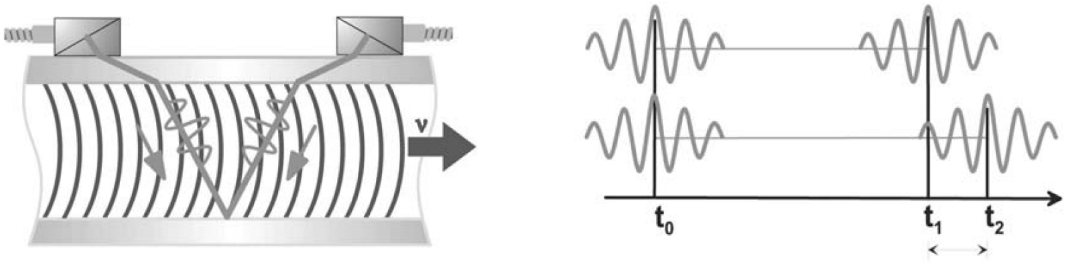

Figure 4.3: Illustration of the working principle of the ultrasonic flow meter as shown in its operating manual

The transducers of the flow meter are more effective in transmitting and receiving ultra-sonic signals when fixed to a stainless-steel pipe compared to a flexible polyurethane hose pipe. As a result, a small section of stainless-steel pipe is introduced in the return section of the test setup to mount the transducers of the flow meter.

Property	Value
Measurement range	$0.01 - 25\ m/sec$
Repeatability	0.15% of measured value
Accuracy	0.5% of measured value
Response time	1 *sec*

Table 4.3: Specifications of the FLUXUS® F601 ultrasonic flow meter reported by the manufacturer

4.3 Orifice geometries

The current investigations aims to understand the working of single-hole orifice plates in detail, and assess the possibility of replacing them with multi-hole orifices as pressure loss devices (see section 3.3). This section outlines the geometries of the single and multiple-hole orifice plates that were used in the pressure measurements.

4.3.1 Single-hole orifices

Table 4.4 categorizes the different single-hole orifice plates based on their geometries. These orifice plates are expected to produce a wide range of pressure losses when introduced in the test-setup (Miller, 1990; Idelchik, 2008). Furthermore, their specifications were selected such that the effect of geometrical parameters on their performance could be investigated. For instance, plates S1, S2, S3 and S4 have the same thickness to hole diameter ratio, but have varying porosities. On the other hand, plates S3, S6 and S7 can be used to analyze the effect of thickness to hole diameter ratio as these plates have the same porosity.

Plate label	Hole diameter $d_h(mm)$	Plate thickness $t(mm)$	Porosity β (%)	Thickness ratio t/d_h
S1	2	1.0	5	0.5
S2	3	1.5	11	0.5
S3	4	2.0	20	0.5
S4	5	2.5	30	0.5
S6	4	0.5	20	0.125
S7	4	2.5	20	0.625

Table 4.4: Geometries of the single-hole orifice plates used for pressure-measurements

4.3.2 Multi-hole orifices

Two different configurations of sharp edged orifice plates with multiple-holes drilled are tested in these investigations. They are the seven hole and nineteen hole orifice plates shown in figure 4.4. This configuration was selected based on the comprehensive study of Kolodzie and Winkle (1957) on multi-hole orifice plates. The holes are positioned in an equilateral triangle arrangement such that each hole is equidistant from its neighbouring holes and this distance is characterized by the pitch P_c.

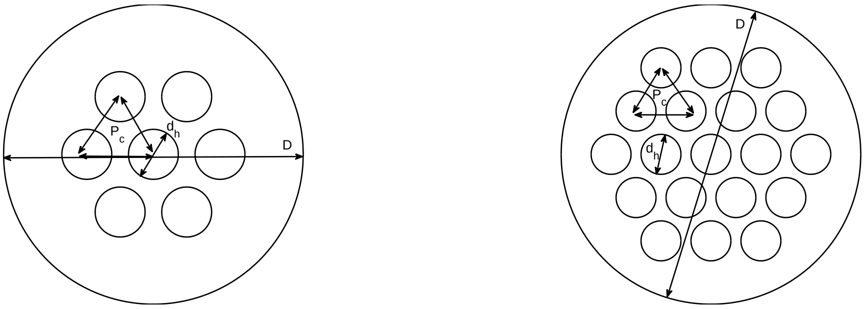

(a) 7-hole orifice plate **(b)** 19-hole orifice plate

Figure 4.4: Configuration of the sharp edged multi-hole orifice plates used in the present investigation.

Table 4.5 lists the geometries of the multi-hole orifice plates that were part of the pressure measurements. A few of these plates were designed such that their non-dimensional geometric variables ($\beta, t/d_h$) are similar to the single-hole orifices. This allows a comparison between the two. Additionally, a few extra plates were created to test the effect of thickness to hole diameter ratio and the number of holes in the plate.

Plate label	N_h	$d_h(mm)$	$t(mm)$	P_c (mm)	P_c/d_h	β (%)	t/d_h
M3	7	1.5	0.75	2.25	1.50	19.4	0.5
M4	7	2.0	1.0	3.0	1.50	34.6	0.5
M5	7	1.5	0.5	2.0	1.33	19.4	0.33
M6	7	1.5	2.0	2.0	1.33	19.4	1.33
M10	19	0.9	1.2	1.2	1.33	19.0	1.33
M11	19	0.9	3.0	1.2	1.33	19.0	3.33

Table 4.5: Geometries of the multiple-hole orifice plates used for pressure measurements

4.4 Experimentation

The experimental setup built for pressure measurements was described in section 4.2. The pressure measurements performed on flow through orifices can be broadly classified into:

1. **Preliminary investigations**
   These tests were aimed at checking the working of the test setup and identifying external factors that can effect measured data. The nature of these experiments and the associated results are described in section 4.4.1.

2. **Steady pressure loss measurements.**
   The aim of these experiments were to determine the pressure loss coefficient of the orifices listed in tables 4.4 and 4.5. The pressure loss created by an orifice plate in a pipe is characterized non-dimensionally by the loss coefficient K. It is the ratio of the steady pressure loss normalized by the mean dynamic pressure. In the current investigations, this parameter is calculated by measuring the pressure loss over the entire setup, with and without an orifice-plate. The difference between the two gives the orifice pressure loss and can be used to calculate the orifice loss coefficient as:

   $$K = \left(\frac{\Delta P_{with} - \Delta P_{without}}{\frac{1}{2}\rho U_p^2} \right) \tag{4.2}$$

   These experiments are aimed at quantifying the effects of Reynolds number and orifice geometry on the loss coefficient. They are performed along with wall pressure fluctuation measurements.

3. **Unsteady pressure measurements.**
   Flow disturbances at several downstream locations, arising from the fluid issuing from an orifice are recorded using axially positioned pressure sensors. The sensors measure unsteady pressure variations with high temporal resolution and allow spectral analysis to be performed on the recorded time series.

Results from the pressure drop and unsteady pressure measurements are discussed in chapters 5 and 8. The next subsection reports results from the preliminary investigations on the test setup.

4.4.1 Preliminary investigations and setup qualification

To examine the functionality of the newly built test rig, several tests were carried out. These were performed to inspect:

1. **Mounting and functioning of the pressure sensors**
   The mounting of the pressure sensors requires special attention. Since these sensors are flush mounted collinearly in the axial direction, a single badly mounted sensor can lead to erroneous data in the sensors following it. For instance, Qing et al. (2006) pick up a vortex-shedding frequency in one of their transducers, as the sensor upstream was protruding into the pipe.

The cavities for the transducers were drilled with high machining accuracy and were tightened carefully. Trial measurements are performed without an orifice and the recorded signals from all the sensors are analysed. Figure 4.5 illustrates the PSD computed from the recorded time series from all the sensors. Note that the curves are shifted by one order of magnitude with respect to the preceding curve otherwise they would overlap. To avoid misinterpretation, the y-axis label is disabled. Without looking too critically at the spectral content, it is clear that all sensors give a very similar response. This result verifies the proper mounting of the sensors.

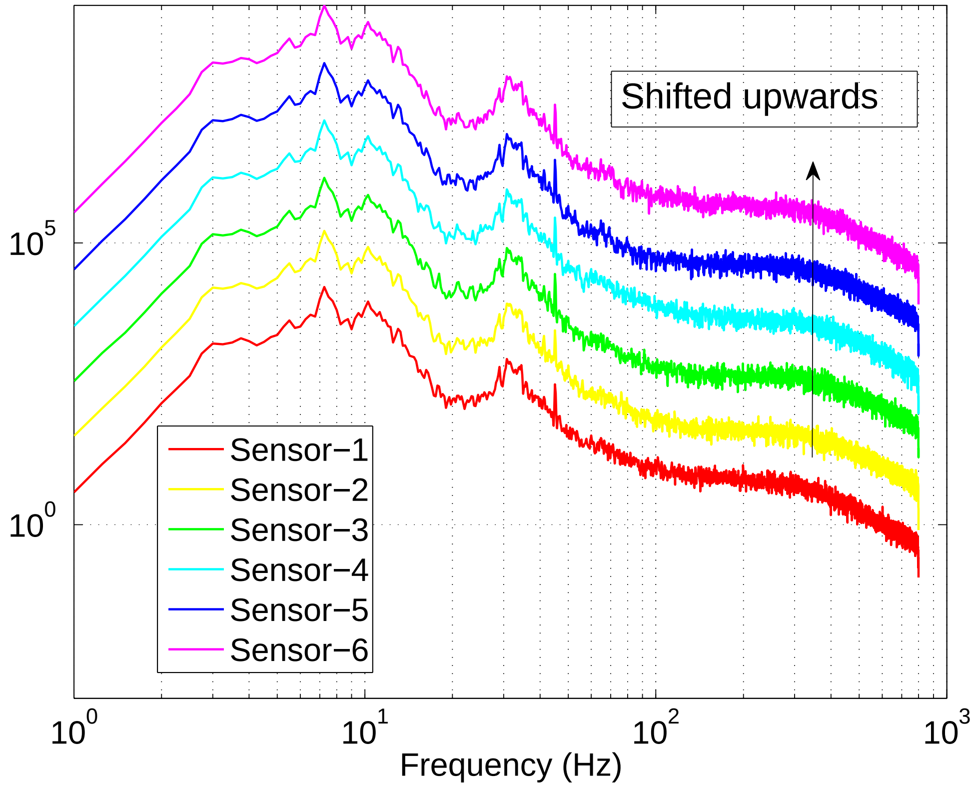

Figure 4.5: Plot of the fluctuating pressure PSD as a function of frequency for all six sensors obtained during trial measurements without an orifice in the test section. Note that the ordinate of each curve is shifted by one order of magnitude with respect to the previous curve. The y-axis label is disabled to avoid misinterpretation.

2. **Effect of external disturbances**

   The high sensitivity of the pressure sensors make them susceptible to external disturbances, for instance, mechanical vibrations arising from various sources that are transmitted through the ground. The vibration isolation pads at the base of the test setup are very effective in protecting the setup from these external disturbances. This was tested by simply striking the ground near the setup and observing the sensor response.

   However, an impulse force applied directly on the connecting hoses, appears clearly in the sensor readings. In this case, the disturbances travel through the fluid medium. Therefore, special care was taken to ensure that none of the setup components are disturbed during a measurement.

3. **Effect of the pump on the measurements**
   The rotating impellers of the centrifugal pump induces pressure pulses into the flow. The frequency at which this occurs depends on the operating power and therefore the R.P.M. of the pump. The identification of the corresponding peak frequency helps in determining the contribution of the pump towards the PSD curves. Since the R.P.M of the pump is known, the detection of the corresponding signals on the pressure sensors can also be viewed as a case to evaluate the working of the new sensors.

Pump power (%)	Pump R.P.M (-)	Pump frequency R.P.M/60 (Hz)	Measured frequency (Hz)
55	2387	39.7	39.5
50	2253	37.5	36.75
45	2119	35.3	33.5

Table 4.6: Pump R.P.M and the measured frequency peaks at different pump operating conditions

Tests without orifices in the setup are performed at all pump operating conditions. The data is sampled at 2048 Hz for a duration of 80 $secs$. Figure 4.6a shows sharp peaks at distinct frequencies in the PSD curves computed from the measured time series. For clarity, the data corresponding to three consecutive pump operating conditions are shown. It is evident that the measured frequency is very close to the R.P.M of the pump (see table 4.6). Furthermore, this peak is detected in all the sensors (see figure 4.5 at 45 Hz for example). Figure 4.6b depicts the measured frequency for all the pump operating conditions tested. The pump also contributes to a very low frequency peak < 10 Hz (for e.g. at 7.5 Hz in figure 4.5). This low frequency peak however doesn't present any defined behavior. Comparison of the pressure spectra from the sensor placed near the pump and the first sensor at the setup reveals that the magnitude of the pump disturbances are dampened significantly. Despite being present, in most cases they aren't discernible when an orifice is introduced in the test setup. In other cases, they are identified using information from the sensor placed close to the pump.

4.4.2 Flow conditions

The present investigations are aimed at studying turbulent flow of water through orifices. Water at 22°C enters the orifice under fully developed conditions. The mean flow in the pipe is varied between $0.5 - 3$ m/sec which corresponds to a Re_p between $4500 - 27000$.

The increment in the mean flow speed is about 0.25 m/sec and is set such that the Re_p values corresponding to those specified in table 4.7 are reached. The highest attainable flow speed however, depends on the orifice in use since the pump power is limited. The values tabulated in table 4.7 are chosen such that analogous flow conditions are present during PIV experiments (see section 6.4.4).

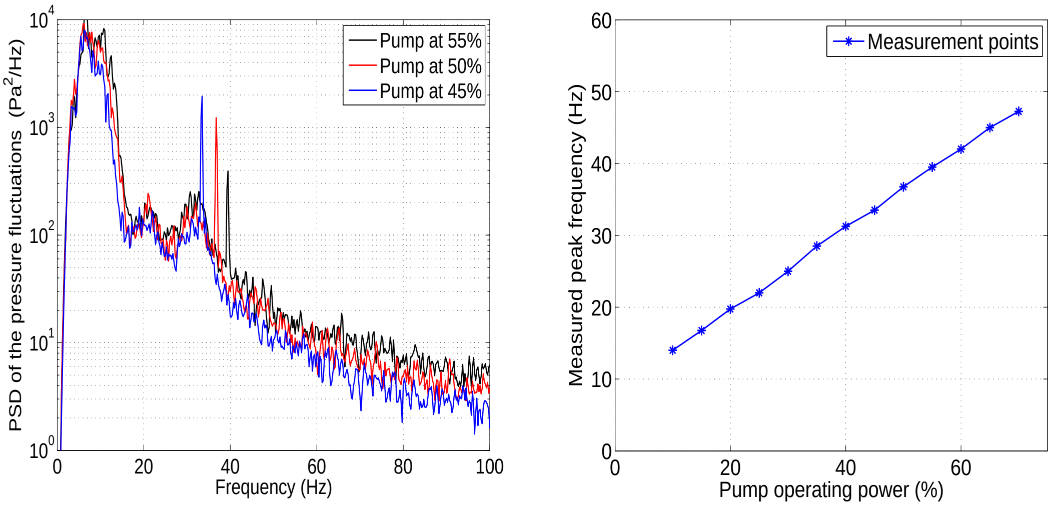

(a) Fluctuating pressure PSD as a function of frequency measured at the first transducer

(b) Peak frequencies observed at different pump operating conditions

Figure 4.6: Figures illustrating the pump frequency detected by the pressure sensors.

Serial number	Re_p
1	4100
2	6300
3	8350
4	10500
5	12500
6	14600
7	16800
8	18000
9	20200
10	22500
11	27000

Table 4.7: Pipe Reynolds number (Re_p) of the flow conditions used during pressure measurements

To facilitate comparison between the orifice plates, a few additional cases are tested such that the hole Reynolds number (Re_h) in the orifice has values tabulated in table 4.8. A complete overview of the flow conditions used for each of the orifice plates are described in appendix B.

4.4.3 Data acquisition and measurement parameters

The instruments used during the experiments were described in section 4.2.2. They are the differential pressure manometer, the ultrasonic flow-meter and the pressure sensors. During each measurement, data output from the manometer and the flow meter are recorded manually. The pressure-sensors are controlled using the PAK signal conditioner

Serial number	Re_h
1	15000
2	25000
3	35000
4	50000

Table 4.8: Selected hole Reynolds number (Re_h) for additional test cases used during pressure measurements

and PAK data acquisition software. The sensor calibration data, measurement duration and sampling rate are specified before a measurement. Each sensor acquires data at a rate of 2048 Hz for a duration of 82 seconds. Table 4.9 summarizes the data-acquisition parameters.

Property	Value
Sampling rate	2048 Hz
Sampling duration	82 s
Total number of measurement values	167936

Table 4.9: Data acquisition parameters used during pressure measurements

4.4.4 Testing procedure

The following are the typical steps that are followed during a measurement.

1. The orifice to be tested is introduced in the test setup. All connections are checked and the pump is turned on. The pump is increased to its maximum safe operating power to check for the maximum attainable flow speed with a given orifice plate.

2. Before setting the first flow condition of interest, water at a high flow rate is forced through the setup for about 15-20 minutes. During this process, the control valves are partially opened and closed. This action allows flushing out of all the air bubbles through the pipes which can be seen in the transparent section of the pipe.

3. Starting with the highest flow speed to be measured, each of the flow cases listed in the testing matrix (see section B) are set in succession.

4. At each flow case, sufficient time is allowed for the flow rate to settle. Soon after, data from the manometer is noted and the data from the pressure sensors are recorded. Each measurement typically takes 8-10 minutes.

5. At the end of all the measurements on an orifice, the water in the setup is drained and the next orifice is introduced.

6. The above mentioned steps are also performed without an orifice so as to determine the steady pressure loss occurring over the test setup for computing the loss coefficient.

4.5 Signal processing

This section describes the steps that are taken to process the signals recorded by the pressure sensors. The results are discussed in chapters 5 and 8.

The output from each sensor is a time series of fluctuating pressure. The signal sampled at $f_s = 2048\ Hz$ lasts $82\ s$. The signal shown in figure 4.7a is used to illustrate the steps taken to compute the power-spectral-density (PSD). Note, this is the same signal that leads to the blue PSD-curve shown earlier in figure 4.6a corresponding to the pump operating at 45 %.

Time block

The entire signal is divided into time-blocks of $4\ s$ each (see figure 4.7b). This leads to a frequency resolution of $0.25\ Hz$.

Windowing

To avoid errors due to spectral leakage, the time series to be transformed is multiplied by a window function before implementing Fast-Fourier-Transform. A Hanning window function as shown in figure 4.7c is used in the present computations. The effect of windowing on the time block can be seen in figure 4.7d.

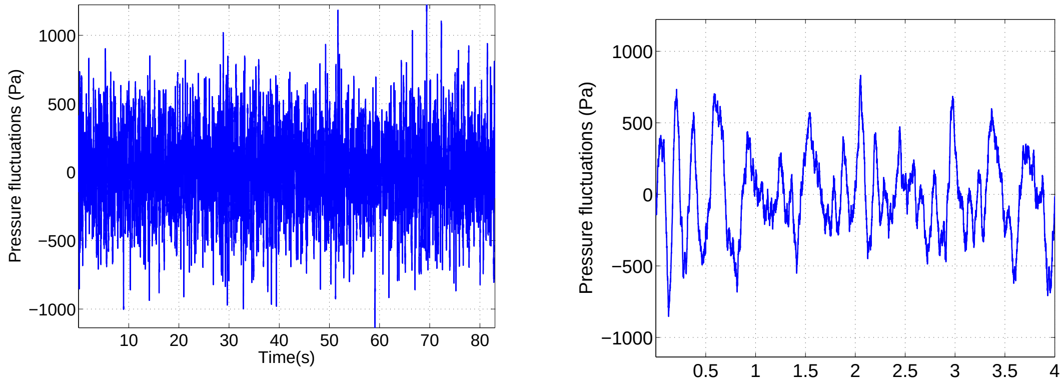

(a) Example of a time series recorded by the first pressure sensor

(b) A single time block lasting $4\ s$

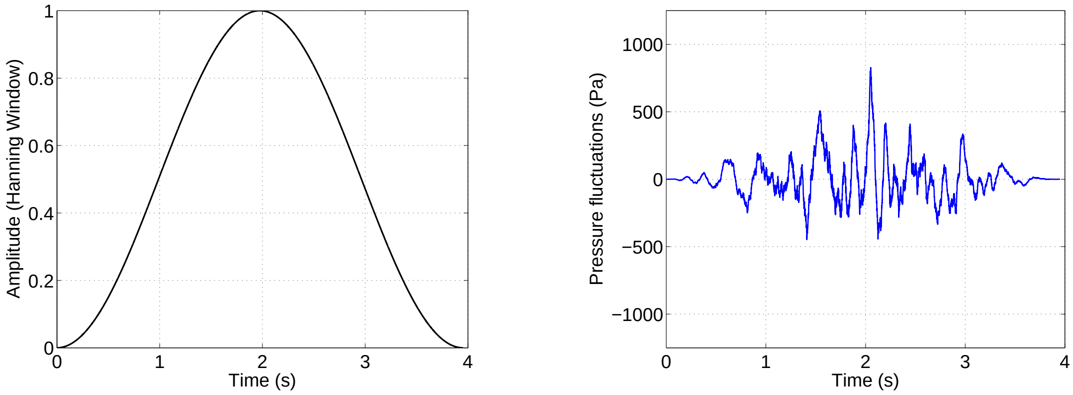

(c) Hanning window function

(d) Time block after windowing

Figure 4.7: Illustration of windowing on a single time block

Power spectral density (PSD)

The power-spectral-density decomposes the content of a signal over different frequencies present in the process. It describes how the energy is distributed over its frequency components and helps identify periodicity. Mathematically it is computed as,

$$G_{pp}(f) = \frac{2}{T}|p^*(f).p(f)| \tag{4.3}$$

Where, $p^*(f)$ is the complex conjugate of the fourier transform $p(f)$, which for a given time signal $p(t)$ can be computed by,

$$p(f) = \int_0^T p(t)e^{i2\pi ft}.dt \tag{4.4}$$

Averaging

Since windowing leads to attenuation of the edges of the signal, the power spectral density calculated from each time-block, is averaged. This results in a good statistical representation of the PSD. This can be seen clearly in figure 4.8.

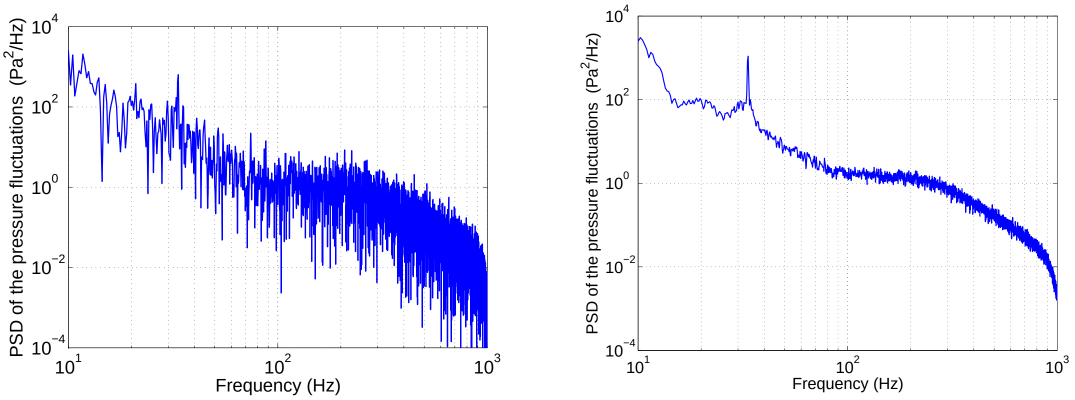

(a) Power spectral density computed from 1 time block.

(b) Power spectral density after averaging using all the time blocks.

Figure 4.8: Effect of averaging on spectral content.

The above mentioned operations are performed using PAK data-processing software and MATLAB. Once the PSD curves are obtained, its spectral content can be analysed closely to identify distinctive features. In the current example, a peak at 33.5 Hz, corresponding to the pump R.P.M. is clearly detected (refer section 4.4.1).

4.6 Summary

This chapter described the experimental setup and the instruments used during pressure measurements on orifice plates (section 4.2). The orifice geometries and the flow conditions that were tested were presented in sections 4.3 and 4.4 respectively. Measurement parameters and steps taken for signal processing were outlined in sections 4.4.3 and 4.5 respectively. Results from preliminary tests done to qualify the functioning of the test setup were detailed in section 4.4.1. Chapters 5 and 8 are dedicated to analyzing the results obtained from the pressure measurements described in this chapter.

Chapter 5

Results: Pressure measurements

5.1 Introduction

The test setup and the orifice geometries used were presented in the preceding chapter (see section 4.2 and 4.3 respectively). An overview of the testing procedure implemented was described in section 4.4.4.

This chapter presents results from pressure measurements on single and multiple-hole orifice plates. The first section describes the outcome of the steady pressure loss measurements occurring over the test section. The subsequent sections analyze the orifice pressure loss and pressure fluctuation characteristics and are aimed at understanding the effects of Reynolds number and geometrical parameters. The final section compares the single hole orifice to the multiple hole orifice.

5.2 Steady pressure loss over the test section: No orifice

The pressure loss created by an orifice is quantified in non-dimensional form using the loss coefficient K as,

$$K = \left(\frac{\Delta P_{with} - \Delta P_{without}}{\frac{1}{2}\rho U_p^2} \right) \tag{5.1}$$

To compute K from the above mentioned equation, it is first essential to determine the pressure loss over the entire setup when no orifice is placed ($\Delta P_{without}$). This value can then be subtracted from the pressure loss occurring with the orifice present in the test section (ΔP_{with}).

Figure 5.1a shows the measured steady pressure loss occurring over the test section as a function of the flow speed, without an orifice. The viscous pressure loss ΔP_l of fully developed, turbulent flow occurring in a pipe of diameter D over a length L is usually expressed as,

$$\Delta P_l = f \times \frac{L}{D} \times \frac{\rho U_p^2}{2} \tag{5.2}$$

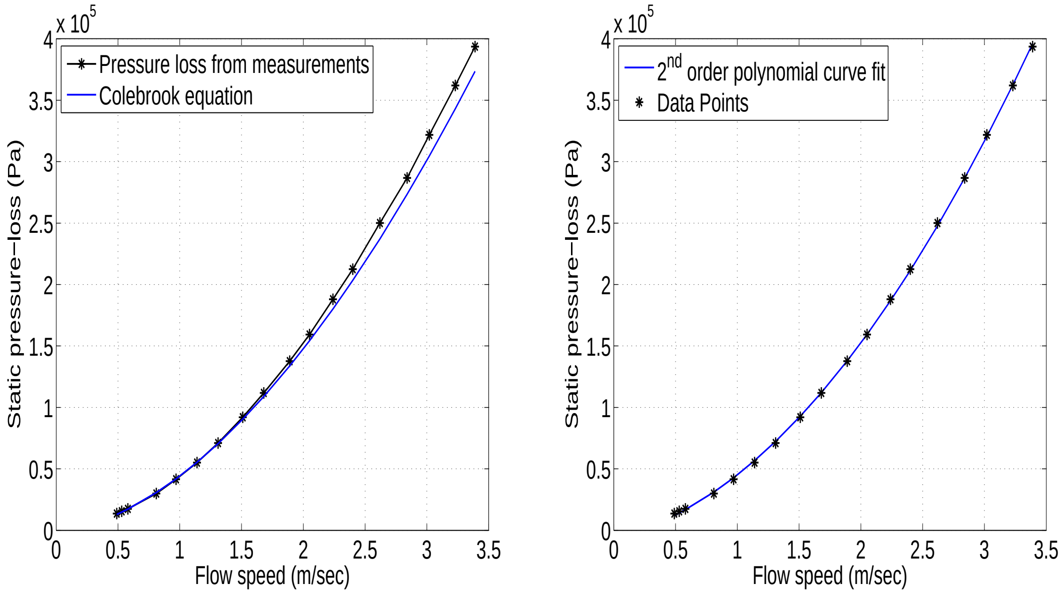

(a) Pressure loss as a function of the flow speed. **(b)** Polynomial curve fit through measured data

Figure 5.1: Figures illustrating the steady pressure loss occurring over the test section *without* an orifice.

where f is the friction factor. For turbulent pipe flow, the friction factor depends on the Reynolds number Re_p and the surface roughness ϵ. The implicit expression (based on extensive experiments) relating the friction factor to Reynolds number and surface roughness is known as the Colebrook equation (Cengel & Cimbala, 2006).

$$\frac{1}{\sqrt{f}} = -2 \times \log_{10}\left(\frac{\epsilon/D}{3.7} + \frac{2.51}{Re_p\sqrt{f}}\right) \tag{5.3}$$

For smooth hose pipes, the surface roughness can be assumed to be zero. Using the dimensions of the pipes used in the setup (see section 4.2.2), the Colebrook equation is solved numerically to obtain the friction factor. The measured pressure losses are thus compared to those obtained using equations 5.3 and 5.2 in figure 5.1a.

From figure 5.1a, it is clear that the numerical and measured pressure losses match fairly well. Minor observable differences are seen at higher flow speeds. This is perhaps due to the fact that the numerical calculation does not take into account the effect of pipe connections used in the setup. Furthermore, it also assumes that the flow is fully developed throughout.

The pressure loss varies quadratically with the flow speed. Figure 5.1b presents a second order polynomial curve-fit over the measurement points. The polynomial function has the form,

$$\Delta P_{without} = a_1 U_p^2 + a_2 U_p + a_3 \tag{5.4}$$

Where, the coefficients are,

$$a_1 = 2.8311 \times 10^4 [Pa.s^2/m^2]$$
$$a_2 = 2.2558 \times 10^4 [Pa.s/m]$$
$$a_3 = -0.5797 \times 10^4 [Pa]$$

Equation 5.4 can now be used as a measure of the steady pressure loss occurring over the test setup for flow speeds between $0.5 - 3.4\ m/sec$.

5.3 Single-hole orifice

Once orifices are introduced in the setup, the pressure loss they create are noted. These are described for each orifice and at each flow condition in appendix B. Equation 5.4 is then used to subtract the contribution of the viscous pressure losses occurring over the setup.

Figure 5.2 presents the magnitude of the pressure loss as a function of the flow speed, created by each of the single hole orifices. It is evident that for a given flow speed, the orifice with the smallest porosity creates the largest pressure loss.

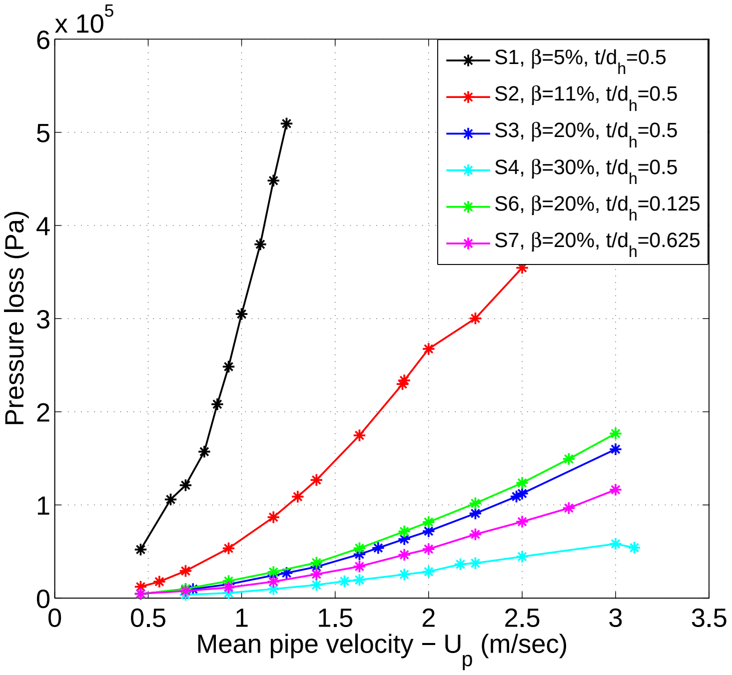

Figure 5.2: Plot of the steady pressure loss as a function of the mean flow speed for all the single-hole orifices tested.

Besides S1, the pressure loss appears to scale quadratically with the flow speed for all other orifices. This becomes evident when the magnitude of the pressure loss is normalized by the mean dynamic pressure ($\frac{1}{2}\rho U_p^2$), to get the orifice loss coefficient.

5.3.1 Effect of Reynolds number on the loss coefficient

Figures 5.3a and 5.3b present the variation of the loss-coefficient as a function of pipe and hole Reynolds number respectively for all the orifices tested. By comparing these curves to the Reynolds number effect reported in literature (see figure 2.4 in section 2.2), the following conclusions can be drawn:

- The loss coefficient of the majority of the orifices tested (S2 to S7) belong to the self similar region (also see figure 5.4 which focuses on plates S3-S7 having a loss coefficient below 50). In this region, the loss coefficient of a given orifice is independent of Reynolds number or the pressure loss is directly proportional to the square of the flow speed. This behavior also indicates that for the flow conditions tested, these orifices are not cavitating.
- For $Re_p > 7000$ (or $Re_h > 35000$), orifice-S1, shows trends expected in region-3. A sharp increase in the loss coefficient value indicates onset of cavitation. Whistling sounds emitting from the orifice corroborates this conclusion (Testud et al., 2007). This interesting phenomenon is discussed separately in sub-section 5.3.3.
- The loss coefficient plotted as a function of Re_p or Re_h presents the same trends, as remarked earlier by Malavasi and Messa (2011).

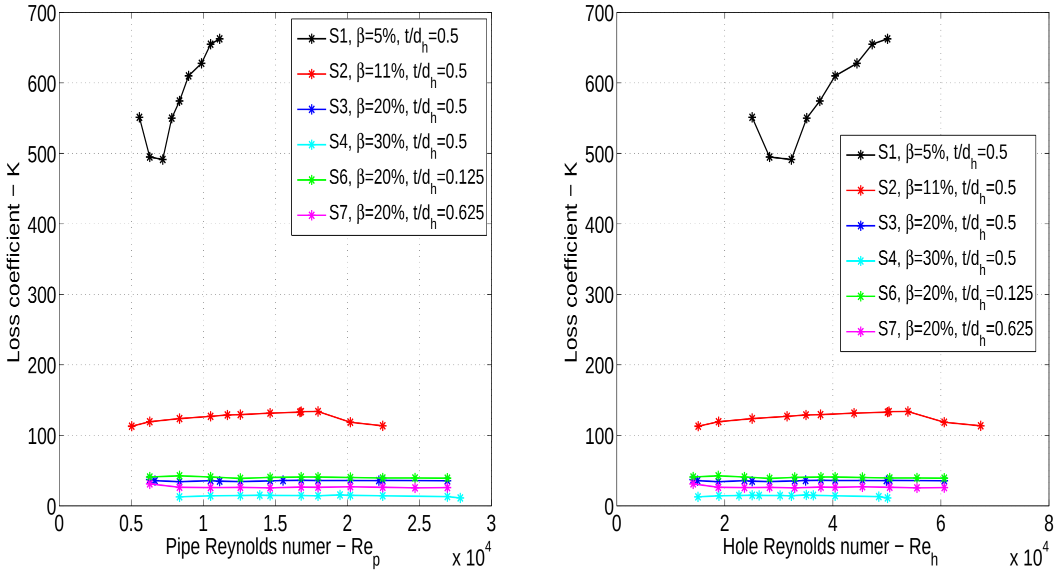

(a) Plot of the loss coefficient as a function of Re_p. **(b)** Plot of the loss coefficient as a function of Re_h.

Figure 5.3: Figures illustrating the effect of Reynolds number on the loss coefficient for all the single-hole orifice plates tested.

Table 5.1 summarizes the loss coefficient values in the self-similarity range for all the single-hole orifice plates. These values can be used to observe the variation in the measured loss coefficient as a result of changing geometric variables. Note, subsequent discussions will focus only on the non cavitating orifices. The cavitating orifice S1 is discussed separately at the end of section 5.3.3.

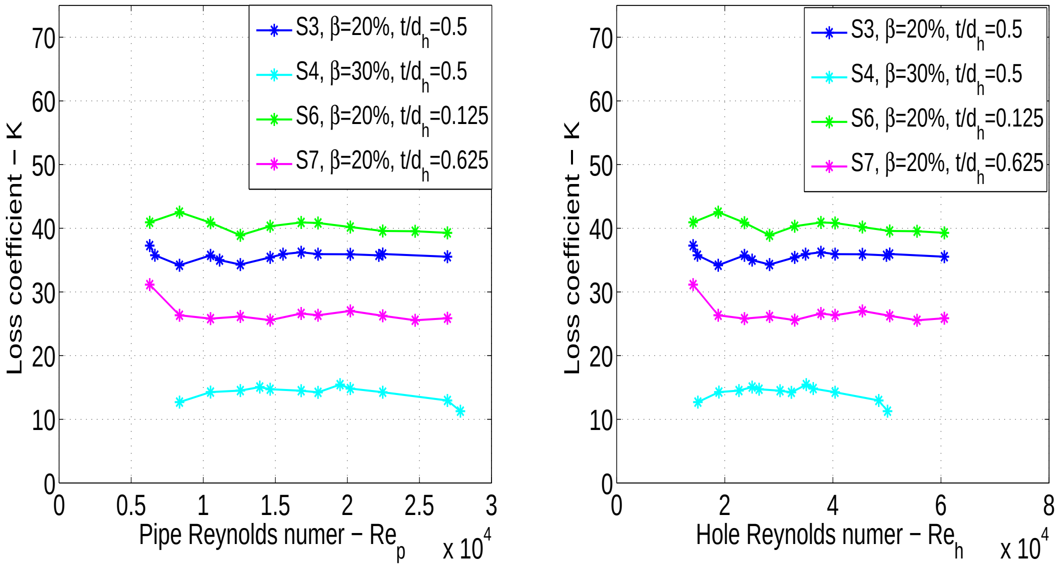

Figure 5.4: Plot of the loss coefficient (K) as a function of Re_p (left) and Re_h (right), for plates S3-S7.

Plate label	Porosity β (%)	Thickness-ratio t/d_h	Loss-coefficient K
S1	5	0.5	500
S2	11	0.5	124
S3	20	0.5	36
S4	30	0.5	14
S6	20	0.125	40
S7	20	0.625	26

Table 5.1: Average loss coefficient values in the self-similar region for all the single-hole orifices tested.

5.3.2 Effect of geometry on the loss coefficient

In the self similar region, the loss coefficient is independent of Reynolds number. This implies that the parameters governing the orifice geometry are solely responsible for the observed change in loss coefficient. This allows a comparison of the present results with standard industrial references like Miller (1990) and Idelchik (2008).

Idelchik (2008) provides an empirical relation between the loss coefficient (K_i[1]) and the geometrical variables effecting the loss coefficient, valid in the range of flow conditions used in the present investigation. These are based on observations from a series of experiments spanning several years. For a given plate porosity β and thickness to hole diameter ratio

---

[1] The symbol 'i' is introduced here to indicate Idelchik (2008)

(t/d_h),

$$K_i = \left[0.5\,(1-\beta)^{0.75} + \tau\,(1-\beta)^{1.375} + (1-\beta)^2 + \left(\epsilon \times \frac{t}{d_h}\right)\right]\left[\frac{1}{\beta}\right]^2 \tag{5.5}$$

where,

$$\tau = (2.4 - (t/d_h)) \times 10^{(-\phi)}$$
$$\phi = 0.25 + \frac{\left(0.535 \times (t/d_h)^8\right)}{\left(0.05 + (t/d_h)^7\right)}$$

Effect of plate porosity

The plate porosity is the most dominant factor effecting pressure losses. Figure 5.5a shows the effect of porosity on the loss coefficient. The results are based on the loss coefficients of plates S1, S2, S3 and S4 which have the same t/d_h of 0.5. Since the thickness-to-hole-diameter ratio is constant among these plates, the change in the loss coefficient depicted here is only due to the change in plate porosity.

The data shows the expected trend of decrease in the loss coefficient for an increasing plate porosity and for a given t/d_h ratio. Results from the present measurements match quite well with those reported by Idelchik (2008). The curves indicate that between $1-20\%$ the loss coefficient drops sharply. Thereafter, for plate porosity values between 20% and 80% the decrease is less severe.

Effect of plate thickness to hole diameter ratio

The thickness ratio is expected to effect the behavior of the flow within the hole of the orifice. For increasing t/d_h ratios, the flow initially separated at the sharp inlet, is expected to reattach locally inside the orifice hole.

Figure 5.5b depicts the loss coefficients of plates S3, S6 and S7. All these plates have a porosity of 20%, and differ only in their respective t/d_h values. As a result, the change in the loss coefficient shown here is only due to the change in plate thickness to hole diameter ratio.

The measured values match reasonably well with those obtained using equation 5.5. Overall, the t/d_h ratio has a relatively minor effect on the loss coefficient, with predominant variations occurring at lower t/d_h values. The reduction in pressure losses are expected to occur till the flow reattaches completely inside the orifice hole. These results are in accordance with past observations that were summarized in section 2.2.

5.3.3 Wall pressure-fluctuations

The time series recorded by each pressure sensor is transformed to the frequency domain. This is then used to compute the power-spectral-density (PSD) (see equation 4.3 in section 4.5). A detailed discussion of the spectral content is presented in chapter 8. In the present section, some general characteristics of the pressure fluctuations are highlighted. In the frequency domain, the root-mean-square (R.M.S) of the pressure fluctuations P'_{rms} can be computed using the power spectral density $G_{pp}(f)$ (Qing et al., 2006) as,

$$P'_{rms} = \sqrt{\int_{-\infty}^{\infty} G_{pp}(f)df} \tag{5.6}$$

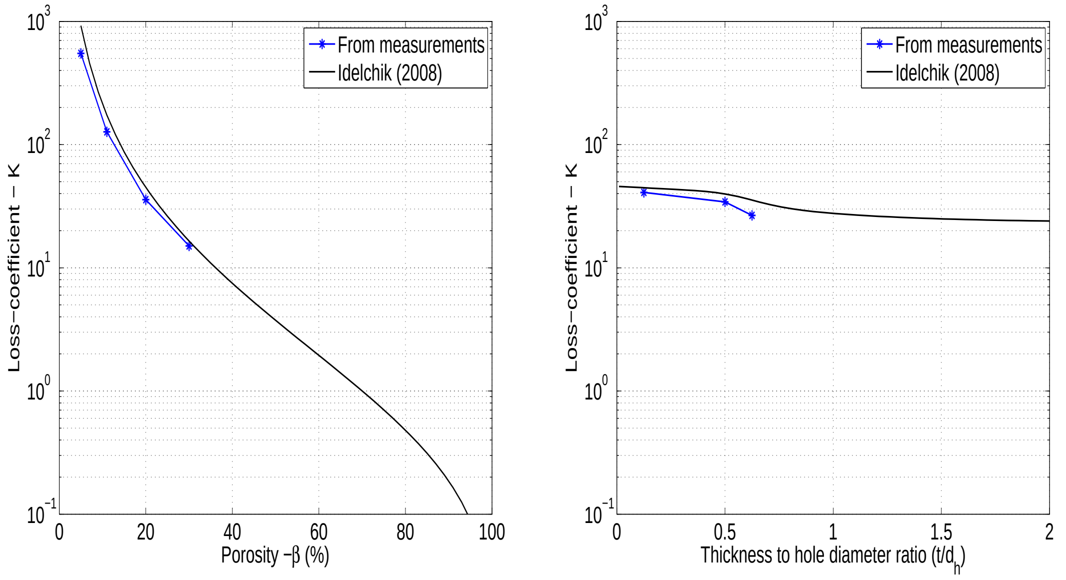

(a) **(b)**

Figure 5.5: Plot of the loss coefficient (K); (left) as a function of the plate porosity (β) for all plates with $t/d_h = 0.5$ and (right) as a function of the thickness to hole diameter ratio (t/d_h) for all plates with $\beta = 20\%$.

Figures 5.6 and 5.7 presents the variation of P'_{rms} measured at different axial locations, for different orifices at several flow speeds. The axial distances (x/D) are relative to the orifice position ($x = 0$), with positive values downstream. Qualitatively, these results are similar to those reported by Qing et al. (2006). The following are some observations based on these results:

- **Scaling**

  At each location, P'_{rms} scales with the mean dynamic-pressure ($\frac{1}{2}\rho U_p^2$). This scaling collapses all the measured values at different flow speeds on top of each other, for each orifice. Thus, both the pressure loss ΔP, and P'_{rms}, scale with the square of the mean flow speed and in turn with each other.

- **Pressure-fluctuation levels**

  In the range of the flow conditions and orifices tested, $P'_{rms}/(\frac{1}{2}\rho U_p^2)$ attains a maxima between 1-2D downstream from the orifice. This location is a function of the orifice geometry and is seen to remain fairly independent of the flow speed.

  In most cases, the R.M.S of the pressure fluctuation levels at 6D downstream appear comparable to the upstream pressure fluctuation levels. However, the pressure fluctuation levels upstream ($-2D$) from the orifice also appears to change with changing orifices. This observation can be attributed to the effect of acoustic waves that propagate in both directions from the orifice (Testud et al., 2009; Lacombe et al., 2013). Norton and Bull (1984) mention that as a result of the acoustic field the power spectral densities of the fluctuating wall pressure field are increased over those of undisturbed fully-developed turbulent pipe flow.

- **Effect of porosity**
  Comparison of figures 5.6a, 5.6b and 5.7b shows that for a given t/d_h, the orifice with the smallest porosity (S2), has the highest magnitude of the normalized P'_{rms}. For a given flow speed, velocity in the core of the orifice jet scales inversely with the plate porosity, thus, this trend is consistent. The point where the peak in pressure fluctuations occur moves downstream with decreasing plate porosity.

- **Effect of thickness to hole diameter** (t/d_h)
  Figures 5.7a, 5.7b and 5.7c illustrate the effect of plate thickness to hole diameter on the RMS of the pressure fluctuation levels. The magnitude of the normalized P'_{rms} decreases with increasing t/d_h. An increase in plate thickness is expected to stabilize the orifice jet, which for sufficiently large thickness ratios can reattach within the hole of the orifice.

The above mentioned observations are compared to observations from the flow-field resulting from the PIV measurements. This is discussed in section 7.3.3 of chapter 7.

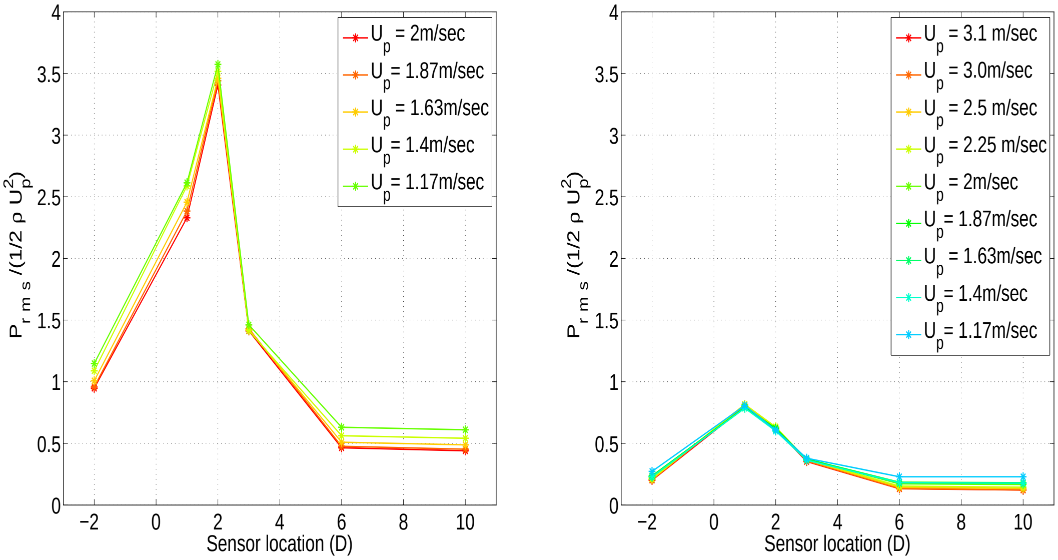

(a) Plate S2, $\beta = 11\%$, $t/d_h = 0.5$ **(b)** Plate S4, $\beta = 30\%$, $t/d_h = 0.5$

Figure 5.6: Figures illustrating the axial variation of $P'_{rms}/(\frac{1}{2}\rho U_p^2)$ for different single-hole orifice plates

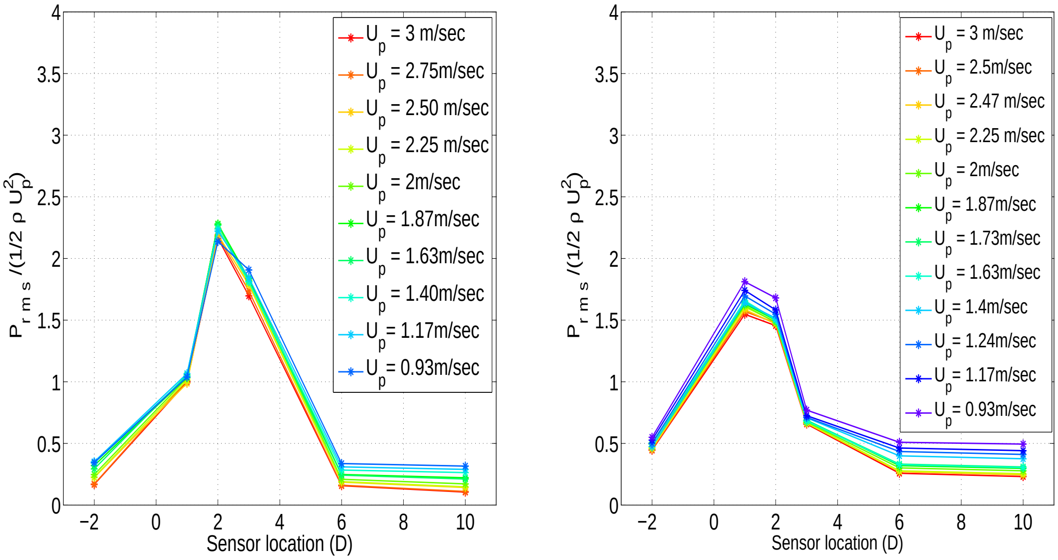

(a) Plate S6, $\beta = 20\%$, $t/d_h = 0.125$

(b) Plate S3, $\beta = 20\%$, $t/d_h = 0.5$

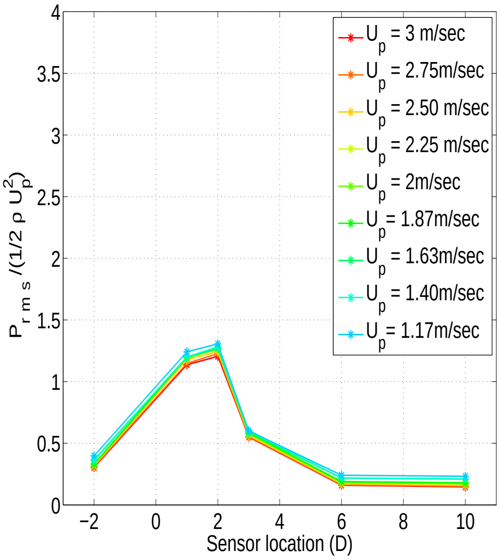

(c) Plate S7, $\beta = 20\%$, $t/d_h = 0.625$

Figure 5.7: Figures illustrating the axial variation of $P'_{rms}/(\frac{1}{2}\rho U_p^2)$ for single-hole orifice plates of porosity 20%.

Whistling orifice - S1

Before looking at the multiple-hole orifices, this section digresses briefly to discuss a few interesting features of orifice S1. It was remarked in section 5.3.1 that the K versus Re curve of the orifice S1 showed a behaviour (see figure 5.3) representative of cavitation (Malavasi & Messa, 2011). Furthermore, whistling sounds emanating from the orifice were heard during measurements.

To quantify this phenomenon, experiments on this orifice were repeated at a sampling rate of 25.6 kHz for several flow conditions. Figure 5.8 presents the power-spectral-density of the recorded time series as a function of the Strouhal number at a flow speed of 1 m/sec. The Strouhal number is defined using the plate thickness (t) and hole velocity (U_h) as the length scale and velocity scale respectively. This definition is commonly used for whistling orifices (Testud et al., 2009).

Each sensor in figure 5.8 shows a sharp, distinct peak at $St \approx 0.2$ (also see table 5.2). Furthermore, the magnitude of this peak is the highest in the upstream sensor (sensor-1) which indicates that the frequency is due to an acoustic effect. Studies on whistling orifices in air and water have reported the whistling frequency to occur at $St \approx 0.2$ (Moussou et al., 2007). In case of flow of water through orifices, whistling occurs only during cavitation (Testud et al., 2007).

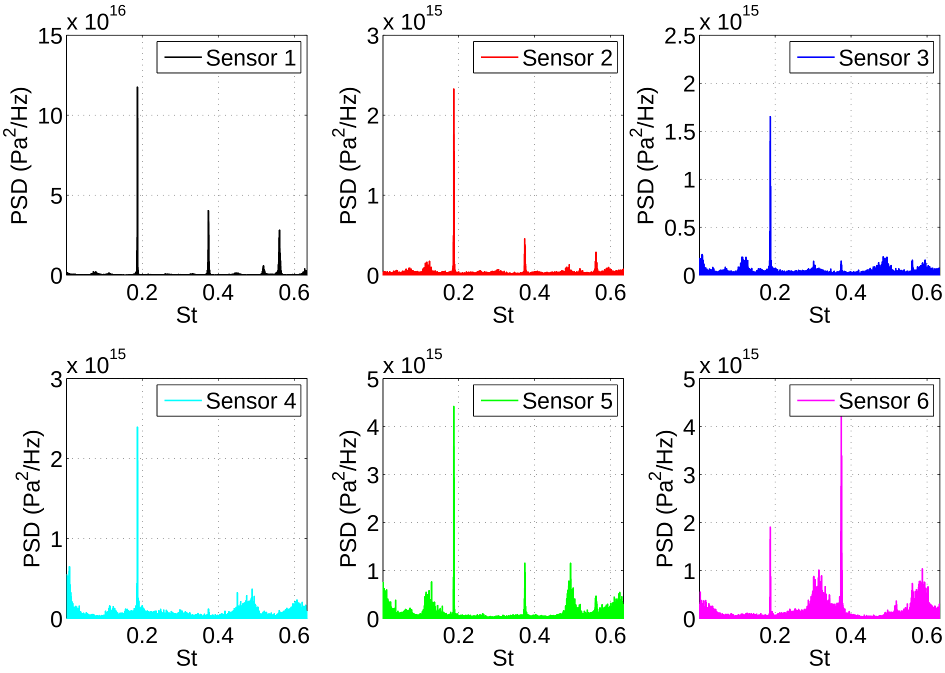

Figure 5.8: Detection of the whistling frequency in sensors 1-6 for flow at 1 m/sec through S1

Flow speed U_p (m/sec)	Hole velocity U_h (m/sec)	Frequency peak f (Hz)	Strouhal number $St = \left(\frac{f \times t}{U_h}\right)$
0.93	18.8	3617	0.19
1	20.2	3782	0.187
1.17	23.7	4506	0.19
1.24	25.1	4814	0.19

Table 5.2: Whistling frequency at different flow speeds and the corresponding Strouhal number based on plate thickness ($t = 1$ mm) and hole velocity U_h

5.4 Multiple-hole orifice plates

A similar analysis is performed on the multi-hole orifice plates listed in section 4.3. The flow conditions and the corresponding pressure losses that were measured can be found in appendix B. The viscous pressure loss over the components of the test setup are subtracted using equation 5.4. The resulting steady pressure loss created by each multi-hole orifice plate as a function of the flow speed, is shown in figure 5.9. Note, the number in parenthesis denotes the number of holes in the plate.

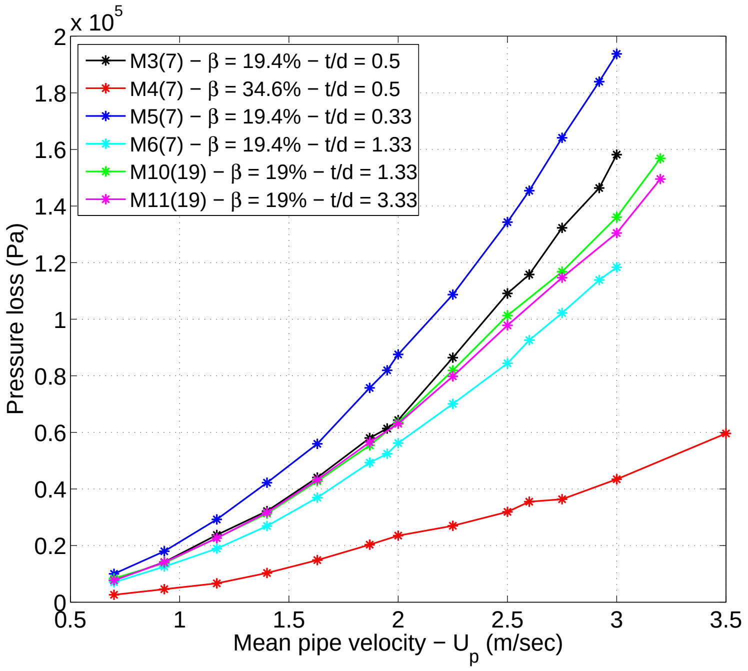

Figure 5.9: Pressure loss as a function of the mean flow speed for all the multi-hole orifices tested. The number in parenthesis denotes the number of holes in the plate.

5.4.1 Effect of Reynolds number on the loss coefficient

The magnitude of the pressure loss is normalized by the mean dynamic-pressure, to get the loss coefficient. Figures 5.10a and 5.10b illustrate the behavior of the loss coefficient as a function of pipe Reynolds-number and hole Reynolds-number respectively.

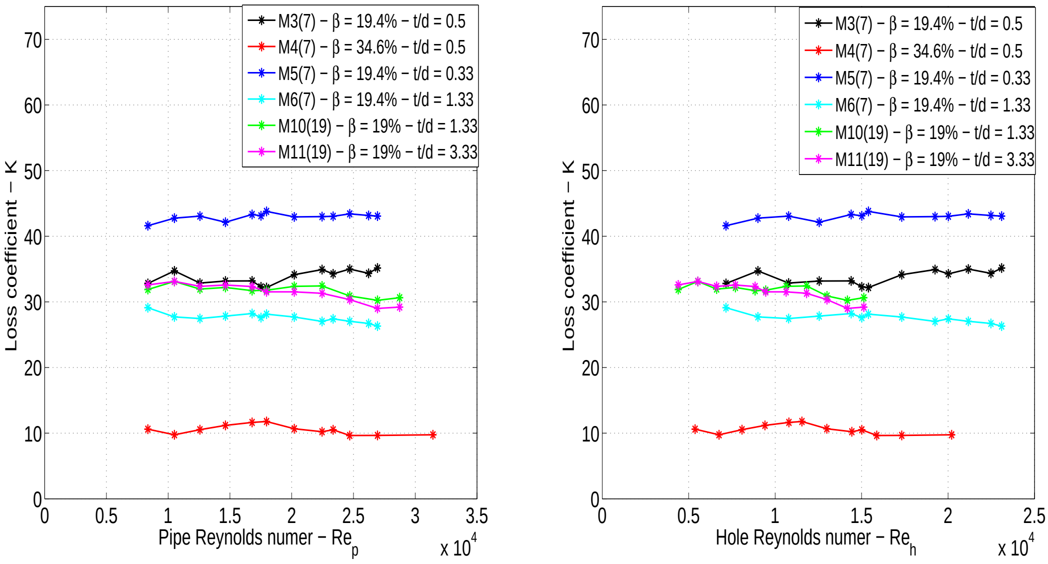

(a) Plot of the loss coefficient as a function of Re_p.**(b)** Plot of the loss coefficient as a function of Re_h.

Figure 5.10: Figures illustrating the loss coefficient behavior of all the multi-hole orifice plates tested.

The results show that the loss coefficient does not present large variations with Reynolds number. Thus, it can be concluded that in the present measurement range, the loss coefficient belongs to the self similar region. This trend is in accordance with results of Kolodzie and Winkle (1957) and Maynes et al. (2013) who report self-similarity for multi-hole orifice plates when $Re_h > 3000$. As a result, the pressure loss is proportional to the square of the flow speed. Table 5.3 outlines the average loss-coefficient values for all the multi-hole orifice plates.

Plate label	No. of holes N_h	Porosity β (%)	Thickness ratio t/d_h	Loss coefficient K
M3	7	19.4	0.5	33
M4	7	34.6	0.5	11
M5	7	19.4	0.33	43
M6	7	19.4	1.33	28
M10	19	19.0	1.33	31
M11	19	19.0	3.33	32

Table 5.3: Average loss-coefficient values in the self-similarity region for the multiple-hole orifices tested.

5.4.2 Effect of geometry on the loss-coefficient

The limited number of orifice plates tested does not allow for a rigorous analysis of the effect of geometrical variables on the behavior of the loss coefficient. However, some general conclusions can be made.

- The plate with the smallest porosity and thickness ratio creates the highest pressure losses. Increase in the porosity or thickness-ratio, leads to a decrease in pressure losses with the former having a greater effect.
- For a given plate porosity and thickness ratio, the number of holes in the plate seems to have a minor effect on the loss-coefficient (compare M6 and M10).
- The similarity in the measured loss coefficient of plates M10 and M11 indicates that the flow has reattached inside the orifice hole. Therefore, an increase in plate thickness has little effect on the loss coefficient.

5.4.3 Wall pressure-fluctuations

Taking a similar approach as described in section 5.3.3 for single-hole orifices, P'_{rms} at each location is computed using equation 5.6 for all the multiple-hole orifices. These values are then normalized by the mean dynamic pressure of the incoming flow.

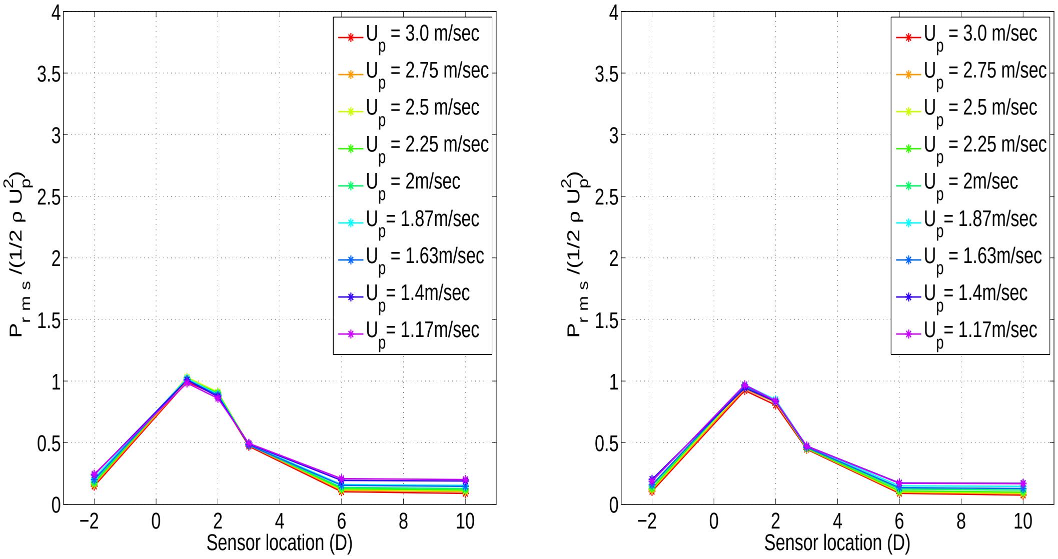

(a) Plate M10 (19), $\beta = 19.4\%$, $t/d_h = 1.33$ **(b)** Plate M11 (19), $\beta = 19.4\%$, $t/d_h = 3.33$

Figure 5.11: Figures illustrating the axial variation of $P'_{rms}/(\frac{1}{2}\rho U_p^2)$ for multiple-hole orifice plates of porosity 19.4% with 19 holes.

Figures 5.12 and 5.11 present the stream-wise variation of P'_{rms} normalized by the dynamic pressure $(\frac{1}{2}\rho U_p^2)$, measured at different axial locations, for different orifices at several flow speeds. The axial distances (x/D) are relative to the orifice position ($x = 0$), with positive values downstream. The following are some observations from the results:

- **Scaling**
  Similar to the single-hole orifices, P'_{rms} scales with the mean dynamic-pressure which leads to a collapse of all the measured values at different flow speeds on top of each other, for a given orifice. Thus, both the pressure loss ΔP, and P'_{rms}, scale with the square of the mean flow-speed and in turn with each other.

- **Pressure fluctuation levels**
  In the range of the flow conditions and orifices tested, $P'_{rms}/(\frac{1}{2}\rho U_p^2)$ attains a maximum at about 1D downstream from the orifice. Interestingly, this appears to be true for a large majority of the orifice plates (as most have $\beta \approx 20\%$). Note, the spatial resolution of this data, which corresponds here to the distance between each sensor, is $1D$, in regions close to the orifice. Thus, it appears that the highest flow fluctuations are present in regions close to the orifice ($x \leq 1D$), for the orifices described here. The normalized R.M.S of the pressure fluctuation levels at 6D downstream appear comparable to the upstream pressure fluctuation levels.

- **Effect of geometry**
  Comparison of figures 5.12a and 5.12b illustrates a large decrease in pressure fluctuation levels for an increase in plate porosity. For a given porosity, downstream pressure fluctuations increase for decreasing t/d_h (compare 5.12d, 5.12a and 5.12c).

  However, comparison of figures 5.11a and 5.11b indicates that after a certain point, a further increase in t/d_h has no effect on the normalized pressure fluctuation levels. Thus, once the flow inside the hole locally reattaches, there is little change in both the pressure loss coefficient and the normalized pressure fluctuation levels.

  The effect of number of holes can be seen in figures 5.12d and 5.11a. For a given porosity and t/d_h, there is a small decrease in the peak pressure fluctuation levels at $1D$ in the plate with 19 holes when compared to the plate with 7 holes. For the same porosity and thickness ratio, the 19 hole plate has perforations of a smaller diameter (0.9 mm) compared to the 7 holes of diameter (1.5 mm).

The trends seen here are compared to the results from PIV measurements on multiple-hole orifices in section 7.4.3 of chapter 7. The next section compares the results from single and multiple-hole orifice plates of similar geometries.

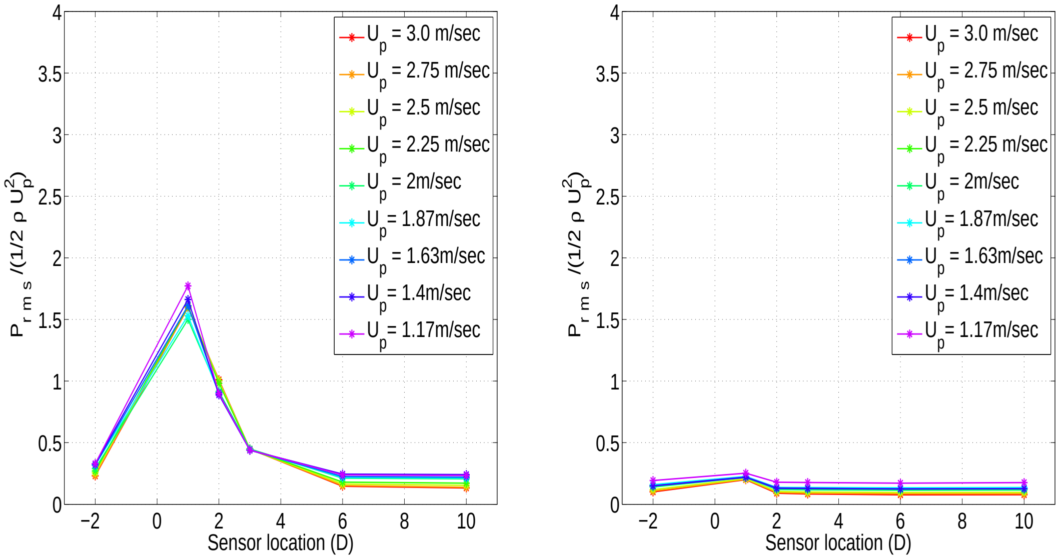

(a) Plate M3 (7), $\beta = 19.4\%$, $t/d_h = 0.5$ **(b)** Plate M4 (7), $\beta = 34.6\%$, $t/d_h = 0.5$

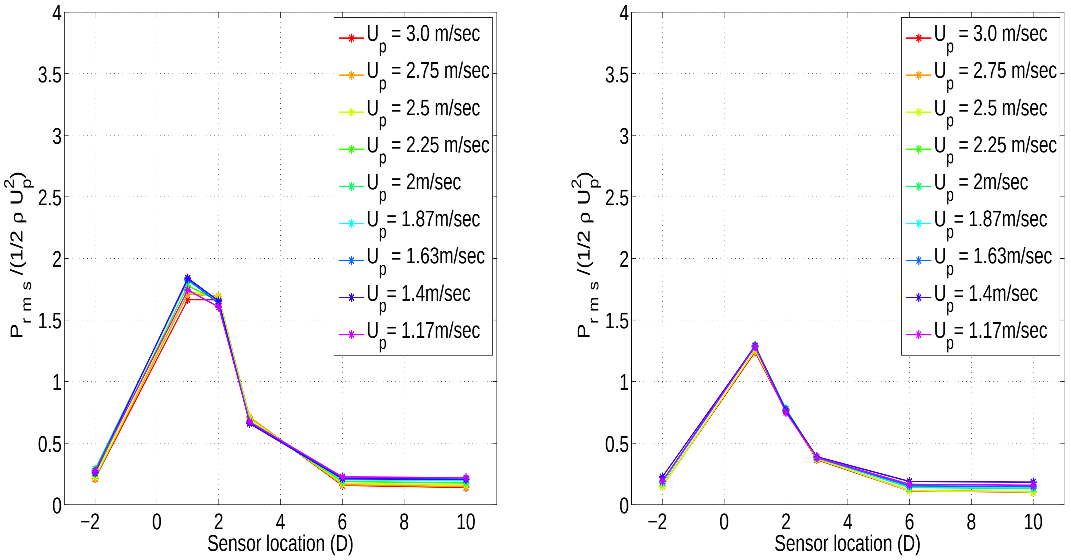

(c) Plate M5 (7), $\beta = 19.4\%$, $t/d_h = 0.33$ **(d)** Plate M6 (7), $\beta = 19.4\%$, $t/d_h = 1.33$

Figure 5.12: Figures illustrating the axial variation of $P'_{rms}/(\frac{1}{2}\rho U_p^2)$ for multiple-hole orifice plates.

5.5 Comparison of single and multiple-hole orifice plates

Figure 5.13 compares single and multiple-hole orifice plates. In order to make this comparison, data from orifice plates having comparable porosity and the same thickness ratio are selected. Thus, S3 can be compared to M3 and S4 to M4.

5.5.1 Pressure losses

It is observed that for a given porosity and thickness ratio, both single and multiple-hole orifices give very similar pressure losses. This can be seen in the curves for the actual pressure loss as a function of the flow speed (figure 5.13a).

The mean loss coefficient values of S3 ($K = 36$) and M3 ($K = 33$) are comparable (figure 5.13b). Note that differences in S4 ($K = 14$) and M4 ($K = 11$) are likely due to the 4.6% difference in their porosities.

Thus, it can be concluded that by scaling both the non-dimensional variables (β and t/d_h), multiple-hole orifices can produce similar pressure-losses compared to single-hole orifice plates. This conclusion is in accordance to the recommendations of Miller (1990).

5.5.2 Pressure fluctuations

In sections 5.3.3 and 5.4.3, it was established that for both single and multiple hole orifices, P'_{rms} scales with the mean dynamic pressure so that the normalized P'_{rms} does not change with the flow speed (in the range of flow conditions tested). As a result, a comparison between single and multi-hole orifices of comparable geometries are made at a single flow-speed of 2 m/sec ($Re_p = 18000$).

Figure 5.13c depicts the axial variation of pressure fluctuations. For the same porosity and thickness-ratio, results of S3 and M3 show that the peak level of the normalized pressure fluctuations at $1D$ are very similar. However, the decay thereafter is much stronger for the multiple-hole orifice plate. The difference in the downstream fluctuation levels between S4 and M4 is rather large. This is partly due to the 4.6% difference in porosity between the plates.

From these comparisons, it is observed that overall, downstream pressure-fluctuation levels are diminished while using multiple-hole orifice plates even though the peak fluctuation levels may be similar (from S3 and M3). The length scales of the fluid issuing from the multiple-hole orifice are smaller than the single-hole orifice. They are thus expected to breakdown and dissipate faster. The interaction between the multiple-jets is expected to further promote mixing and is also a likely cause for the reduced magnitude of downstream pressure fluctuations. These assumptions are verified by the results from velocity measurements described in section 8.2.2.

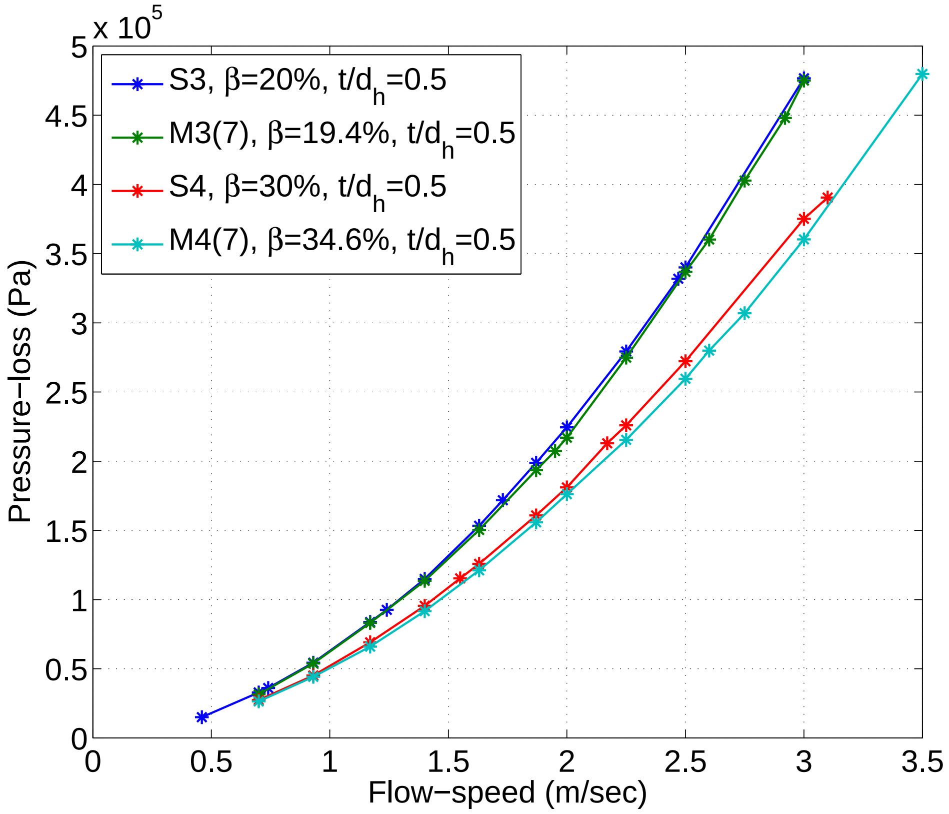

(a) Pressure loss as a function of the flow speed.

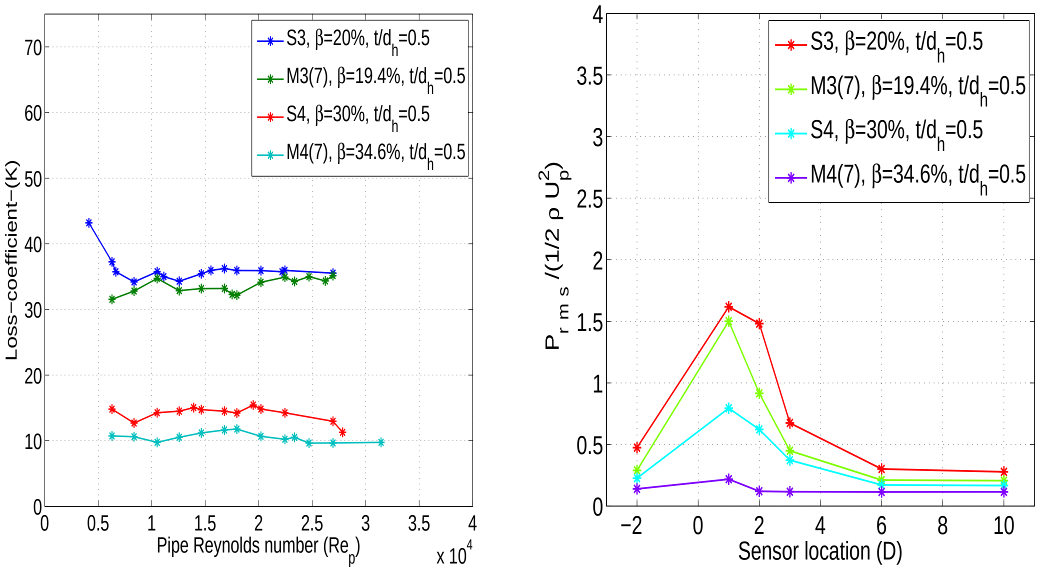

(b) Loss coefficient as a function of Re_p.

(c) Axial variation of $P'_{rms}/(\frac{1}{2}\rho U_p^2)$.

Figure 5.13: Comparison of single(S) and multi-hole(M) orifice plates of similar geometries

5.5.3 Geometric constraints

Results presented in this section have shown that multiple-hole orifices can be used as a replacement to single-hole orifices to achieve the same pressure loss. The pressure fluctuations measured downstream of multi-hole orifices are found to be lower as a result of reduction in size of the flow scales.

To achieve this, both the porosity and thickness to hole diameter ratio need to be taken into account. This means that for a given β and t/d_h, multiple-hole orifice plates (which have many holes of small diameter) will have a lower plate thickness in comparison to its equivalent single-hole orifice. The thickness of the plate also constrains the smallest hole sizes that can be used in a multiple-hole orifice.

In practice, due to manufacturing and/or due to structural rigidity, a plate thickness below 1 mm may not be feasible. This constraint is particularly relevant with respect to the orifice plate geometries that were investigated in the present study.

5.6 Conclusion

This chapter covered results obtained from pressure measurements performed on single and multi-hole orifice plates. The effect of Reynolds number and geometry, on the loss coefficient of single and multiple hole orifices were discussed. The loss-coefficient of majority of the orifices belonged to the self similar region and the effect of geometry on the measured loss coefficients was found to be in agreement to those previously reported in literature.

The loss-coefficient of a cavitating single-hole orifice presented a Reynolds number dependency expected in region-3. The whistling sounds that the orifice emanated was quantified and the non-dimensional whistling frequency ($St \approx 0.02$) matched closely to those described in literature.

The axial variations in pressure fluctuations for both single and multiple-hole orifices were presented. The RMS of the pressure fluctuations were found to scale with the square of the incoming flow speed.

The peak pressure fluctuation levels for the single hole orifices occurred between 1-2D from the orifice, with the location varying as a function of the orifice geometry. For the multiple-hole orifices tested, the peak pressure fluctuations occurred much closer to the orifice ($x \leq 1D$).

A comparison of single and multiple hole orifices showed that for a given β and t/d_h, both presented comparable pressure losses under the present measurement conditions. The overall pressure fluctuation levels downstream of multiple-hole orifices were found to be lower, though the peak pressure fluctuations could be similar. The pressure fluctuations created by multiple hole orifices were observed to decay over a much shorter distance when compared to the single-hole orifice of comparable geometry.

Chapter 6

Approach: Velocity measurements

6.1 Introduction

The working principle and the components of a conventional PIV setup were highlighted in section 2.5. This chapter describes the test setup that was used in the present study to perform time-resolved planar-PIV measurements on the flow downstream of orifices in pipes.

Starting with a working overview of the setup, the subsequent subsections give a detailed description of the experimental apparatus used during the measurements. The geometries of the orifice plates that were investigated are outlined in section 6.3. The experimental considerations along with the flow conditions of interest are presented in section 6.4. A summary of the PIV experimental settings are highlighted in section 6.4.6. The final section (see section 6.5) presents the steps taken to process the measurement data.

6.2 Experimental setup for Particle Image Velocimetry measurements

The layout of the setup was planned so as to adapt to existing infrastructure available at the jet-tomographic-facility (JTF) of the Aerodynamics laboratories at the faculty of Aerospace engineering, TU Delft.

The JTF has been used in the past for tomographic-PIV measurements on circular and chevron-jets (Violato & Scarano, 2011) and aerodynamics of flapping wings (Perçin et al., 2011).

6.2.1 Setup overview

A schematic representation of the experimental setup is shown in figure 6.1. Water containing seeding particles is supplied by a pump. The flow first passes through a flow meter and then to a settling chamber. It subsequently enters an orifice plate under fully-developed and turbulent conditions. The fluid issuing from the orifice passes through a transparent glass tube and eventually exits into the octagonal tank. The entire test section is submerged in water inside the octagonal tank and the flow from the tank is carried back to the reservoir.

The measurement region is formed by the two-dimensional central longitudinal plane of the glass pipe following the orifice plate. The particles moving in this plane are illuminated by a light sheet produced by a high-speed laser. To extend the measurement region in the stream-wise direction, two high-speed cameras are used, which are positioned on opposite sides of the glass tank, with a viewing direction orthogonal to both the tank wall and the laser-light sheet. The triggering of the laser illumination and image acquisition by the cameras are synchronised by a high-speed controller.

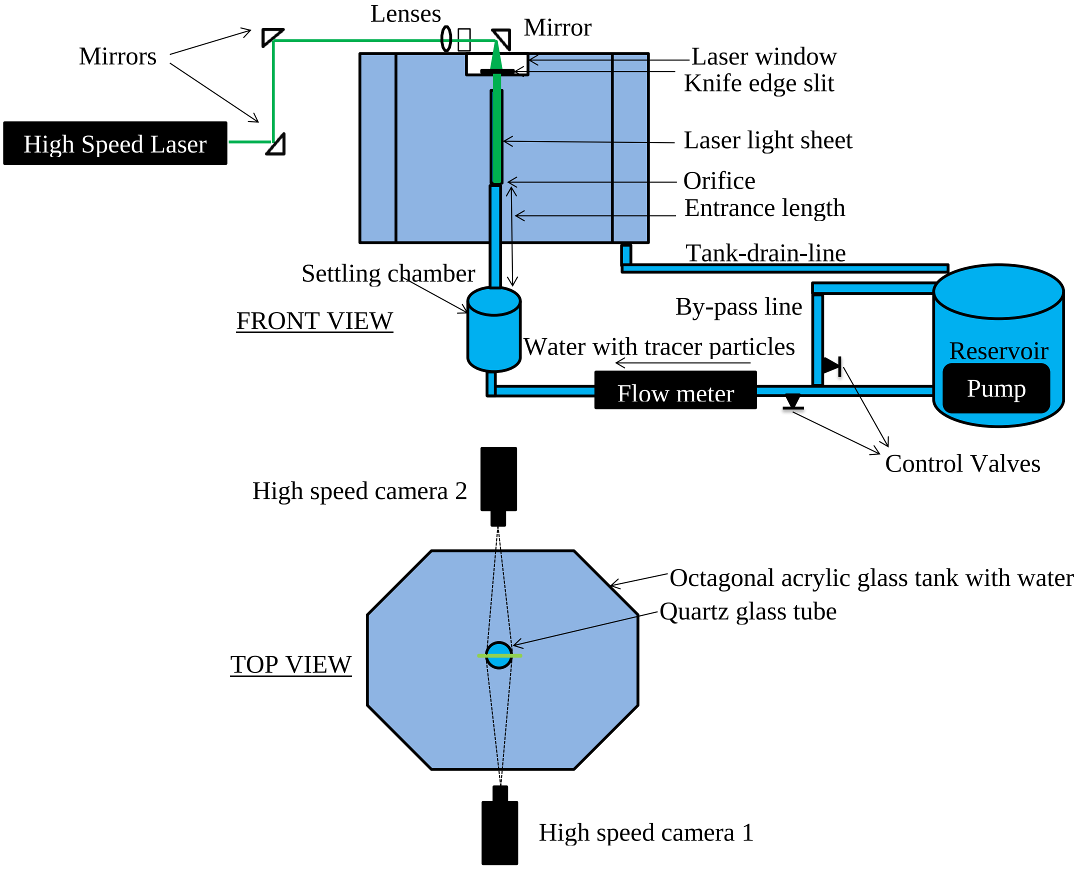

Figure 6.1: Schematic of the experimental setup used to perform time-resolved planar particle image velocimetry (PIV)

6.2.2 Experimental instrumentation and arrangements

- **Pump, control valves and connecting hoses**
  An Oase Aquarius Universal 40000 pump (see figure 6.2a) drives the flow through the experimental setup. It is submerged inside a reservoir containing water mixed with seeding particles. The pump is connected to an external electronic-flow-control unit, that controls its flow rate. Since, the maximum head-height deliverable by the pump is 11 m, the largest allowable pressure drop over the entire setup is 1.07 bar (107.91 kPa). This value restricts the maximum attainable flow speed for a given orifice within this setup.

Property	Value
Dimensions	$461 \times 234 \times 293$ mm
Net weight	19.68 kg
Maximum flow-rate	40000 l/hr
Maximum head height	11 m

Table 6.1: Specifications of the Oase Aquarius Universal 40000 pump as reported by the manufacturer.

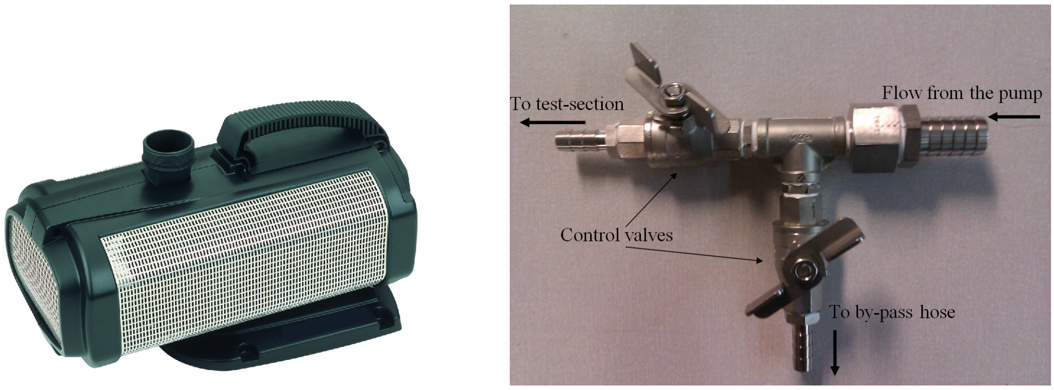

(a) (b)

Figure 6.2: Oase Aquarius Universal 40000 fountain pump (left) and the T-junction with control valves used to set the flow speed within the test section (right).

Water from the pump is carried to a T-junction (see figure 6.2b) by a hose of internal diameter 24 mm and wall-thickness 4 mm. Here, the flow splits into two. A part of the flow is channeled to the flow meter and subsequently into the test section. The remaining portion is carried back to the reservoir by the by-pass hose. Both hoses have an internal diameter of 12 mm and a wall-thickness of 8 mm. The ball valves provided on the T-junction and the pump electronic-flow-control unit are used together to set the flow speed.

- **Flow meter**
  The flow from the T-junction passes through a mechanical flow-meter (see figure 6.3a) to set the flow speed. The flow meter has a suspended mass whose weight

opposes the force exerted by the flowing liquid. The position of the suspended mass is indicated on a percentage scale varying from $0 - 100\%$, with 100% corresponding to the highest flow rate that the flow meter can measure. The flow meter was calibrated and the linear relation between the flow speed and the markings etched on the flow meter are shown in figure 6.3b.

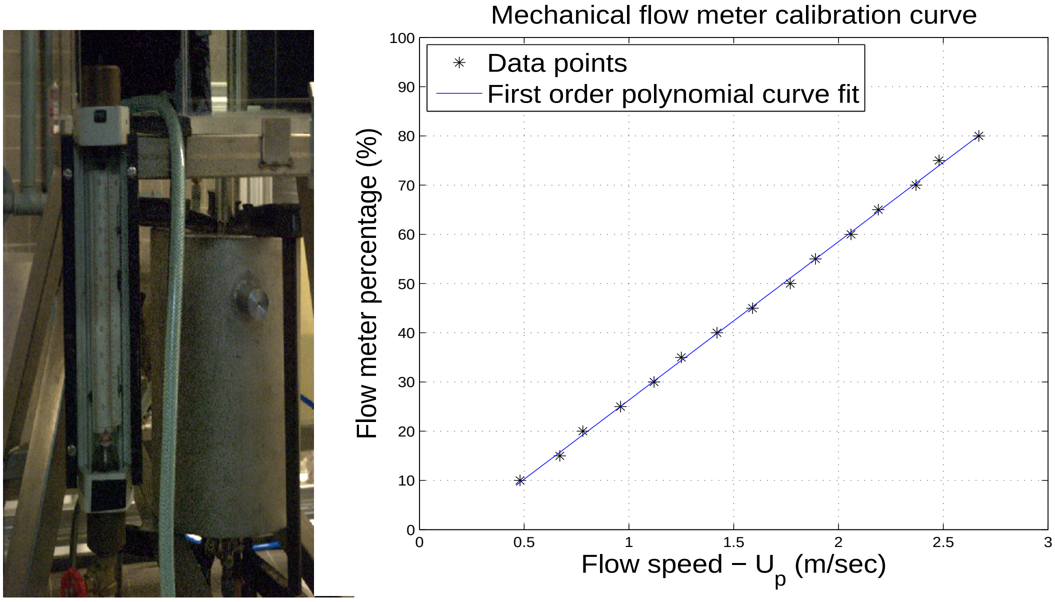

(a) Flow meter **(b)** Calibration curve

Figure 6.3: Flow meter and its calibration curve

- **Settling chamber**
  Before entering the test section, the water is carried to a settling chamber. It is a closed cylindrical tank of diameter 300 *mm* and height 400 *mm*. Its lower end is provided with a hose pillar to connect the hose pipe arriving from the flow meter. The upper end of the settling chamber opens into a stainless-steel pipe section meant to provide the necessary entrance length for the flow to reach fully-developed conditions.

- **Octagonal tank**
  An octagonal shaped tank made of acrylic glass surrounds the glass tube. The tank width and height span 600 *mm* and 800 *mm* respectively. The acrylic glass walls enable extensive optical access for illumination and imaging which are crucial requirements for PIV investigations.

  The floor of the tank has an opening in its center for the stainless-steel pipe connected to the settling chamber. It also contains an outlet to drain the fluid inside the tank. The roof of the tank is equipped with a laser-window that descends into the tank such that the window is submerged in water when the tank is filled.

- **Test section**
  A cylindrical stainless-steel pipe of inner diameter 8.4 *mm* and length 400 *mm* carries water from the settling chamber. It ensures that the flow enters the orifice

plate under fully developed conditions (see equation 4.1). Figure 6.4 shows the positioning of an orifice plate at the exit of the steel pipe.

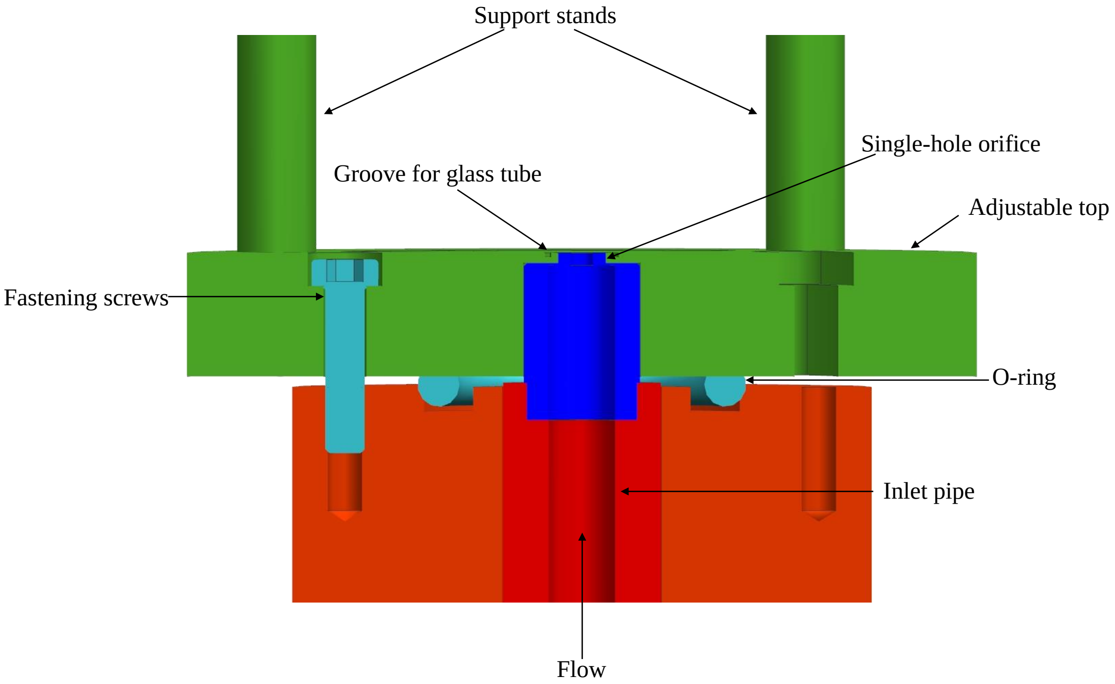

Figure 6.4: Cross-sectional view of the test setup showing the position of the orifice with respect to the upstream stainless steel pipe. The glass tube (not shown here) is fixed in the groove provided using an adhesive. ***Design courtesy ASML.***

The flow emerging from the orifice is observed in a glass tube of internal diameter 8.4 mm and wall thickness 0.3 mm ($t/D = 3.5\%$). The specifications of the glass tube are outlined in table 6.2. For measurements in geometries with curved inner and outer surfaces, the difference in refractive index of the glass wall and water leads to an error in particle positions recorded on the camera due to refraction at the glass-water interface. To minimize this, pipe geometries with extremely thin walls are employed (van Doorne & Westerweel, 2007; Westerweel et al., 1996). This ensures that refraction errors due to wall curvature are confined to regions very close to the boundary of the glass. Section A.1 in appendix A discusses this as a source of measurement error in further detail.

The glass tube is fixed into a groove provided on a support structure (see figure 6.5) using an adhesive. The pillars of the support ensure structural stability and protect the fragile glass. The entire support structure is painted black to minimize background reflections. It is free to rotate about its longitudinal axis, which enable its positioning to be such that the pillars do not block the camera field-of-view. Once a suitable position is determined, the support structure is fixed to the inlet pipe using fastening screws.

Property	Value
Material	Fused Quartz-Silica glass
Inner diameter	8.4 mm
Wall thickness	0.3 mm
Length	150 mm
Refractive index	1.46
Density	2200 kg/m^3
Design tensile strength	48 MPa
Design compressive strength	1100 MPa
Young's modulus	72 GPa

Table 6.2: Specifications of the quartz glass tube used in the PIV experiments.

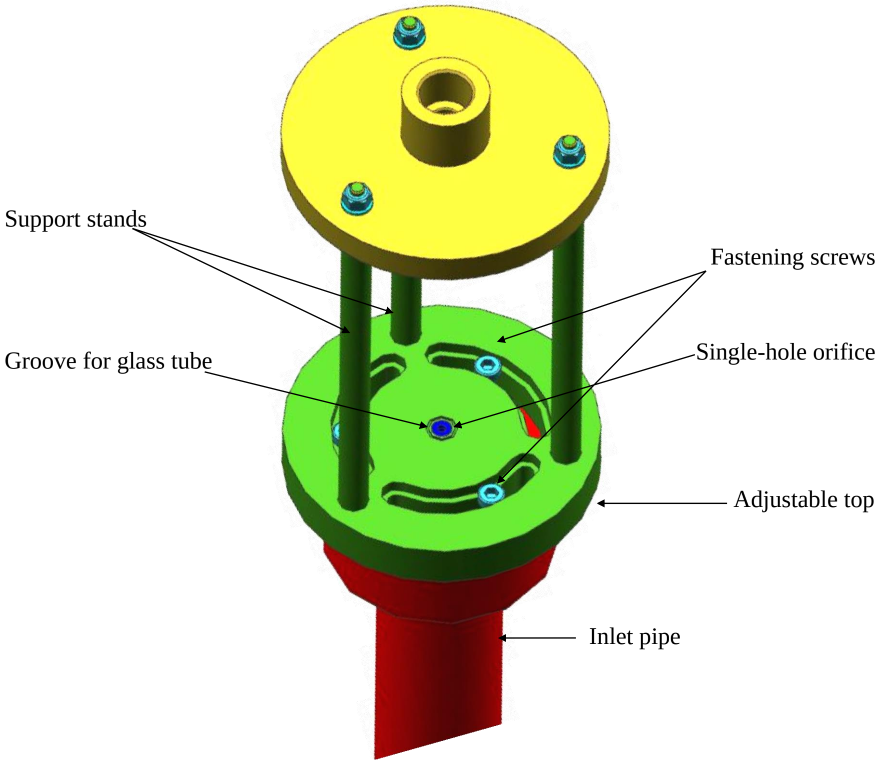

Figure 6.5: Isometric view of the support structure fixed to the inlet steel pipe as seen from the exit side. Note, the image does not show the glass tube. ***Design courtesy ASML.***

- **Flow seeding**
  Silver-coated, hollow glass sphere particles of mean diameter 10 μm are used for seeding the flow. They have sufficiently small velocity lag and show very good scattering properties (Raffel et al., 2007). Furthermore, these particles remain suspended in the flow for several hours. Table 6.3 summarizes the properties of these tracer particles. The required quantity are weighed and added directly to the reservoir in suspension form where they are mixed thoroughly.

Property	Value
Material	Borosilicate glass coated with silver
Mean diameter	10 μm
Size distribution	$2 - 20$ μm
Particle shape	Spherical
Density	1400 kg/m^3
Refractive index	> 1.52

Table 6.3: Specifications of Silver coated hollow glass sphere tracer particles used for PIV measurements.

- **Illumination source**
  A neodymium-doped yttrium lithium fluoride (Nd:YLF) diode pumped, dual cavity, high-speed laser is used for illumination during PIV measurements. Table 6.4 summarizes the properties of the laser used.

Property	Value
Manufacturer	Litron
Laser medium	Nd:YLF
Output wavelength	527 nm
Repetition rate	$0.2 - 20$ kHz
Pulse energy (at 1kHz)	22.5 mJ/pulse
Beam diameter at exit	5 mm

Table 6.4: Specifications of the high-speed laser used for illumination.

To illuminate the measurement plane, the light beam from the source is reflected and shaped using mirrors and lenses respectively. The light enters the glass pipe from the top through the laser window of the octagonal tank. Knife edges are placed inside the laser window to shape the light sheet. This helps in further decreasing the the light sheet thickness to 0.5 mm.

- **Imaging**
  Two high-speed cameras (High Speed Star 6) are used for recording images. These are high sensitivity, mega-pixel resolution digital cameras used for time-resolved PIV measurements. The camera has an advanced CMOS sensor that allows frame rates up to 5400 Hz at full resolution of 1024×1024 pixels and 20 kHz at a reduced area of 512×512 pixels. Table 6.5 summarizes its properties.

- **Synchronizer and Software**
  The camera frame rate and laser light pulses are triggered and synchronized using LaVision's high speed controller. DaVis 8.1.6 software by LaVision, integrates all the PIV recording operations and is used for acquiring images during measurements.

Property	Value
Full resolution	1024×1024 pixels
Frame rate	5.4 kHz at full resolution
Pixel pitch	20 μm
Minimum exposure time	1 μs
Minimum inter frame time	< 1 μs

Table 6.5: Specifications of the High Speed Star 6 cameras used for recording.

6.3 Orifice geometries

This section outlines the geometries of the orifice plates investigated during PIV measurements.

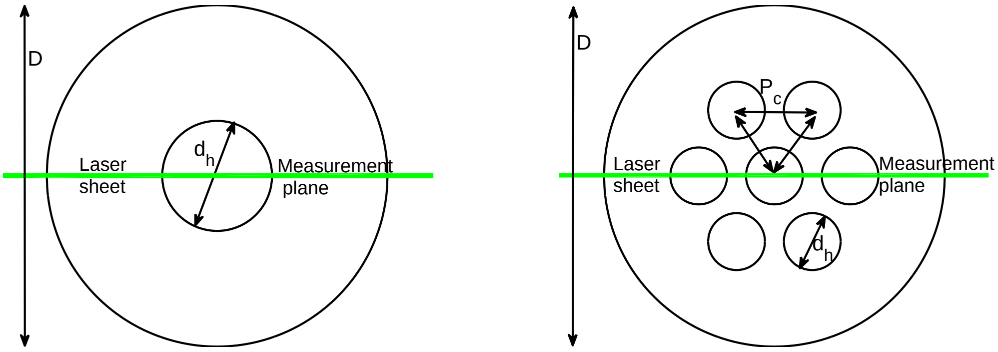

(a) Single-hole orifice plate **(b)** 7-hole multi-hole orifice plate

Figure 6.6: Figures illustrating the orifice geometric variables and the top view of the PIV measurement plane.

Single-hole orifices

Table 6.6 specifies the geometries of the single-hole orifices. Majority of the orifices used have properties analogous to those described in table 4.4 for the pressure measurements. Due to a minor difference in the internal diameter of the two test-setups[1], the hole diameter and thickness were modified so as to reach the same non dimensional values (compare S3 and PIV-S3).

Some constraints in the PIV test setup did not allow for all the orifices used in pressure measurements to be reproduced for PIV measurements. For example, to achieve a t/d_h of 0.125 as in S6, a plate thickness smaller than 0.5 mm would be necessary, which was not feasible. Furthermore, an orifice with a porosity of 5% (S1) creates such large pressure losses, that the pump used in the PIV setup isn't powerful enough to drive the flow.

---

[1] The test section used in pressure measurements has an inner diameter of 9 mm whereas the entrance pipe and the glass tube used in PIV measurements has an internal diameter of 8.4 mm.

Plate label	Hole diameter $d_h(mm)$	Plate thickness $t(mm)$	Porosity β (%)	Thickness-ratio t/d_h
PIV-S2	2.8	1.5	11	0.5
PIV-S3	3.8	2.0	20	0.5
PIV-S4	4.6	2.5	30	0.5
PIV-S5	6.5	3.5	60	0.5
PIV-S10	3.8	3.0	20	0.8
PIV-S11	3.8	4.0	20	1.05

Table 6.6: Geometries of the single-hole orifice plates used for PIV measurements

Multi-hole orifice

Table 6.7 specifies the geometry of the multi-hole orifice plate that was tested in the PIV investigations. Given the complex and three-dimensional nature of the flow features expected to emerge from the orifice (7-jets), it was decided to confine the planar PIV measurements to a single plate.

Plate label	N_h	$d_h(mm)$	$t(mm)$	P_c (mm)	P/d_h	β (%)	t/d_h
PIV-M1	7	1.4	1.5	2.8	2	20	1.07

Table 6.7: Geometry of the multiple-hole orifice plate used for PIV-measurements

6.4 Experimentation

The measurement instruments and their specifications were presented in section 6.2.2. This section presents the final experimental settings used during PIV measurements. A summary of the experimental parameters are presented in table 6.10.

6.4.1 Illumination

This section describes some experimental considerations that were taken into account for illumination of the measurement plane using the high speed laser. Figure 6.7 illustrates the two different illumination approaches that were evaluated. For clarity, not all components of the setup are shown.

In the first case, a divergent light sheet passing orthogonal to the octagonal glass tank enters the glass tube from the side and illuminates the central, longitudinal measurement plane (see figure 6.7). Knife edges at the entrance of the octagonal tank limits the light sheet thickness to 0.5 mm. In this configuration, flow from the glass tube is channeled directly into the pump reservoir so that the water in the octagonal tank is free from any tracer particles. The corresponding camera image shows strong reflections from the glass tube that mask a major portion of the flow field. These reflections (caused perhaps due to internal reflections by the two component glass) severely hamper the quality of the images recorded. Image processing (non linear time filtering) reduces some of the aberrations, however, a large majority of the particles are also lost in this process.

To abstain from passing through the glass tube, the laser light is introduced into the measurement plane from the top, through the laser-window used in previous experiments of Violato and Scarano (2011). The laser light is reflected twice before it passes through a spherical and cylindrical lens. It is subsequently reflected the third time and directed into the glass tube (see figure 6.7). Knife edges are placed inside the laser-window that limit the light sheet thickness to 0.5 mm. The dramatic change in the quality of images when illuminating the measurement plane from the top can be seen clearly in the corresponding camera image. Despite the reduction in light intensity due to three reflections, the silver coated particles appear distinctly in the recorded images. However, as the seeded flow from the glass pipe now drains into the octagonal tank, the camera visibility deteriorates with time (see bottom image in figure 6.7).

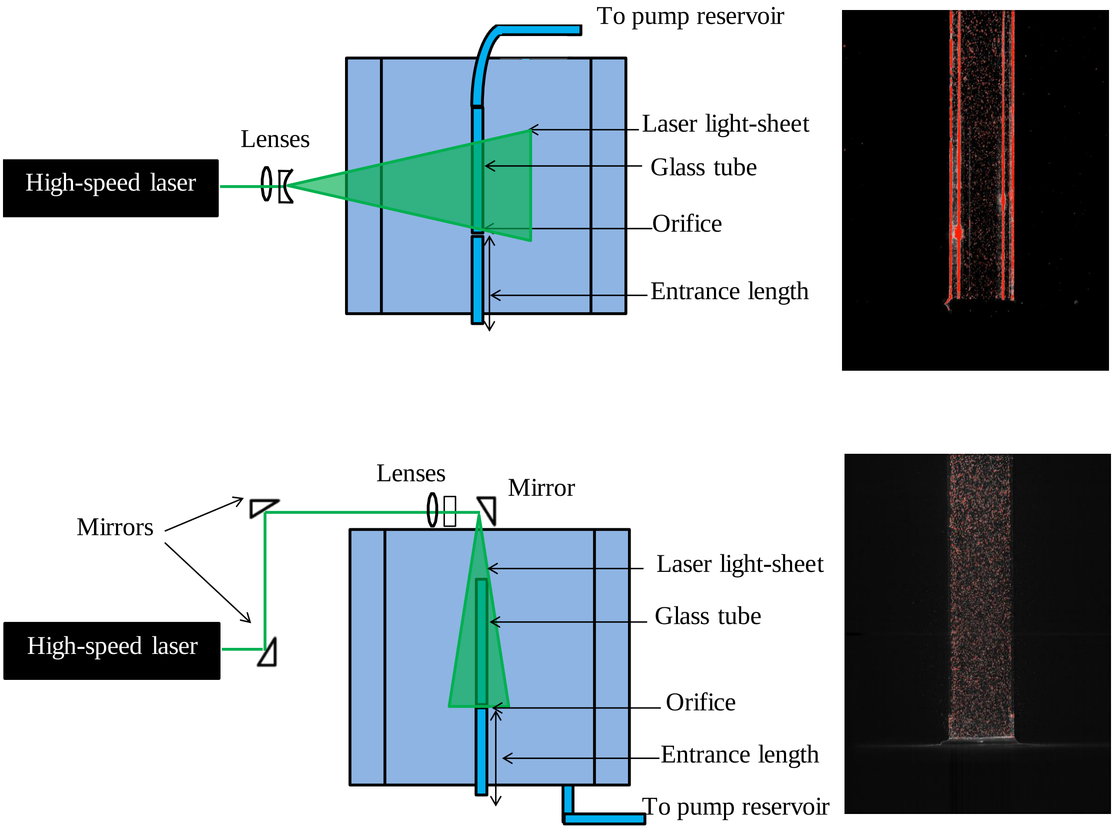

Figure 6.7: Schematic of the laser light configuration and the corresponding raw-image recorded using horizontal illumination (top); vertical illumination (bottom) of the measurement plane.

As a result of the improved image conditions, the second configuration was implemented in all the measurements, as illustrated in the schematic of the test setup presented earlier in figure 6.1. The laser is operated at 65 % of its maximum operating power.

6.4.2 Imaging

High-speed cameras record particle displacements. In order to capture a large extent of the flow field, two cameras are used. These are positioned on opposite sides of the glass tank with a viewing direction orthogonal to the tank wall and the laser light sheet, such that they capture particle motion in the central longitudinal plane of the glass pipe. These cameras are relatively large in size which doesn't allow them to be positioned on top of each other.

Optical arrangement
The cameras are equipped with lenses of focal length $f = 180\ mm$ to achieve a large magnification. Given the large focal length of the lens, extension rings (36, 20 and 12 mm) were required to get closer to the glass pipe and reduce the minimum focusing distance. The $f_{\#}$ is set to 5.6 which ensures that the images are sufficiently bright and the depth of field is large enough for the particles inside the laser sheet to be in focus.

Field of view
Figure 6.8 illustrates the camera field-of-view (FOV). Images from the first camera capture the axial flow field till a distance of about $3.9D$ from the orifice. A small portion ($\approx 0.6D$) of the region preceding the glass tube is also recorded and is eventually masked. The second camera records the flow field from $2.9D$ to $7.4D$, thus creating an overlap region of about $1D$. In order to save memory, the camera resolution is reduced to 384×1024 pixels as the desired measurement plane dimensions are $1D \times 4.5D$. This increases the maximum attainable camera frame rate to 12500 Hz.

Calibration
The glass tube has an internal diameter of 8.4 mm which prohibits conventional calibration plates to be placed inside. A 3D-printed, rectangular shaped calibration plate made of strong and flexible plastic was manufactured. The plate covered with discernible markings that are spaced 2 mm vertically and 0.2 mm horizontally fits into the central plane of the glass tube. This plate can be seen in figure 6.8 with the markings more apparent in the image of camera-2. With water inside the entire test setup, calibration images are recorded that are used for scaling the measured pixel displacements.

6.4.3 Flow seeding

Silver-coated, hollow glass spheres particles are used for tracing the flow. 2 g of particles are mixed with the water in the pump reservoir. This leads to an approximate concentration of about 15 particles/mm^3. The above concentration ensures that sufficient number of particles are present in an interrogation window of 32×32 pixels during post-processing.

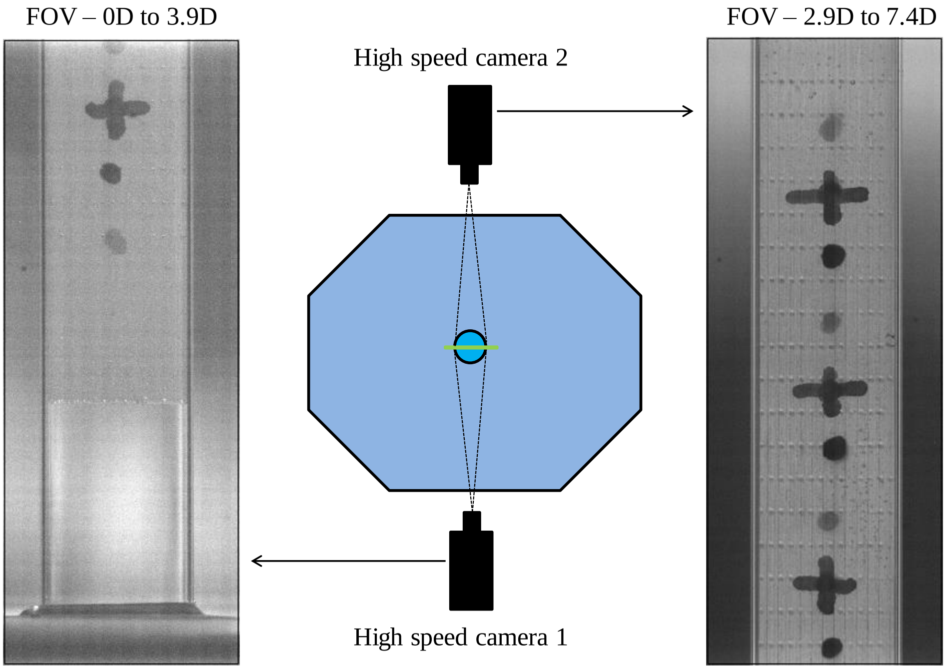

Figure 6.8: Field-of-view of the two high-speed cameras and the calibration plate inside the glass tube. The 3D printed calibration plate placed inside the glass tube has markings spaced at 2 mm vertically and 0.2 mm horizontally.

6.4.4 Flow conditions

Turbulent flow of water at 22°C enters the orifice under fully developed conditions. The mean flow in the pipe is varied between $0.5 - 2$ m/sec which corresponds to a Re_p between 4000 – 17000 at the inlet of the orifice. The increment in the mean flow speed is 0.25 m/sec and is set such that the Re_p values corresponding to those specified in table 6.8[2] are reached.

To facilitate comparison between the orifice plates, a few additional cases are tested such that the hole Reynolds number in the orifice has values tabulated in table 6.9. A complete overview of the flow conditions used for each orifice plate during measurements are outlined in appendix C.

---

[2] Note that the flow-conditions used here are analogous to those used in pressure-measurements described in section 4.4.2.

Serial number	U_p (m/sec)	Re_p
1	0.5	4100
2	0.75	6300
3	1.0	8350
4	1.25	10500
5	1.50	12500
6	1.75	14600
7	2.0	16800

Table 6.8: Flow speed and the corresponding pipe Reynolds number (Re_p) of the flow conditions used during PIV measurements

Serial number	Re_h
1	12500
2	25000
3	18500
4	25000

Table 6.9: Selected hole Reynolds number (Re_h) for additional test cases used during PIV-measurements

6.4.5 Image acquisition

An important parameter that needs to be specified during image acquisition is the time separation Δt between exposures. This parameter is chosen in such a way that majority of particles are imaged in the same interrogation window in both exposures. As a rule of thumb, it is recommended that the maximum in-plane displacement between exposures be less than one-fourth of the correlation window size. Using the velocity in the hole (U_h) as an estimate of the maximum expected flow speed; for a given camera magnification (M) and pixel-pitch, the pulse separation time can be expressed as,

$$\Delta t = \frac{(Pixelpitch) \times (WindowSize)}{4 \times M \times U_h} \tag{6.1}$$

Where, the interrogation window size is assumed to be 32 × 32 pixels. The time separation used during each measurement can be found in the testing matrices provided in appendix C.

The time-separation between consecutive image pairs is set by the image acquisition frequency or the sampling frequency (f_s). This parameter controls the maximum resolvable frequency or the Nyquist frequency which is half of the sampling rate.

Time resolved measurements are performed in two operation modes. They are:

Single frame, time-series mode (SF)

In this mode, both laser pulses are fired in quick succession ($1\mu s$) during each camera frame. The camera frame rate is equal to the sampling frequency f_s. A pair of consecutive images are then cross correlated to obtain the flow field. This requires the camera acquisition frequency to be high enough such that a large majority of particles are imaged in the same interrogation window in both exposures. This condition can only be satisfied for low flow speeds and therefore is restricted to a few test cases. Figure 6.9 illustrates the camera and laser timing diagram. While operating in this mode, the sampling frequency, $f_s = 1/\Delta t$ and is computed using equation 6.1.

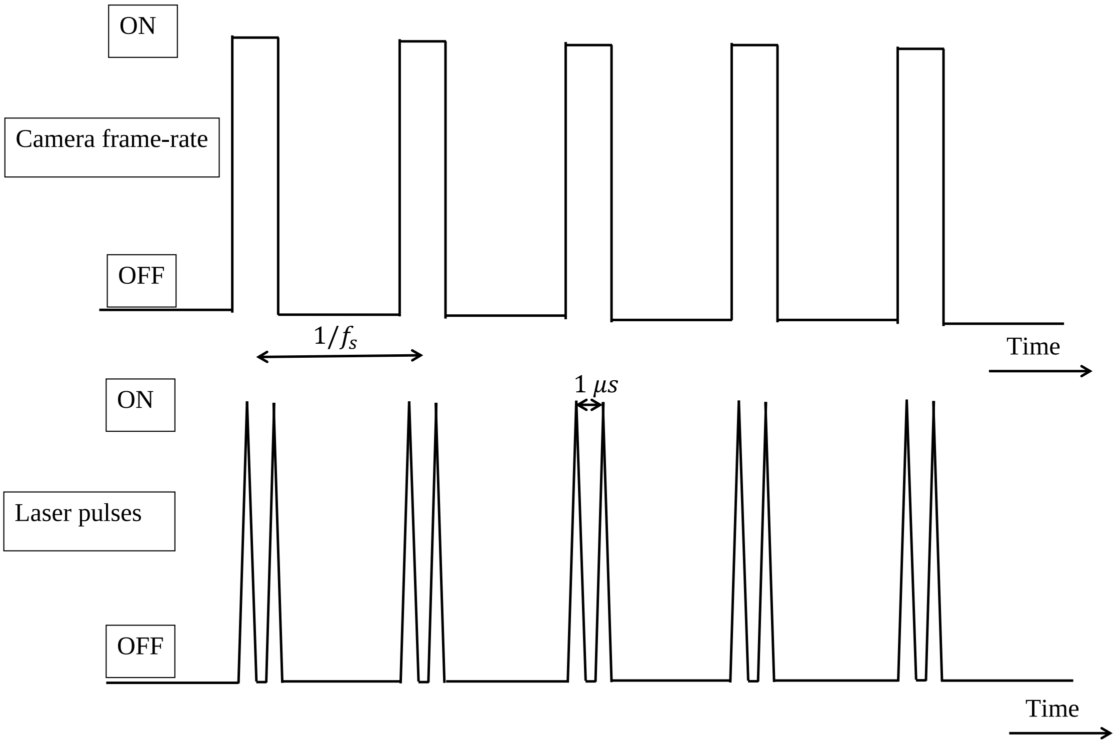

Figure 6.9: Timing diagram illustrating image recording using single-frame time-series images

Double-frame, frame-straddling mode (DF)

In this mode, pairs of images are recorded with the first laser pulse fired towards the end of the first frame and the second laser pulse fired at the beginning of the second frame, as shown in figure 6.10. This allows the selection of an optimum pulse separation time, Δt without it being coupled to the camera acquisition frequency. While recording in this mode, the sampling frequency is fixed to 1500 Hz and the pulse separation time is determined using equation 6.1.

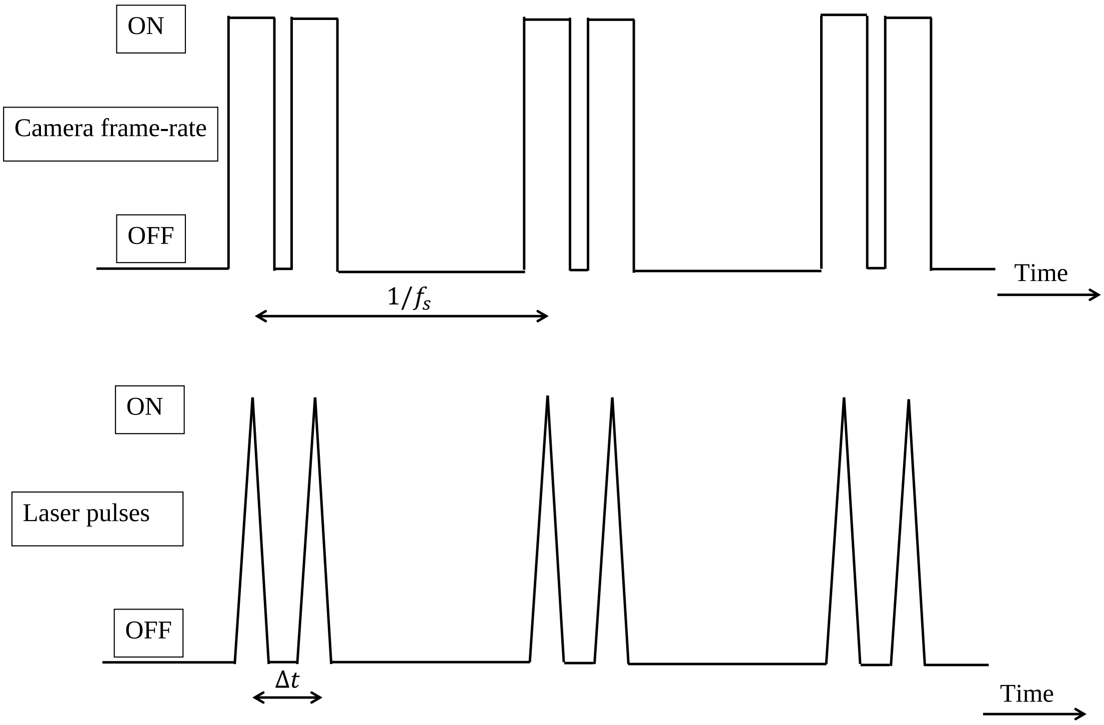

Figure 6.10: Timing diagram illustrating image recording using double-frame images in frame-straddling mode

6.4.6 Summary of experimental settings and testing procedure

Table 6.10 summarizes the experimental settings of the PIV measurements. The following are the typical steps that are taken for each orifice plate PIV measurement.

1. The orifice to be tested is positioned within the setup and the octagonal tank is filled up with clean water. The alignment of the laser light sheet and the cameras are checked.

2. The calibration plate is introduced inside the glass pipe and calibration images are recorded.

3. Tracer particles are weighed and added in suspension form to the pump reservoir. The pump is turned on and sufficient time is allowed for the particles to mix thoroughly. This also allows the air bubbles to escape from the system.

4. Before recording, the laser is set to continuous operation mode and the cameras are made to focus on the tracer particles inside the laser light sheet.

5. The required flow speed is set using the pump electronic flow control and the control valves. The recording mode (single or double frame) time separation, number of images to be recorded and the acquisition frequency is specified and images are subsequently recorded through DaVis.
6. A few images are processed immediately to check for possible abnormalities. Once approved, the images are stored and the next flow-condition is set.
7. The total measurement time at each flow condition is about 8 minutes which is largely due to the time taken for data transfer from the camera to the computer.

Seeding	Silver coated hollow glass spheres Mean diameter: 10 μm Concentration: 15 particles/mm^3
Illumination	Litron laser Maximum repetition rate: 20kHz Sheet thickness: 0.5 mm
Recording device	High-speed star 6 (Two) Minimum exposure time: 1 μs Maximum repetition rate of 5.4 kHz at 1024×1024 pixels Maximum repetition rate of 12.5 kHz at 384×1024 pixels Pixel pitch: 20 μm
Optical arrangement	Nikon lenses: f = 180 mm Extension rings: 36, 20 and 12 mm $f_{\#} = 5.6$
Complete image size[1]	Camera-1 = 37 × 37 mm^2 at 27.7 mm/px Camera-2 = 37.8 × 37.8 mm^2 at 27.08 mm/px
Measurement Field of View[2]	Camera-1 = 8.4 × 32.6 mm^2 or $1D \times 3.9D$ Camera-2 = 8.4 × 37.8 mm^2 or $1D \times 4.5D$ Overlap region = $2.9D - 3.9D$ Complete flow field = 8.4 × 62 mm^2 or $1D \times 7.4D$
Acquisition frequency	Double frame at 1.5 kHz Single frame at 12.5 kHz Pulse separation Δt using equation 6.1
Number of images	Double frame: 3000 images in 2 s Single frame: 6000 images in 480 ms

Table 6.10: Summary of experimental settings for planar PIV measurements

---

[1] Dimensions of the entire recorded image, including regions lying outside the glass tube.

[2] Dimensions of the flow-field inside the glass tube, measured from the orifice exit.

6.5 Data processing

Each measurement comprises of a series of images that need to be processed to construct the two-dimensional vector field. This section describes the steps taken to generate these vector fields using the recorded particle images on DaVis 8.1.6.

6.5.1 Image pre-processing

Masking and Intensity correction
Information lying outside the glass pipe recorded on the images is unwanted and can interfere with the cross correlation of particle images. As a result, these regions are masked which ensures that the pixels lying here are not included in the cross correlation.

In the next step, the intensity of the particles are normalized with respect to the first frame and Gaussian smoothing over 3 × 3 pixels is applied. This reduces image noise and has a positive effect on vector calculations. The effect of intensity correction and Gaussian smoothing can be seen in figure 6.12.

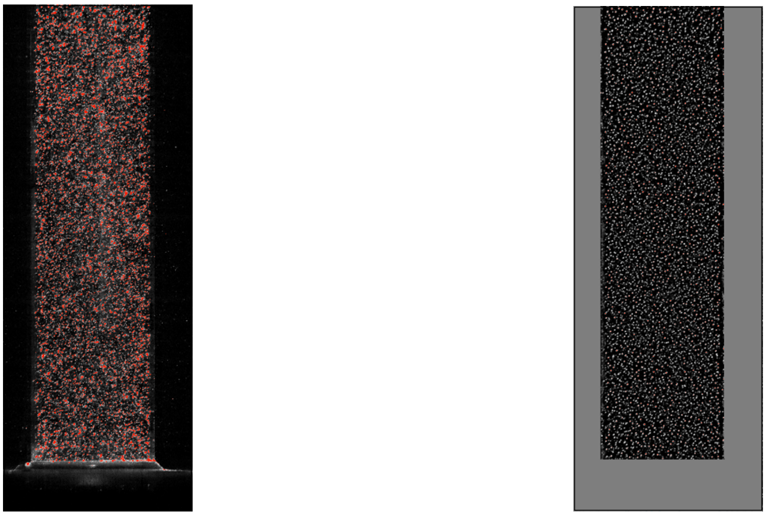

Figure 6.11: Raw-image from camera-1 (left); after masking and image pre-processing (right) as seen on *DaVis 8.1.6*

6.5.2 Vector calculations

Cross correlation
Cross-correlation analysis is performed with multiple passes of decreasing interrogation window sizes. The first two passes are with interrogation windows of size 128 × 128 pixels with an overlap of 50% between neighbouring windows. Starting with large interrogation windows ensures that sufficient number of particle pairs are present to compute particle displacements. The information from the larger windows can then be used as a pre-shift allowing the use of smaller interrogation windows which result in a higher spatial resolution. Therefore, two additional passes with interrogation windows of size 32 × 32

pixels and an overlap of 75% between neighbouring windows are used. This results in a two dimensional, instantaneous vector field shown in figure 6.12a.

Note, before cross correlation the interrogation windows used are multiplied by an elliptical weighting function elongated in the direction of the flow. The downstream flow field is characterized by large velocity gradients normal to the direction of the flow, specially near the shear layer of the jet. Reducing the window size in the direction of the maximum gradient decreases the particle image velocity difference across the window and enhances the correlation signal over highly sheared regions (Scarano, 2003).

Sliding sum-of-correlation
The high sampling rate used during the single frame image acquisitions (12500 Hz) lead to highly correlated image pairs. Such a high temporal resolution allows the usage of advanced vector calculation techniques.

In the present case, the sliding sum of correlation method is used in a few cases. In this method, the average correlation function for each interrogation window is evaluated from a kernel of N image pairs that are separated by the time separation. For an unsteady flow, a small kernel of images, such that the time interval between the first and last snapshot is shorter than the characteristic time scale of the flow must be used (Sciacchitano et al., 2012). The averaging leads to a decrease in the background noise and thus reduces random errors. This approach is viable when the sampling rate is in excess of that strictly needed for temporally resolving the flow (Scarano et al., 2010).

In the present case, three images before and after a given image (±3) are used while implementing this method on DaVis 8.1.6. The first two passes are with interrogation windows of size 64 × 64 pixels with an overlap of 50%. The final passes are with interrogation windows of size 24 × 24 pixels and an overlap of 75% between neighbouring rectangular shaped interrogation windows.

Vector fields and post processing
The spurious vectors that are present after cross correlation are detected and replaced using the universal-outlier-detection algorithm (Westerweel & Scarano, 2005). The final instantaneous two dimensional vector field is shown in figure 6.12b.

The various characteristics of the flow can now be extracted from the vector fields. These results are discussed in chapters 7 and 8.

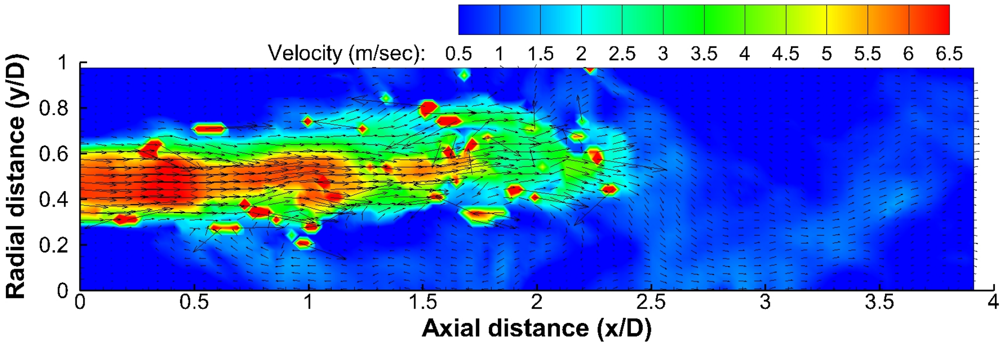

(a) Vector field obtained from camera-1 after cross-correlation.

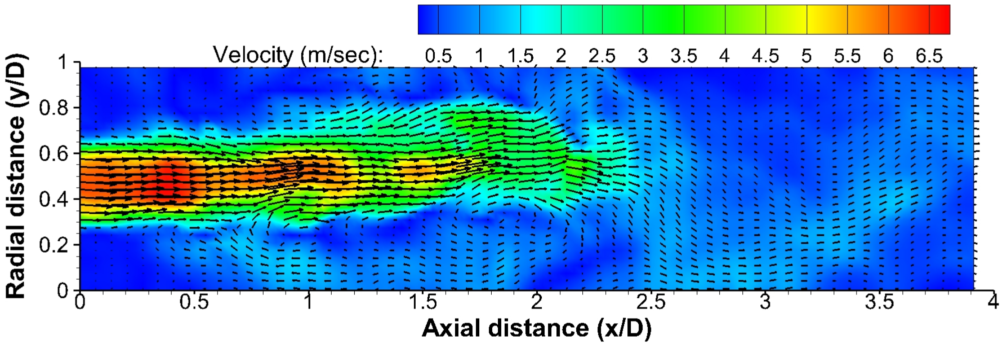

(b) Post processing of the vector field to remove spurious vectors.

Figure 6.12: Figures illustrating instantaneous vector fields obtained from camera-1 before and after image post processing. Contours show the velocity magnitude $\sqrt{u^2 + v^2}$ for a flow entering at $0.5\ m/sec$ through orifice PIV-S2.

6.6 Summary

This chapter described the experimental setup and instrumentation of the PIV experiments conducted on flow through orifices in pipes (section 6.2). The orifice geometries and the experimental conditions were presented in sections 6.3 and 6.4 respectively with table 6.10 providing an overview of the experimental parameters. The steps taken to process the PIV data were highlighted in section 6.5.

Chapter 7

Results: Velocity measurements

7.1 Introduction

The preceding chapter described the experimental setup and measurement conditions that were used during the PIV measurements (see summary in table 6.10). The recorded images are processed using techniques discussed in section 6.5 which result in a time series of two-dimensional vector fields, at each of the flow condition tested.

The velocity data can be used to extract several properties of the flow-field which are discussed in the present chapter. The first section outlines a few definitions that aid discussions in sections following it, which analyze features of the instantaneous and mean velocity field of both single and multiple hole orifices. Section 7.5 analyzes the behavior of the mean reattachment length, an important parameter commonly discussed in the context of separated flows. Finally, the proper-orthogonal-decomposition (POD) data analysis technique is implemented to identify the most energetic and coherent structures that are present in the flow downstream of orifices (section 7.6).

7.2 Definitions

7.2.1 Coordinate system

All results described here follow the co-ordinate system shown in figure 7.1. Length scales are normalized by the pipe diameter (D). Axial (stream wise) distances are specified with respect to the orifice exit (x=0) and the radial distances (y/D) are specified with respect to the lower end of the pipe. Positions inside the flow field are described as (x, y) = (axial distance x/D, radial distance y/D). The horizontal (axial) and vertical (radial) velocity components at a given instant t are denoted as $u(x, y, t)$ and $v(x, y, t)$, respectively.

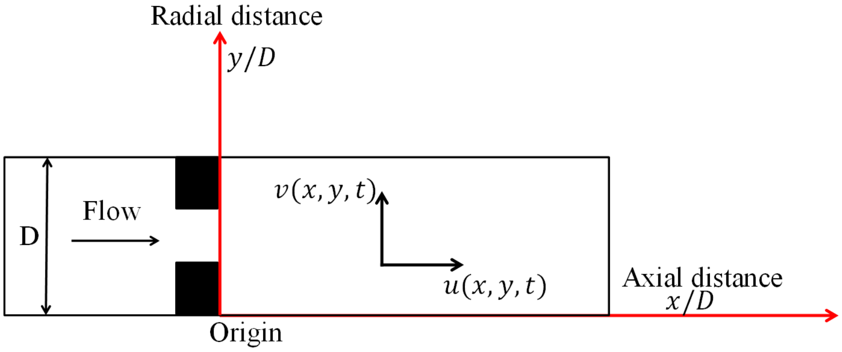

Figure 7.1: Co-ordinate system used to describe spatial locations and velocity-vector components.

7.2.2 Reynolds decomposition

For studying turbulent flows, the velocity components are usually expressed as a mean and a fluctuating component. For a two-dimensional vector field, $\mathbf{V}(x, y, t) = (u(x, y, t), v(x, y, t))$, this results in:

$$\mathbf{V}(x, y, t) = \bar{\mathbf{V}}(x, y) + \mathbf{V}'(x, y, t) \tag{7.1}$$

Where, $\bar{\mathbf{V}}$ represents the average flow-field and $\mathbf{V}'$ the fluctuating component.

7.2.3 Mean and Root mean square (RMS)

Consider a time series comprising of N statistically-independent, instantaneous samples of a two-dimensional vector field, $\mathbf{V}(x, y) = (u(x, y), v(x, y))$. The **mean** and **root-mean-square (R.M.S)** of such a series are mathematically given as,

$$\bar{\mathbf{V}} = \frac{1}{N}\sum_{i=1}^{N}\mathbf{V}_i \tag{7.2}$$

$$\mathbf{V}_{rms} = \sqrt{\frac{1}{N-1}\sum_{i=1}^{N}\left(\mathbf{V}_i - \bar{\mathbf{V}}\right)^2} \tag{7.3}$$

7.2.4 Reynolds stress

Application of Reynolds decomposition on the two-dimensional incompressible Navier-Stokes equations gives rise to additional terms referred to as Reynolds stresses or turbulent stress (Pope, 2000). For a two dimensional vector field, only three components of the

Reynolds stress tensor can be resolved and are calculated as,

$$\tau_{xx} = \frac{1}{N}\sum_{i=1}^{N}\big(u_i'(x,y).u_i'(x,y)\big) \tag{7.4}$$

$$\tau_{yy} = \frac{1}{N}\sum_{i=1}^{N}\big(v_i'(x,y).v_i'(x,y)\big) \tag{7.5}$$

$$\tau_{xy} = \frac{1}{N}\sum_{i=1}^{N}\big(u_i'(x,y).v_i'(x,y)\big) \tag{7.6}$$

7.2.5 Auto-correlation function

For an accurate description of the mean-features of the flow-field, the above definitions require consecutive samples to be statistically independent (uncorrelated) in time. The **autocorrelation function** describes the dependence of the data at one-point on values at another time. The autocorrelation function ($R_x(\tau)$) between values at two instances t and $t+\tau$ can be computed by,

$$R_x(\tau) = \lim_{T\to\infty}\frac{1}{T}\int_0^T x(t)x(t+\tau)dt \tag{7.7}$$

$$\rho_x(\tau) = \frac{R_x(\tau)}{R_x(0)} \tag{7.8}$$

Where, ρ_x is known as the **auto-correlation coefficient**. Since the auto-correlation function has a maximum value at $\tau = 0$, the auto-correlation coefficient, always lies between 0 and 1. The **integral time-scale** T_I, which is a measure of the time-separation over which signals are correlated can be computed as,

$$T_I = \int_0^\infty \rho_x(\tau)d\tau \tag{7.9}$$

Samples separated by $2\times T_I$ can be considered as statistically-independent (Bruun, 1995). An estimate for the integral time scale, is the time taken for the autocorrelation coefficient to decay from 1 to 0.

7.3 Single-hole orifice

This section presents some results from the PIV measurements on single hole orifices. The vector fields presented in this section correspond to a flow entering at 1 m/sec ($Re_P = 8350$) through orifice PIV-S2 ($\beta = 11\%, t/d_h = 0.5$).

7.3.1 Instantaneous flow field

Figure 7.2 presents an instantaneous vector field of the entire measurement region. The image is constructed by stitching the instantaneous velocity fields obtained after processing of images from both cameras. It is evident that most of the interesting features of the orifice jet are captured within the first 3 diameters by the first camera. Thus, all subsequent results are based on vector fields obtained from camera 1.

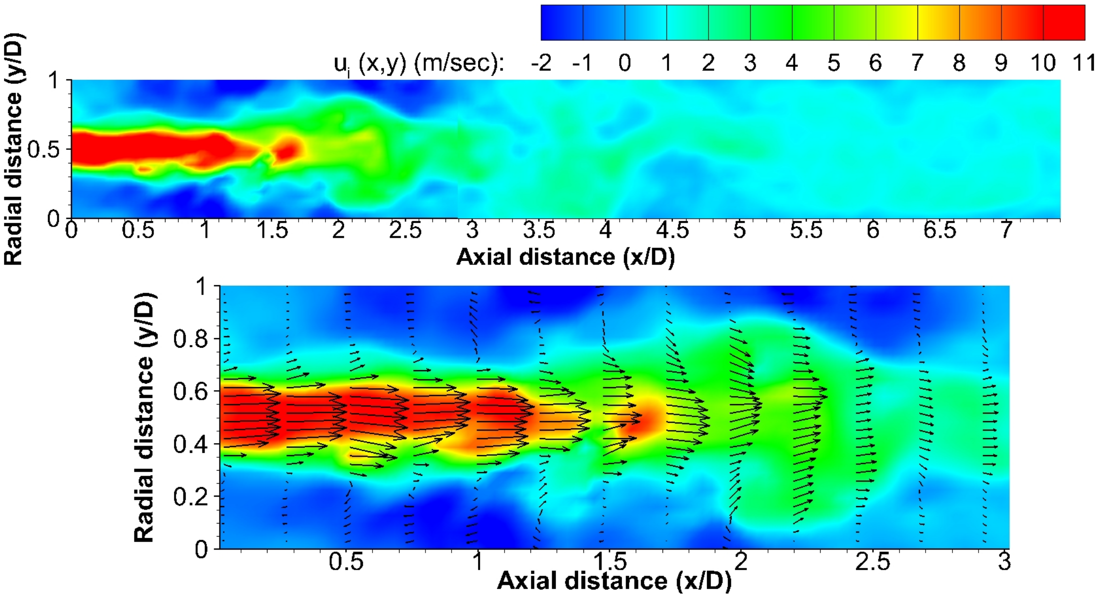

Figure 7.2: Instantaneous flow field downstream of PIV-S2 ($\beta = 11\%, t/d_h = 0.5$). Mean flow at the entrance of the orifice is 1 m/sec ($Re_P = 8350$). The contours show the instantaneous axial velocity $u_i(x, y, t)$. The bottom image zoomed over $(0 - 3D)$ showing every 1 in 8 vectors in the axial direction.

For a thin, sharp edged, single-hole orifice, the flow separates at the orifice inlet. Due to a sudden decrease in cross section area, the fluid accelerates and issues from the orifice in the form of a jet into the pipe downstream. The evolution of the jet is restricted by the walls of the pipe. As the adverse pressure gradient begins to relax, the flow reattaches to the walls and the boundary layer begins to re-develop.

This image captures the instance when the shear layers merge together at $(1.4D, 0.5D)$. The result reveals the large recirculation zones accompanying the jet with instantaneous velocities reaching as high as 2 m/sec inside this region. The vena-contracta, which is the narrowest portion of the jet, appears at $(0.35D, 0.5D)$. The velocity in the core is as high as 11 m/sec and is about 2 m/sec higher than that estimated using inviscid conservation of mass (equation 2.3). Large velocity gradients which are characteristic of shear layers are clearly visible (see zoomed in view of figure 7.2).

Additional features of the unsteady flow through a single-hole orifice are described in section 8.2 of chapter 8.

7.3.2 Characteristics of the mean flow

The integral time scale is a reasonable estimate of the time scale associated with the turbulent macro structure. When the downstream flow field has a wide range of flow scales the auto-correlation function at different locations in the flow are expected to yield different results (Tropea et al., 2007).

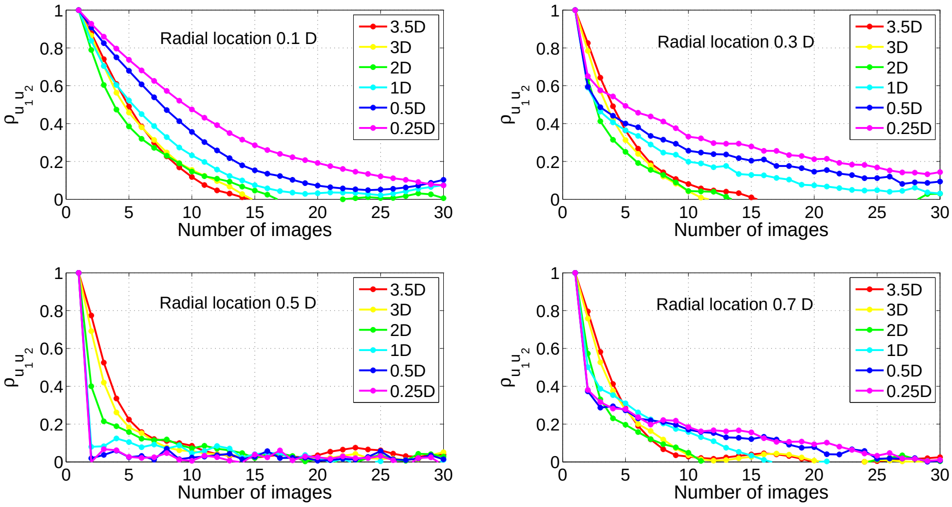

Figure 7.3: One point, two time, auto-correlation function $\rho_{u_1u_2}$ for flow through PIV-S2 ($\beta = 11\%, t/d_h = 0.5$) at $1\ m/sec$ ($Re_P = 8350$). Legend shows different axial distances (x/D) and each figure corresponds to the mentioned radial distance (y/D). Time separation between images is $1/1500\ s$.

Figure 7.3 presents the auto-correlation function $\rho_{u_1u_2}$ for a mean flow of $1\ m/sec$ through PIV-S2 ($\beta = 11\%, t/d_h = 0.5$), computed at different radial and axial locations downstream. The time separation between images is, $1/f_s = 1/1500\ s$. The following conclusions can be drawn from figure 7.3:

- The auto-correlation function shows very similar trends at axial locations 3D and 3.5D and over all the radial locations; with its value decaying to 0 after about 13 samples. So $(13 \times (1/1500)) = 8.6\ msec$ would be an approximate integral time-scale of the flow in this region. These points lie beyond the influence of the orifice jet and the recirculation region and the time scale of the fluid structures present here are expected to scale with the pipe diameter and flow speed as $\tau_{3D} \approx \frac{D_p}{U_p} = 8.4\ msec$.
- In the recirculation region, at radial distances $0.1D$, $0.3D$ and axial distances $< 2D$, the auto-correlation function shows high-correlation between consecutive samples.

The flow evolves much slowly inside this region and a high-sampling rate results in highly correlated images. The auto-correlation function approaches 0 only after 30 samples, which is $(30 \times (1/1500)) = 20\ msec$.

- Radial distances $0.5D$ and $0.7D$ are inside the core of the jet and in the shear layer respectively for all axial distances $< 3D$. It is evident that the decay of the auto-correlation function is the strongest here, partly due to the high velocity of the fluid inside the core of the jet.

The above analysis shows that to have completely uncorrelated samples in time, at each point in the flow, it would be necessary to perform a measurement with a very low sampling rate. In practise this is not always feasible and there is often no choice but to accept a degree of statistical uncertainty (Tropea et al., 2007).

In the present case, the ensemble averaged mean and root-mean-square of the flow-field are computed using 1 in every 10 samples, which is an effective sampling rate of 150 Hz. In total, 300 measurement samples are used. The uncertainty associated with these statistics are detailed in section A.2 of appendix A.

Average flow field

Figure 7.4a presents the axial velocity contours of the mean flow-field ($\bar{u}(x, y)$). The unsteady features of the flow that are visible in the instantaneous vector field are lost as a result of averaging. The relative uncertainty associated with the mean flow is $\epsilon_\mu = 2.7\%$ (see section A.2).

The axial symmetry of the mean flow is self evident[1]. The velocity of the jet reaches its peak value at about $(0.1D, 0.5D)$ from the orifice exit. The primary recirculation region extends till about $2.6D$ from the orifice (see figure 7.4b), with the peak reverse-flow occurring at about $1D$ downstream. The data also captures a secondary-recirculation region close to the wall at $0.1D$.

R.M.S flow field

Figure 7.5 presents the horizontal component of the R.M.S. The stable potential core of the jet $x \in (0 - 0.6D)$, centered around the pipe axis has the least fluctuation levels. The velocity fluctuations are prominent in the shear-layers surrounding the jet core, with large values being reached in regions where the shear layers interact with each other. This point is sufficiently far downstream from the orifice, a conclusion also made by Nicolleau et al. (2011). This region lies about $1D$ upstream from the point of reattachment. The peak turbulence-intensity u_{rms}/u_{jet}, is about 24%. The relative uncertainty in the estimation of the RMS is $\epsilon_\sigma = 11\%$ (see section A.2).

Reynolds stress

The three Reynolds-stress components (see equations 7.4 - 7.6) that are computed from the two-dimensional vector fields are presented in figure 7.6. The normal stress in the direction of flow τ_{xx} is about five times higher than the other two components. The component τ_{yy} reaches large values in regions where the shear layers interact with each other. The shear stress component τ_{xy} also attains large values between $1 - 2D$ from the orifice.

---

[1] Note, this observation does not hold for all the orifices that were tested. The mean flow field of some of the orifices were nor symmetrical. This asymmetry is discussed as a source of systematic error in section A.1 of appendix A.

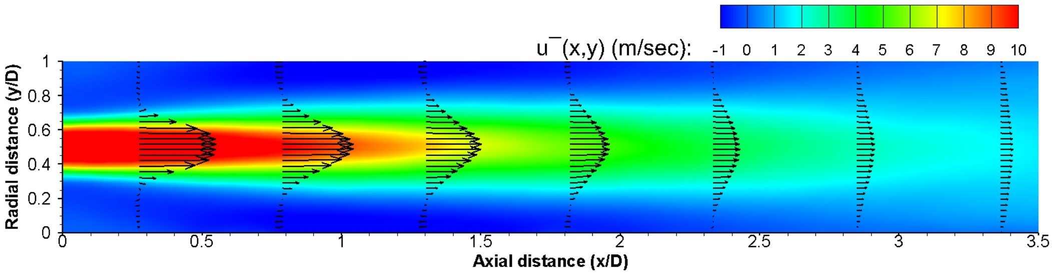

(a) Contours of the axial velocity component of the mean flow-field.

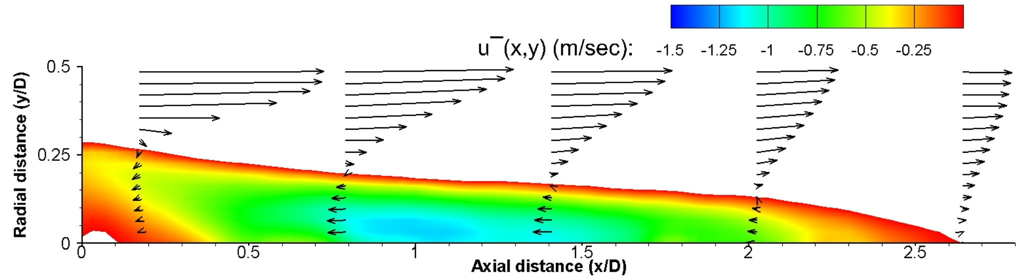

(b) Contours of the axial velocity component of the mean flow-field inside the lower recirculation region. $\bar{u} > 0$ have been disabled.

Figure 7.4: Figures illustrating the axial component of the mean flow-field $(\bar{u}(x, y))$, for flow through PIV-S2 $(\beta = 11\%, t/d_h = 0.5)$ at $1\ m/sec$ $(Re_P = 8350)$.

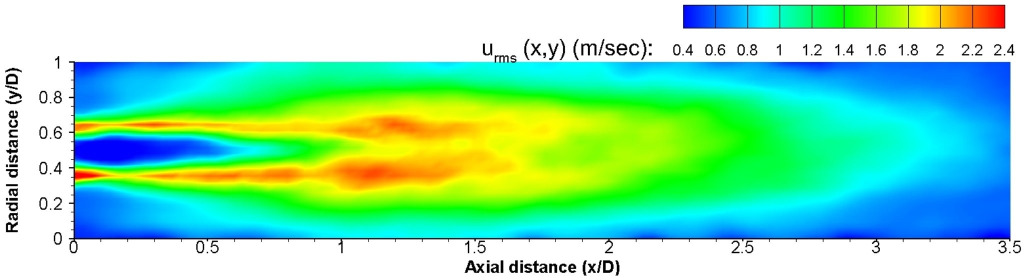

Figure 7.5: Contours of the axial velocity component of the R.M.S. $(u_{rms}(x, y))$ of the flow field.

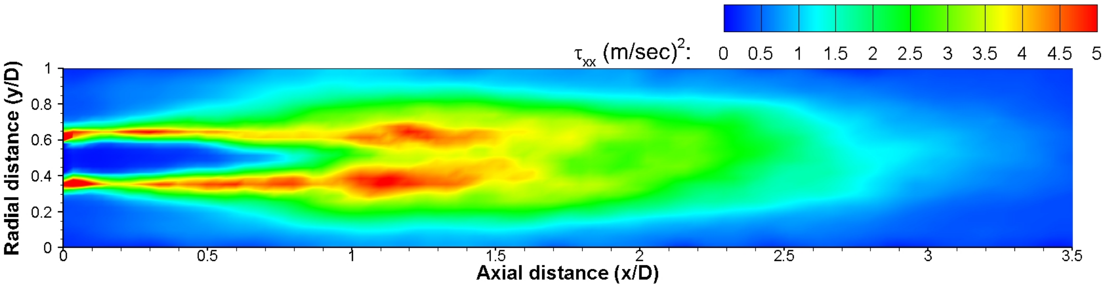

(a) Contours of τ_{xx}.

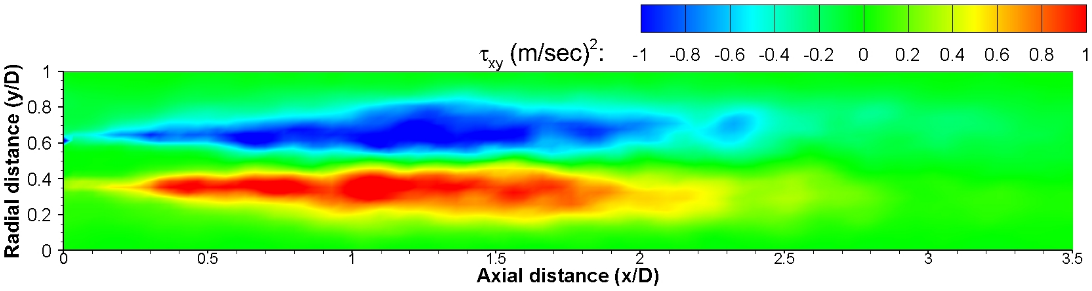

(b) Contours of τ_{xy}.

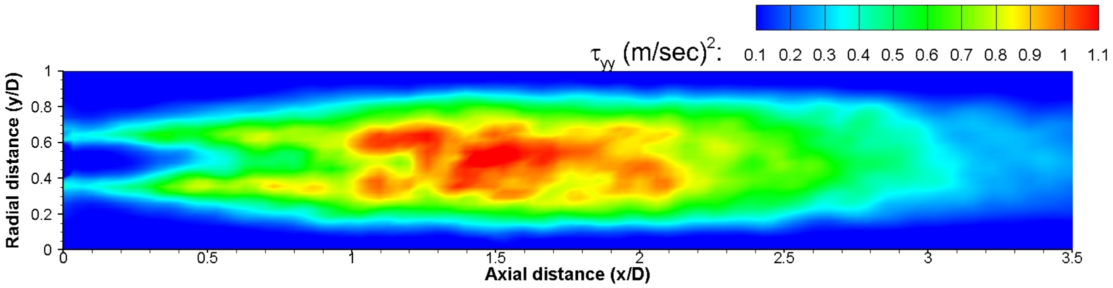

(c) Contours of τ_{yy}.

Figure 7.6: Mean contours of the three Reynolds stress components for a flow entering at 1 m/sec ($Re_P = 8350$) through orifice PIV-S2 ($\beta = 11\%, t/d_h = 0.5$)

7.3.3 Comparison to pressure measurements

Section 5.3.3 in chapter 5 presented results from wall pressure measurements on single hole orifices. Figure 5.6a showed that the non-dimensional P'_{rms} was maximum at 2D from the orifice. Furthermore, the RMS of the pressure fluctuation levels at 1D were higher than that at 3D from the orifice.

Figure 7.5 shows that the RMS of the velocity fluctuations at 3D from the orifice are much lower compared to regions between 1-2D from the orifice. The interaction between the shear layers of the orifice jet appear to be the highest at these locations which are upstream of the mean reattachment point ($2.6D$). It can be thus concluded that the peak pressure and velocity fluctuations occur in the upstream vicinity of the mean reattachment point. This parameter is discussed in further detail in section 7.5.

7.4 Multiple-hole orifice

This section is devoted to analyzing the flow downstream of the 7-hole multiple hole orifice. The orifice geometry and the plane of measurement were presented previously in figure 6.6. The multiple hole orifice has a porosity and thickness-ratio of $\beta = 19\%$, $t/d_h = 1.07$ respectively. This value of the thickness ratio can cause the flow inside the orifice hole to reattach (Maynes et al., 2013).

7.4.1 Instantaneous flow field

Figure 7.7 shows an instantaneous vector-field of the axial velocity component $u(x, y)$, for flow through the investigated multi-hole orifice plate (PIV-M1, $\beta = 20\%$ and $t/d_h = 1.07$). The flow enters the orifice at 1 m/sec ($Re_P = 8350$).

The three-jets issuing from the holes lying inside the measurement plane are captured clearly. The maximum velocity reached in each of the jets are very similar, with the middle-jet appearing over a larger extent downstream. A small recirculation zone is present till about $1D$ from the orifice. Beyond $1.5D$, the flow is attached at all locations and the boundary layer starts to develop.

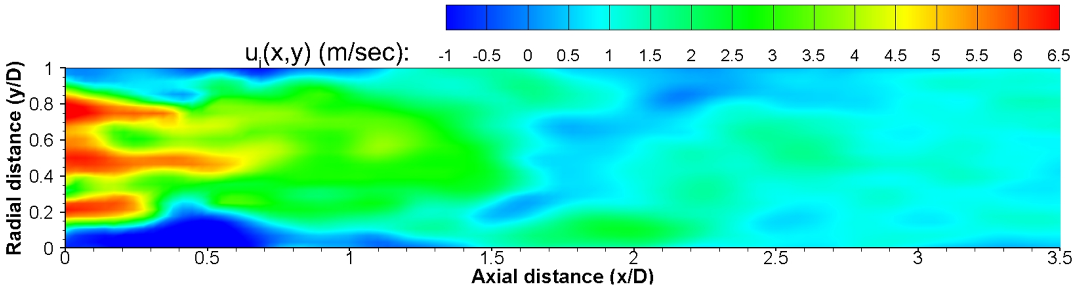

Figure 7.7: Instantaneous flow field through PIV-M1 ($\beta = 20\%, t/d_h = 1.07$), flow enters at 1 m/sec ($Re_P = 8350$), showing contours of axial velocity.

The instantaneous vectors indicate a strong interaction between the jets. These features of the unsteady flow are described in section 8.2.2 of chapter 8.

7.4.2 Characteristics of the mean flow

Figure 7.8 presents the auto-correlation function at different points in the flow-field. Similar to the single-hole orifice, the downstream flow-field has a wide range of flow scales due to which the auto-correlation function at different points yields different results (Tropea et al., 2007).

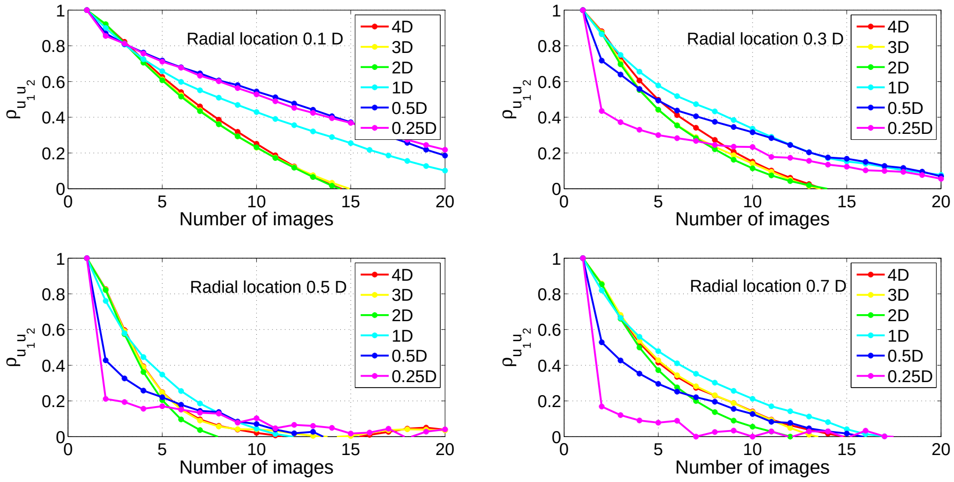

Figure 7.8: One-point, two-time, auto-correlation function $\rho_{u_1u_2}$ for flow through PIV-M1 ($\beta = 19\%, t/d_h = 1.07$), mean-flow at $1\ m/sec$ ($Re_P = 8350$). Legend shows different axial distances and each figure corresponds to the mentioned radial distance. Time separation between images is $1/1500\ s$.

Far downstream from the orifice (axial distance $\geq 2D$), the auto-correlation function shows the same trend over all the radial locations, with $\rho_{u_1u_2}$ reaching close to 0 after 14 samples. Inside the recirculation zone, radial distance $0.1D$ and axial distance $< 1D$, consecutive images are highly correlated due to the slow evolution of the flow in this region. At points directly under the influence of the orifice jets, the auto-correlation function drops sharply (see radial distances $0.5D$ and $0.7D$ and axial distance $< 1D$ in figure 7.8).

Keeping the above analysis in mind, the ensemble-averaged mean and root-mean-square of the flow field are computed using 1 in every 10 samples, which is an effective sampling rate of 150 Hz. In total, 300 measurement samples are used.

Average flow-field

The streamwise velocity-component of the mean flow-field is shown in figure 7.9. The velocity profiles show the presence of three jets but the dynamics of the flow processes occurring are lost due to averaging. The mean axial flow field appears symmetric about the pipe axis ($y = 0.5\ \forall\ x > 0$).

The velocity magnitude of the central jet is measured to be higher than its neighbours on either sides. Since the central hole is surrounded by 6 neighbouring holes, it is expected to be influenced by them. This increase in velocity is perhaps due to entrainment of the central jet by the surrounding jets. Furthermore, the top and the bottom holes (in figure 7.9) are nearer to the walls and perhaps its influence leads to a minor decrease in the observed flow speed.

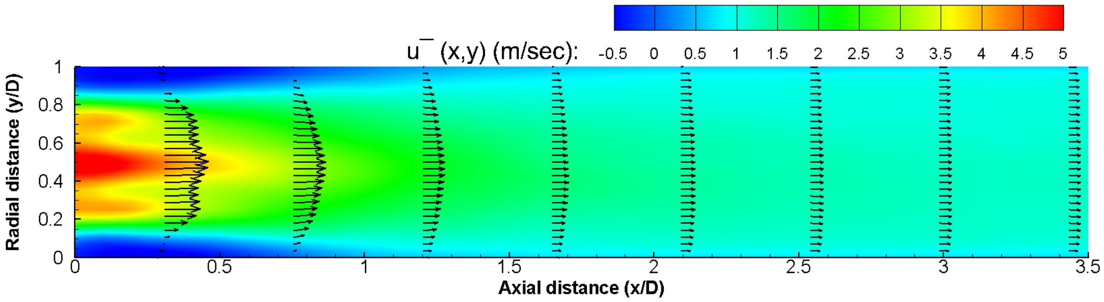

Figure 7.9: Contours of the axial velocity component of the mean flow field. Flow enters the single-hole orifice at $1\ m/sec$ ($Re_P = 8350$).

R.M.S flow-field

Figure 7.10 presents the axial component of the R.M.S. of the flow-field. The results indicate that velocity fluctuations are the highest in regions immediately downstream of the holes close to the walls, $y = 0.3D$ and $y = 0.7D$. A visual inspection of the vector series indicates a strong interaction between the central jet and its neighbours. It was seen that the middle jet dominated while intermittently interacting with the neighbouring jets. This interaction could explain the relatively low RMS values in the center ($y = 0.5D$), whereas higher fluctuation levels near the other two jets (see section 8.2.2 of chapter 8).

The flow is expected to be highly three dimensional and the observed asymmetry (with respect to the pipe axis) is likely due to this. Note however that the RMS decreases strongly at distances beyond $0.5D$ from the orifice.

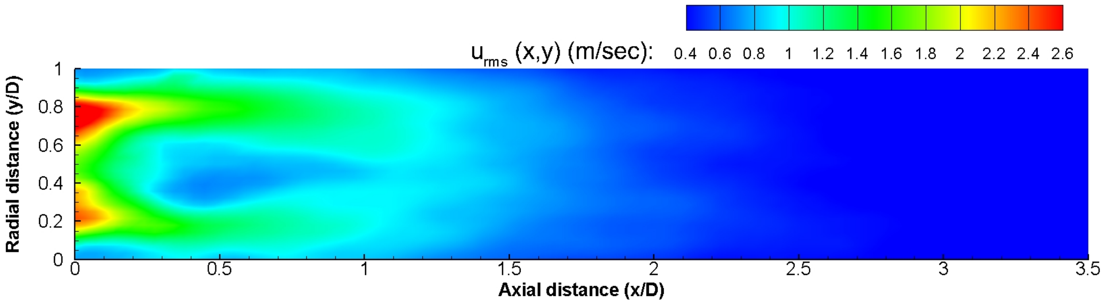

Figure 7.10: Contours of the axial velocity component of the R.M.S. of the flow field. Flow enters the multi-orifice at $1\ m/sec$ ($Re_P = 8350$).

Reynolds stress

Figure 7.11 presents the normal and shear stress components of the Reynolds stress tensor that can be obtained from the present two-dimensional vector fields. The result indicates that the normal stresses (τ_{xx} and τ_{yy}) reach their peak values in the vicinity of the top and bottom hole. The Reynolds shear-stress (τ_{xy}) shows that regions where the shear layers of neighbouring jets interact $y = 0.3D$ and $y = 0.6D$, the shear stress is reduced when compared to the shear layers close to the wall $y = 0.2D$ and $y = 0.8D$. An asymmetry in figure 7.11a is present again perhaps due to the three-dimensional nature of the flow in this region.

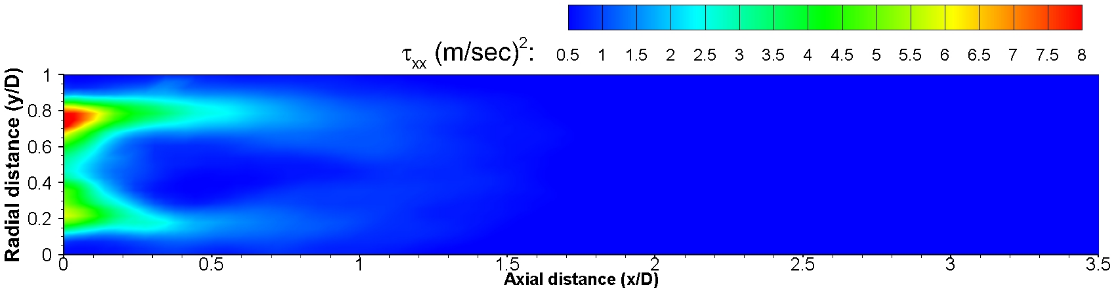

(a) Contours of τ_{xx}.

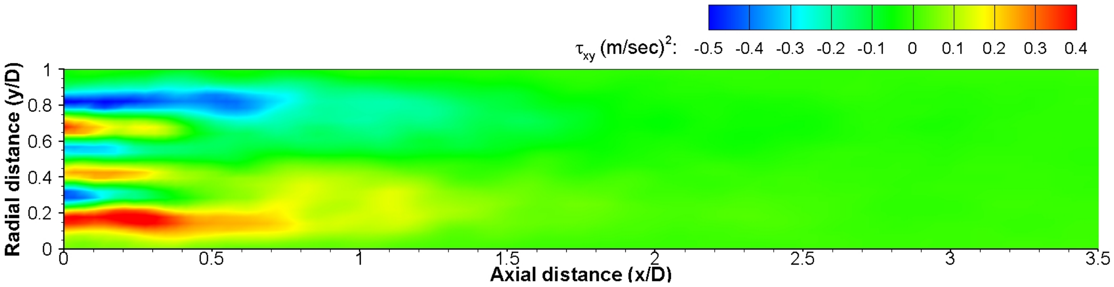

(b) Contours of τ_{xy}.

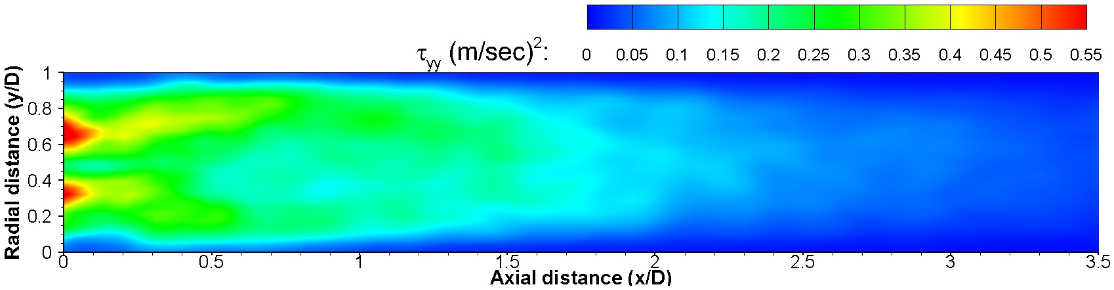

(c) Contours of τ_{yy}.

Figure 7.11: Figures presenting the iso-contours of the three Reynolds stress components for flow through PIV-M1 ($\beta = 20\%, t/d_h = 1.05$) at $1\ m/sec$ ($Re_P = 8350$).

7.4.3 Comparison to single hole orifice

In comparison to the single hole orifice, the peak RMS values for a multiple hole orifice occur much closer to the plate. This observation is in line with those reported by Nicolleau et al. (2011) and that observed from the pressure measurements discussed in section 5.5.

Furthermore, velocity fluctuations from multiple hole orifices decay faster (see figure 7.10), a trend which was also noticed in P'_{rms} of the wall pressure fluctuations discussed in section 5.5.

7.5 Mean reattachment-point

In separated flows, an important parameter that defines the extent over which the flow remains separated is the **mean reattachment-point** (X_r) (Schetz & Fuhs, 1999). It provides a length scale for the primary recirculation region.

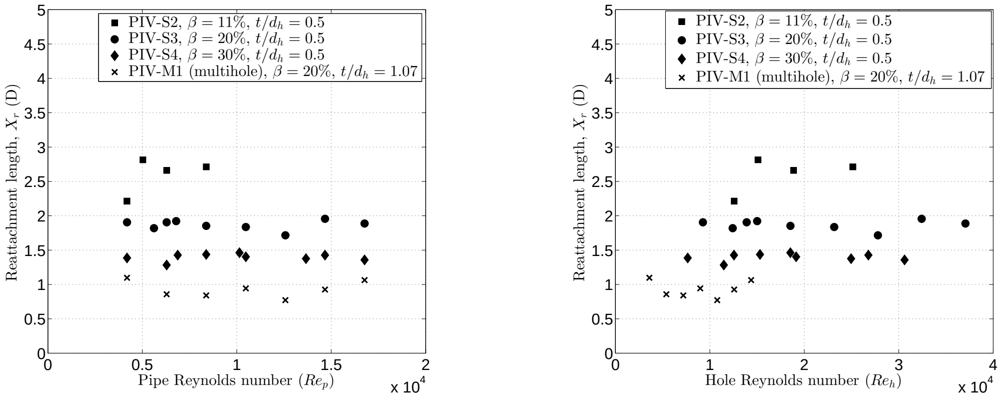

(a) X_r as a function of pipe Reynolds-number. **(b)** X_r as a function of hole Reynolds-number.

Figure 7.12: Plot of the mean reattachment-length (X_r), as a function of Reynolds number for all orifices.

Averaging of all the instantaneous vector fields ($N = 3000$) results in a mean flow field. The vectors closest to the walls are analysed and the point where the horizontal velocity component of the mean flow changes sign from positive to negative is taken as an estimate of the mean reattachment point. Since the vector pitch (distance between two neighbouring vectors) is 0.28 mm or $0.034D$, the relative uncertainty of this location (with respect to the pipe diameter) is 3.4%.

The mean reattachment points observed near the upper and lower walls were not identical. Among the orifices reported in this section, at a given flow condition, the maximum difference in the reattachment distances observed on the upper and lower wall surfaces for flow through orifice PIV-S2 was $0.03D$, through PIV-S4 was about $0.3D$ and for flow through PIV-S3 was within $0.5D$. For the multi-hole orifice, these points were less than $0.2D$ of each other for a given test condition. Note, this asymmetry is discussed as a source of systematic error in section A.1 of appendix A.

Though the trends shown by the reattachment distances near the upper and lower wall were the same, the final value reported here, are the average of the reattachment distances measured near the upper and lower wall.

Figure 7.12a presents the mean-reattachment location as a function of the flow Reynolds-number (Re_p), for all single-hole orifices with $t/d_h = 0.5$ and the multiple-hole orifice tested. Though the inlet flow conditions used during the measurements were similar, the velocity in the core of the orifice jet, being a function of the orifice geometry are different. Therefore, the mean reattachment-lengths are also presented as a function of the hole Reynolds-number in figure 7.12b.

From figure 7.12 it is observed that in the current measurement range, the mean reattachment-point does not present strong variations with Reynolds number. This trend is similar to those observed from measurements of turbulent flow over a backward-facing-step (Armaly et al., 1983). For a given, t/d_h, a single-hole orifice with the lowest porosity has the largest mean reattachment length, and thus the largest recirculation zone surrounding the jet. As the orifice diameter increases, the mean reattachment point moves upstream implying that smaller recirculation regions surround the orifice-jet.

The mean reattachment-lengths measured for the multiple hole orifice tested is also shown in figure 7.12. It is interesting to see that the multiple-hole orifice presents a Reynolds number dependency similar to the single-hole orifice. It has the shortest reattachment length, compared to all other orifices, perhaps due to a greater degree of mixing and interaction between the jets and due to their proximity to the pipe wall.

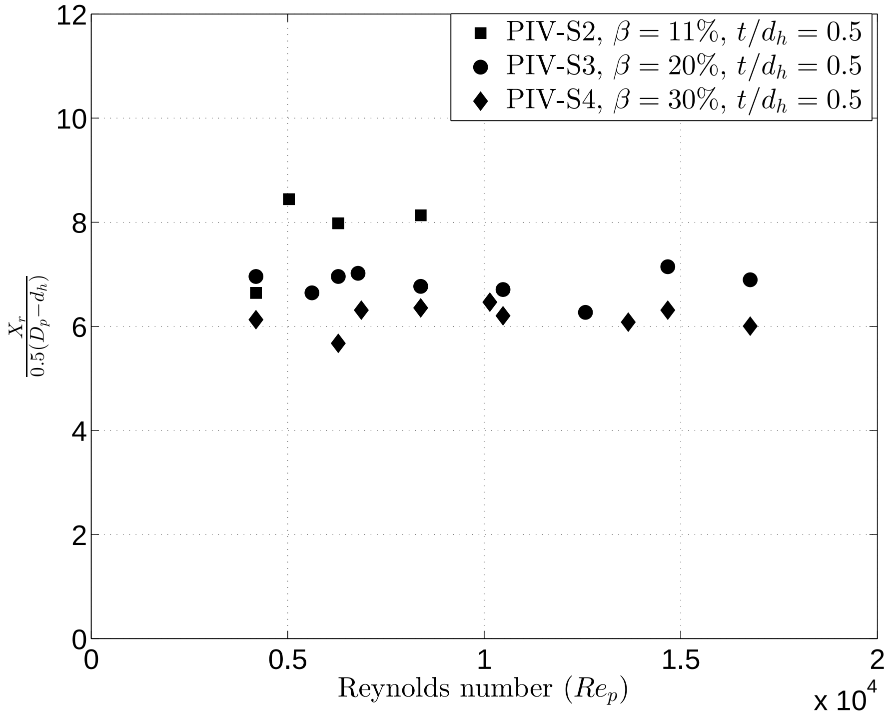

Figure 7.13: Mean reattachment length normalized by $0.5 \times (D_p - d_h)$, (equivalent step-height) as a function of Re_p for **single-hole orifices**.

The above mentioned observations indicate that the mean reattachment lengths behave similar to those reported for the backward facing step (BFS). This motivates the scaling of the reattachment-length with the "step height", which in the present case can be regarded as $0.5 \times (D_p - d_h)$ (say equivalent step-height).

Figure 7.13 presents the normalized reattachment length for all the single-hole orifices with $t/d_h = 0.5$ but having different porosities. It can be inferred that for the present measurement range all the reattachment points seem to lie at about $6 - 8$ equivalent step-heights from the orifice. This behavior is similar to the weak variation of the mean reattachment-length normalized by the step-height ($X_r/h \approx 6$) observed for the backward-facing step (Jovic & Driver, 1995). This result needs to be investigated further over a larger geometrical range of orifice plates.

In BFS, variations in the normalized reattachment-length (X_r/h) for different step-heights are attributed to a difference in expansion ratio (ratio of the downstream to upstream channel height) (Kuehn, 1980). For turbulent BFS flows, the mean reattachment length was found to increase with increasing expansion ratio (Le et al., 1997). The expansion ratio is a measure of the adverse pressure gradient acting on the separated shear-layer (Adams & Johnston, 1988). For an orifice flow, D_p/d_h can be considered as a measure of the expansion ratio and similar to BFS, the reattachment length is seen to increase with the expansion ratio.

Given the highly unsteady nature of the flow expected at the reattachment location, the lengths shown above are used as approximate length-scales for normalization (see section 8.3). The average reattachment length for different orifices are tabulated in table 7.1. Results from other single-hole orifices are omitted (PIV-S10 and PIV-S11) due to a large asymmetry in the downstream flow-field (see section A.1).

Plate label	Hole-diameter $d_h (mm)$	Expansion ratio D_p/d_h	Mean reattachment-length X_r (D)	$\frac{X_r}{(0.5\times(D_p-d_h))}$
PIV-S2	2.8	3	2.72	8.1
PIV-S3	3.8	2.2	1.87	6.8
PIV-S4	4.6	1.82	1.4	6.2

Table 7.1: Average of the mean reattachment-lengths of single-hole orifices using data for $Re_p > 5000$. Pipe-diameter $D_p = 8.4\ mm$

7.6 Proper Orthogonal Decomposition (POD)

An experimental technique like PIV, provides a large amount of data describing the flow-field. Proper-orthogonal-decomposition (POD) is an advanced data-analysis technique which strives to make optimum use of this information. It was first introduced in the context of fluid-mechanics to identify coherent-structures by Lumley (1967). In the present investigation, the flow field is analysed using 'snapshot-POD' (Sirovich, 1987). Meyer et al. (2007) gives a step-by-step description for implementing POD and this is summarized below.

Each instantaneous planar vector-field $\mathbf{V}(x,y) = u(x,y), v(x,y)$, is regarded as a single snap-shot. N consecutive, statistically-independent snapshots are used to first calculate the mean-flow $\bar{\mathbf{V}}$, which can be regarded as the 0^{th} mode of the system. Subtraction of the mean from the instantaneous vector-fields leaves behind just the fluctuations $\mathbf{V}'(x,y) = u'(x,y), v'(x,y)$. If each snapshot has M vectors then, the fluctuating components of each snapshot are arranged as,

$$\mathbf{U} = \left[\mathbf{V'^1} \quad \mathbf{V'^2} \quad \mathbf{V'^3} \ldots \mathbf{V'^N}\right] = \begin{pmatrix} u'^1_1 & u'^2_1 & \cdots & u'^N_1 \\ u'^1_2 & u'^2_2 & \cdots & u'^N_2 \\ \vdots & \vdots & \vdots & \vdots \\ u'^1_M & u'^2_M & \cdots & u'^N_M \\ v'^1_1 & v'^2_1 & \cdots & v'^N_1 \\ v'^1_2 & v'^2_2 & \cdots & v'^N_2 \\ \vdots & \vdots & \vdots & \vdots \\ v'^1_M & v'^2_M & \cdots & v'^N_M \end{pmatrix} \tag{7.10}$$

The auto-covariance matrix is created as,

$$\tilde{C} = \mathbf{U}^T\mathbf{U} \tag{7.11}$$

and the corresponding eigen-value problem is solved.

$$\tilde{C}\mathbf{A}^i = \lambda^i \mathbf{A}^i \tag{7.12}$$

The solutions are ordered according to the size of their eigen-values as,

$$\lambda^1 > \lambda^2 > \lambda^2 > \cdots \lambda^N \tag{7.13}$$

The normalized POD modes ϕ^i are then constructed using the n^{th} component of the eigen-vector, A^i_n, corresponding to the eigen-value λ^i as,

$$\boldsymbol{\phi^i} = \frac{\sum\limits_{n=1}^{N} A^i_n \mathbf{V'^n}}{\left\| \sum\limits_{n=1}^{N} A^i_n \mathbf{V'^n} \right\|}, \quad i = 1, 2, \cdots N \tag{7.14}$$

Each instantaneous snapshot can be expressed with respect to the function basis formed by the POD modes as,

$$\mathbf{V^n} = \bar{\mathbf{V}} + \sum_{i=1}^{N} a_i^n \boldsymbol{\phi^i} \tag{7.15}$$

The POD coefficients a_i, are determined by projecting the fluctuating part of the velocity field onto the POD-modes as,

$$\mathbf{a^n} = \boldsymbol{\Psi^T V'^n} \tag{7.16}$$

where, $\boldsymbol{\Psi} = \left[\boldsymbol{\phi^1 \phi^2} \cdots \boldsymbol{\phi^N}\right]$ are the spatial POD-modes which are also called *topo*-modes. The POD coefficients contain temporal information related to the spatial structures and are known as *chrono*-modes. This temporal information gives access to the frequencies dominant in each mode, provided the snapshots represent a time-resolved sequence. In general, more than a single frequency is associated with each structure (Semeraro et al., 2012).

The eigenvalues reflect the relative kinetic energy associated with the corresponding mode. The ordering of the eigenvalues in equation 7.13 results in the first few modes being the most energetic modes. Most often, these are also the largest flow structures.

Snapshot-POD is implemented using MATLAB on the PIV vector-fields obtained for flow through single and multiple hole orifices. The following sub-sections presents these results.

7.6.1 Single-hole orifice

The snapshot POD is first applied to the vector fields of the single hole orifice. For consistency, the results presented here correspond to a flow entering at 1 m/sec ($Re_P = 8350$) through orifice PIV-S2 ($\beta = 11\%, t/d_h = 0.5$).

Convergence test

This section tests the convergence of the POD modes by following the approach of Semeraro et al. (2012). The POD modes obtained from a given data set depend mainly on the total number of snapshots N and the time interval between two consecutive snapshots. To extract physically relevant information from the data-set, N has to be chosen so that there are enough independent samples to ensure converged statistics, and that the time spanned by the snapshots is long enough to contain the slowest scales of the flow.

The present measurement data have been acquired at 1500 Hz for a duration of 2 s. Therefore, in total 3000 snapshots are available. To select a suitable time separation, the above mentioned procedure is implemented for three different time-separations namely, $\{5/1500, 10/1500, 15/1500\}$ which result in $\{600, 300, 150\}$ snapshots respectively. During the convergence test, the contribution of the mean flow from the snapshots is not subtracted. This is to determine the affect of choice of data set on the mean flow, which is expected to be the first mode.

Figure 7.14 presents the eigen values of the modes obtained using different time-separations between snapshots. The eigen value corresponding to the first mode, which as mentioned previously is the mean flow is reached using all three time steps. The mean flow contributes to about 86% of the total energy. The figure indicates that the eigen values

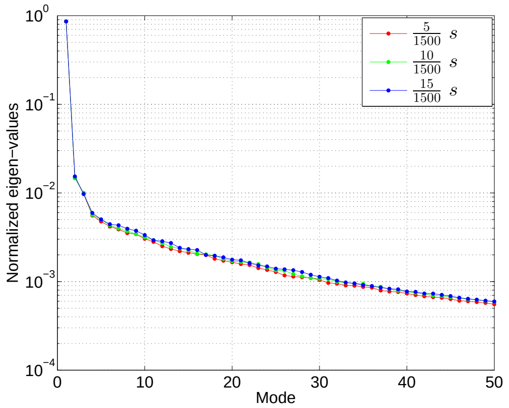

Figure 7.14: Normalized eigen-values of the modes computed using three different time-separations namely, $\{5/1500, 10/1500, 15/1500\}$ s. Note, the first mode shown here is the mean-flow as the contribution of the mean has *not* been subtracted from the snapshots.

of the first few modes (about 11) are almost identical for time-separations $5/1500s$ and $10/1500s$. The eigen values of the modes computed using a time separation of 15/1500 matches the other two till the first 6 modes. Thereafter, it presents deviations with occasional overlap with the other curves. The structural similarity between the initial modes resulting from the aforementioned time steps is also analysed and found to be similar, with observable differences resulting from the changing data set sizes.

Implementation and results

Since only the first few modes are of interest, a time step of $5/1500$ s between snapshots is used. The contribution of the mean-flow is subtracted from each snapshot and the procedure described earlier is implemented. Results shown below are obtained using a data set of 600 snapshots.

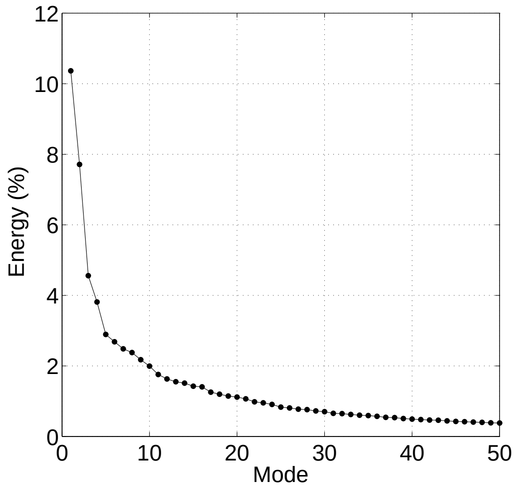

Figure 7.15: Eigenvalues of the first 50 modes shown as a percentage of the total energy of the fluctuating velocity field. Note, now the contribution of the mean flow has been subtracted.

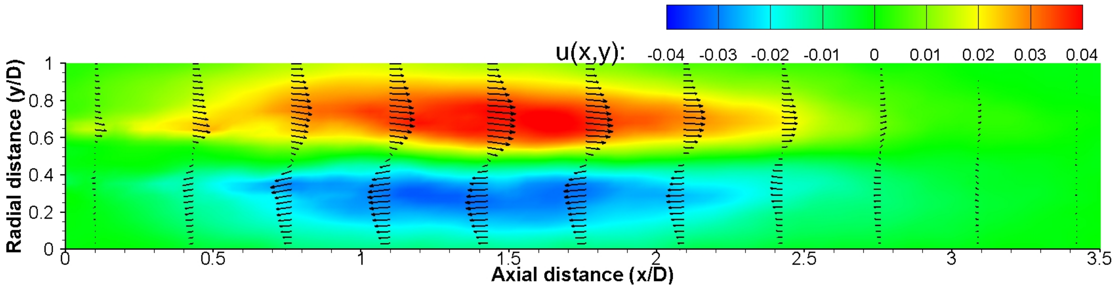

(a) Mode 1, Energy-10.36%

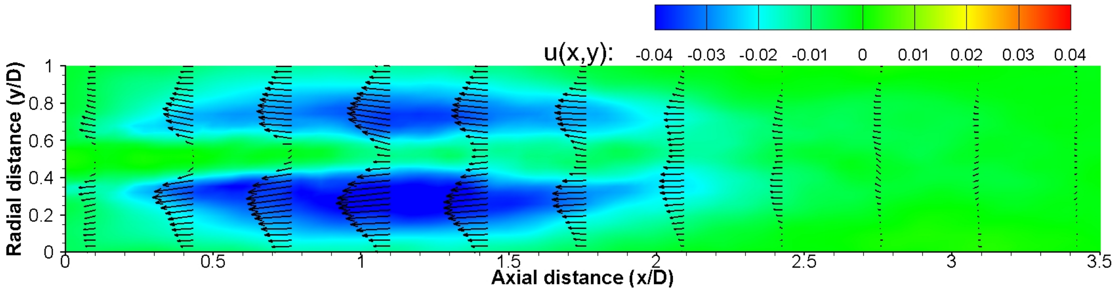

(b) Mode 2, Energy-7.71%

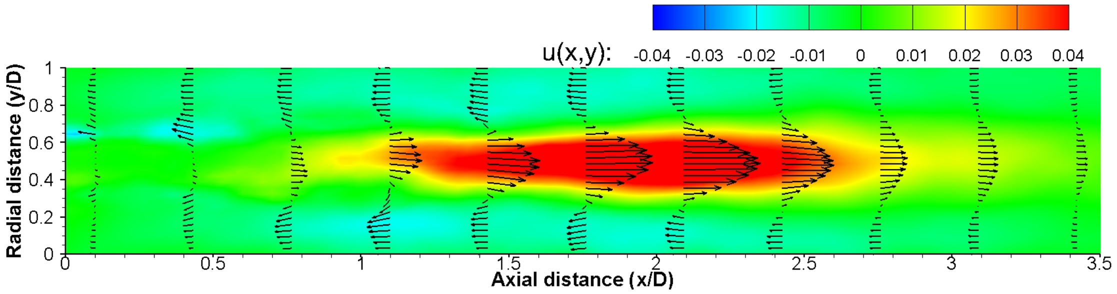

(c) Mode 3, Energy-4.56%

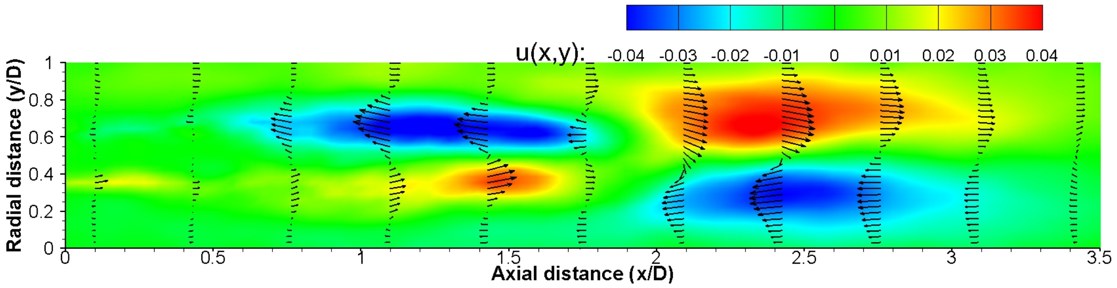

(d) Mode 4, Energy-3.81%

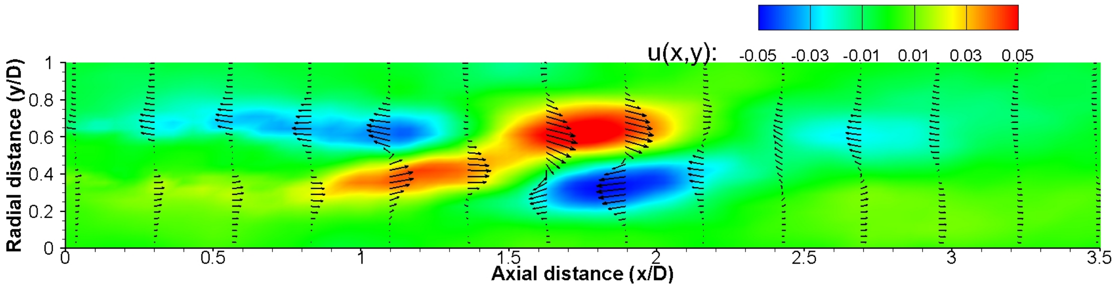

(e) Mode 5, Energy-2.9%

Figure 7.16: Modes 1 to 5 and their corresponding energy contribution. The contours show the normalized axial-velocity magnitude $u(x, y)$. Flow enters the single hole orifice PIV-S2 ($\beta = 11\%, t/d_h = 0.5$) at $1\ m/sec$ ($Re_P = 8350$).

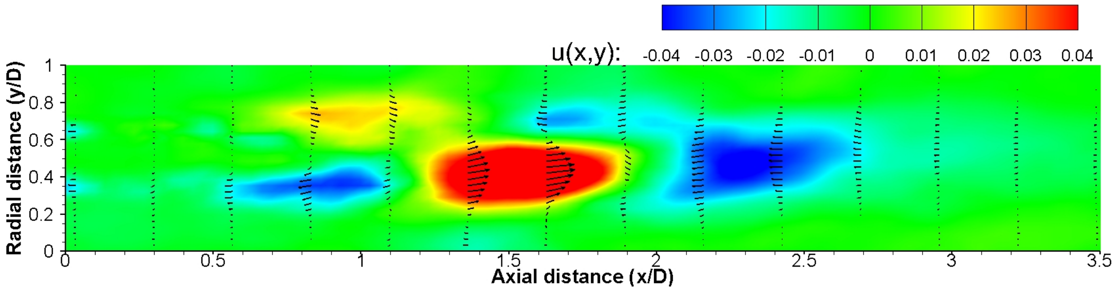

(a) Mode 6, Energy-2.69%

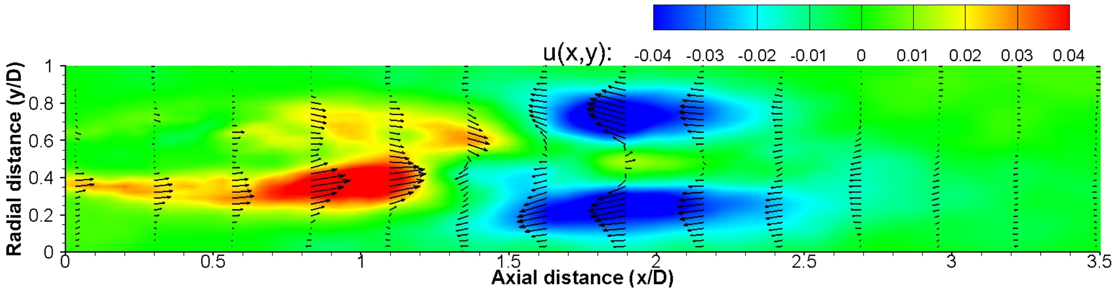

(b) Mode 7, Energy-2.48%

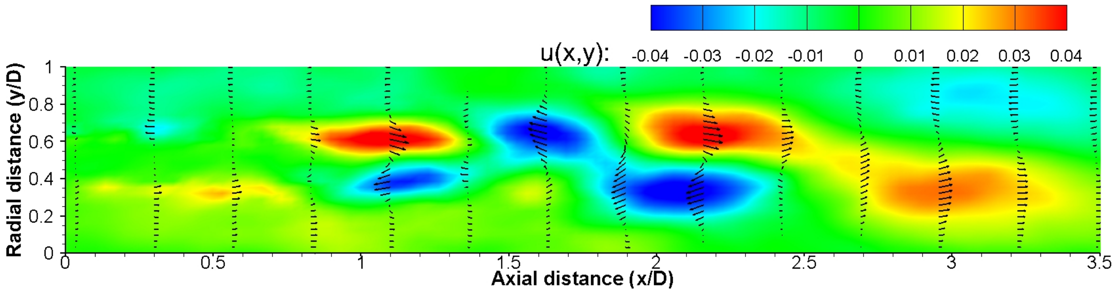

(c) Mode 8, Energy-2.39%

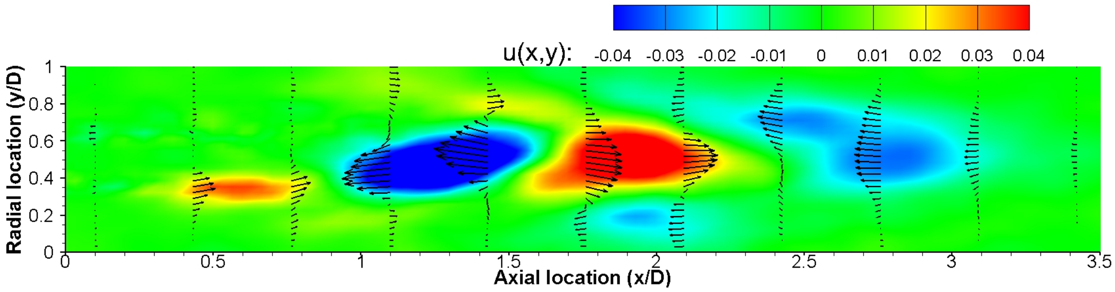

(d) Mode 9, Energy-2.18%

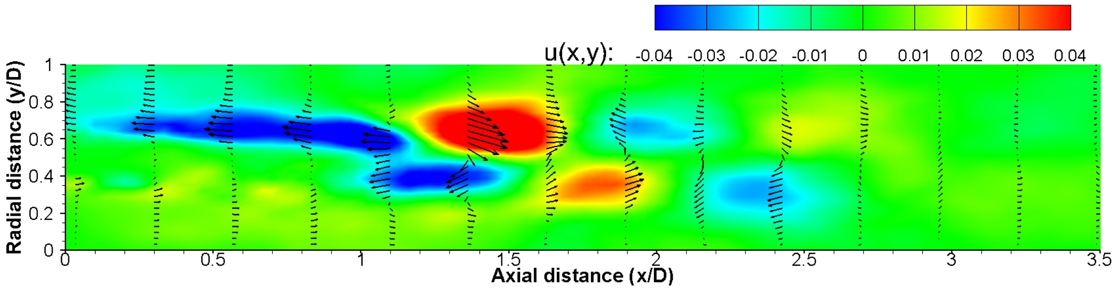

(e) Mode 10, Energy-2.0%

Figure 7.17: Modes 6 to 10 and their corresponding energy contribution. The contours show the normalized axial-velocity magnitude $u(x,y)$. Flow enters the single hole orifice PIV-S2 ($\beta = 11\%, t/d_h = 0.5$) at $1\ m/sec$ ($Re_P = 8350$).

Hereafter, the mean-flow is referred to as the 0^{th} mode. Figure 7.15 presents the energy associated with the first 50 eigen modes. The POD algorithm arranges the modes in a decreasing order of energy and thus the first few modes correspond to the most dominant (energetic) flow structures. The first 10 modes and their corresponding energy contributions to the total fluctuations are shown in figures 7.16 and 7.17 where the contours show the normalized axial velocity $u(x, y)$.

Interpretation of POD modes

The eigenmodes obtained from a POD analysis relate to coherent structures present within the flow. Physically, each eigenmode can be considered as capturing dominant characteristics of the flow and should not be misinterpreted as instantaneous physical structures (Van Oudheusden et al., 2005).

In the present case, the first three modes contribute about 23% to the fluctuations present in the flow. By analysing the modes along with the mean flow-field, the physical phenomenon that the modes represent could be understood. Figure 7.18a presents the normalized mean flow field (mode 0). Some interesting observations that can be made are:

- Mode-1 (figure 7.16a) extends from the orifice exit, till about $2.5D$ downstream and spans about half the pipe diameter (note $X_r = 2.6D$ here). Figure 7.18b illustrates the effect of mode-1 on the normalized mean. In terms of flow physics, this mode seems to indicate an upward deflection of the orifice jet while the flow in the lower recirculation zone moves upstream. This mode could represent a flapping motion of the orifice jet about the pipe centerline. This observation is further investigated by analysing the temporal information stored in the POD-coefficients. These observations are discussed further in section 8.4.1 dedicated to understanding the unsteady flow characteristics.

- The size of the flow structures represented by mode-2 (figure7.16b) are similar to mode-1, with their energy contribution to the fluctuations about 3% lower. Figure 7.18c shows that this mode represents the constriction (narrowing) and shortening of the orifice jet perhaps by the action of the fluid in the recirculation regions. It is thus observed that the largest flow structures (first two modes) extend approximately till the mean reattachment length and are dominant within the recirculation zones.

- Mode-3 is perhaps a representative of the flow structures that appear to break-off intermittently from the jet (see figure 8.1). These are visualized in the form of a longitudinal expansion of the jet in figure 7.18d.

- Mode-5 onwards (see figures 7.16e and 7.17), the size of the flow structures start reducing, with higher modes corresponding to smaller flow structures. These higher modes become more difficult to interpret, though a few modes appear complementary to each other (for example mode 6 and 9; mode 7 and 10).

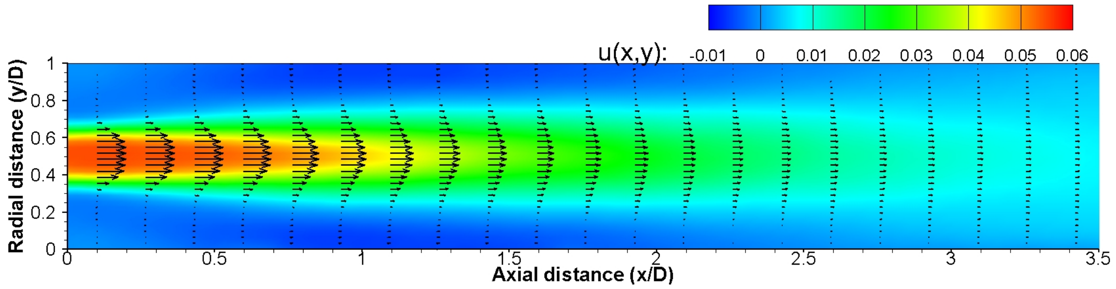

(a) Mode-0, Mean-flow

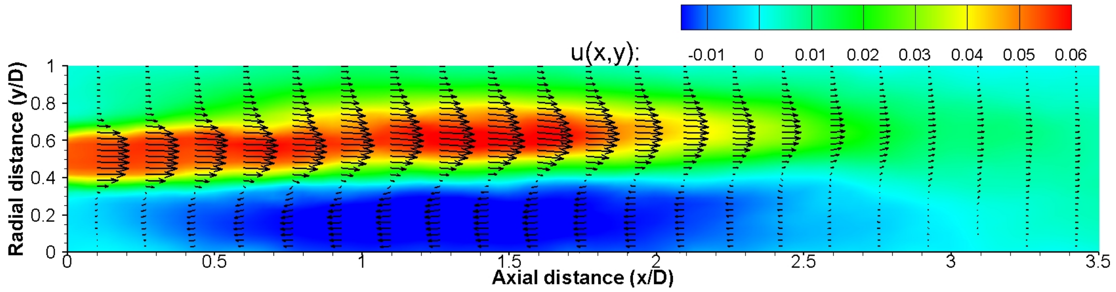

(b) Mode-0 + Mode-1

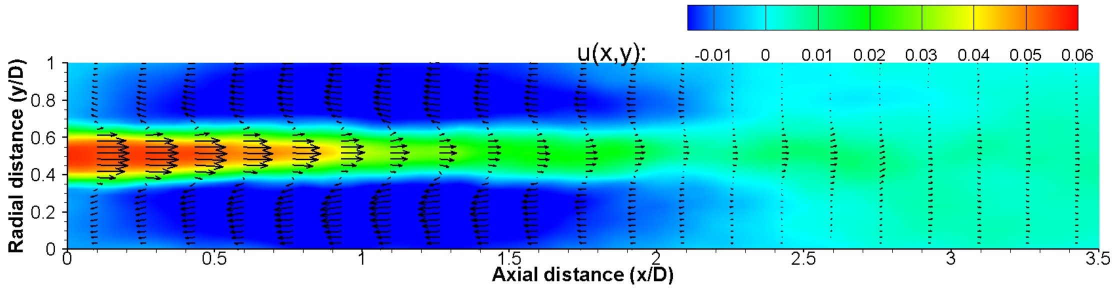

(c) Mode-0 + Mode-2

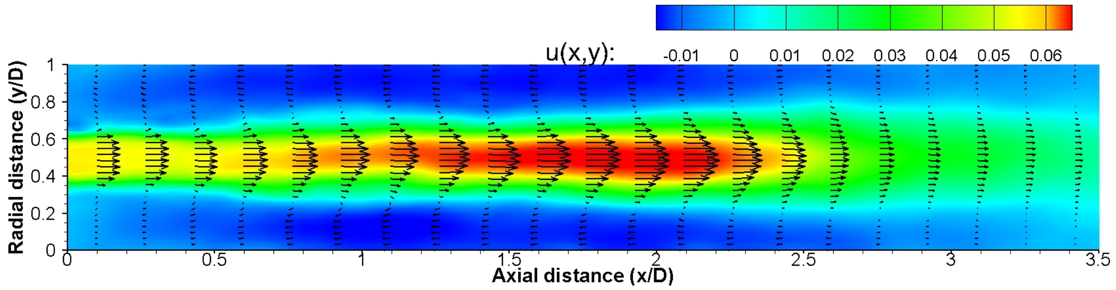

(d) Mode-0 + Mode-3

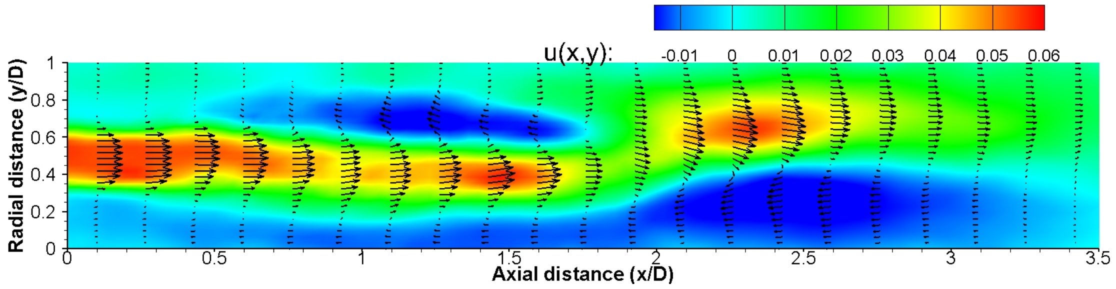

(e) Mode-0 + Mode-4

Figure 7.18: Figures illustrating the effect of the mode on the mean flow field. Each normalized mode is added to the normalized mean. The contours show the normalized axial-velocity magnitude $u(x, y)$. Note, these contours are not physical and are used only to assist in the interpretation of the modes.

7.6.2 Multiple-hole orifice

Following the approach presented earlier for the single hole orifice, the POD modes for a flow at 1 m/sec ($Re_P = 8350$) through a multiple-hole orifice PIV-M1 ($\beta = 19\%, t/d_h = 1.07$), are described in this section. The convergence of the eigen values was tested (see figure 7.19) and a data size of 600 snapshots, with a time separation of $5/1500$ s between each snapshot is selected.

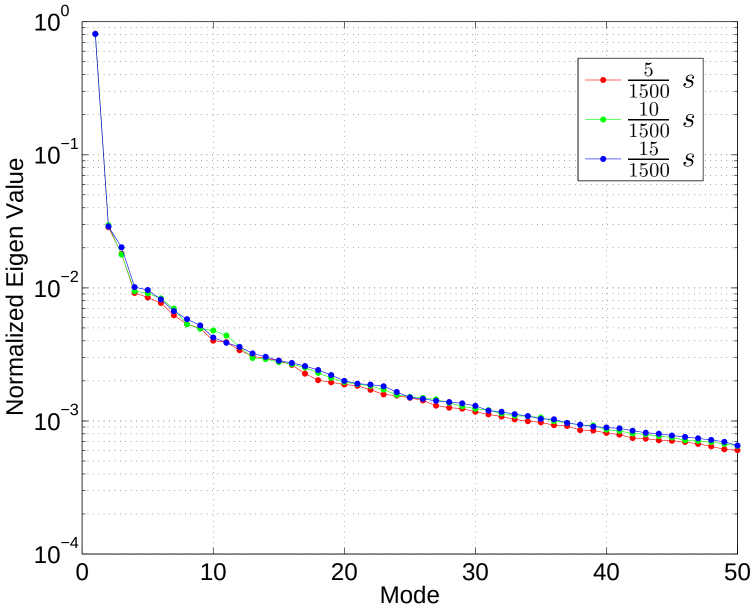

Figure 7.19: Normalized eigen-values of the modes computed using three different time-separations namely, $\{5/1500, 10/1500, 15/1500\}$ s for a multiple hole orifice. Note, the first mode shown here is the mean-flow as the contribution of the mean has not been subtracted from the snapshots.

The contribution of the mean-flow is subtracted from each snapshot and the algorithm to compute the POD modes is implemented. Figure 7.20 presents the relative energy contribution of the first 50 modes.

Interpretation of POD modes

Figure 7.21 presents the first two POD spatial modes, along with their energy contribution to the velocity fluctuations. Similar to the single hole orifice, the effect of the mode on the mean flow is visualized (see figure 7.22) to assist the interpretation of these modes.

The first two modes contribute about 28% of the total velocity fluctuations in the flow. On comparing them (see figure 7.21a and 7.21b) it appears that these two modes are complementary to each other. By observing the effect of these modes on the mean (see figure 7.22b and 7.22c), it can be established that these two modes represent a lateral swaying of the merged orifice jets, which is quite noticeable through visual inspection of the vector field time series (also see section 8.2.2). It also appears that these POD modes each represent the suppression of one of the off-axis jets.

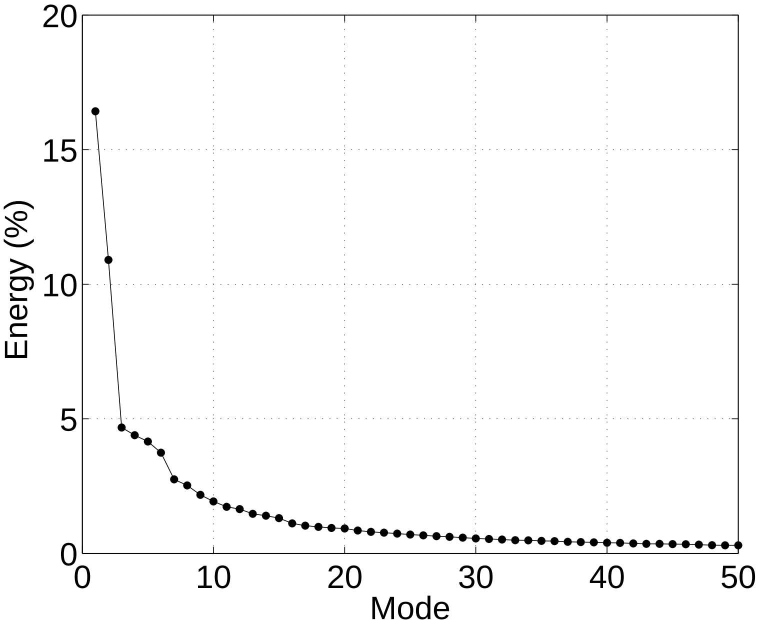

Figure 7.20: Eigenvalues of the first 50 modes shown as a percentage of the total energy of the fluctuating velocity field. Note, the contribution of the mean flow has been subtracted.

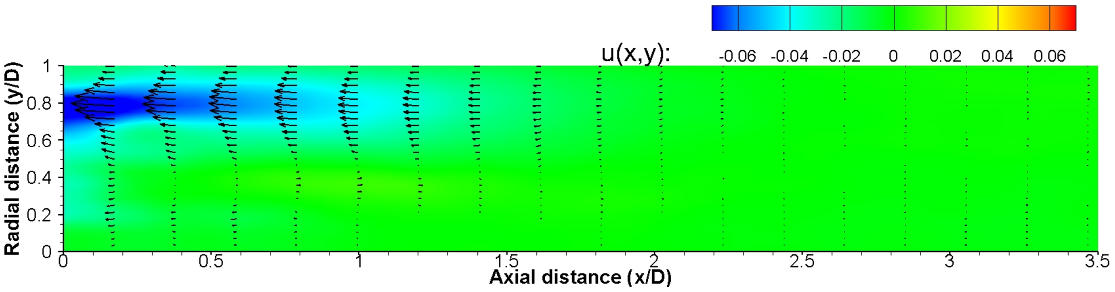

(a) Mode 1, Energy-16.43%

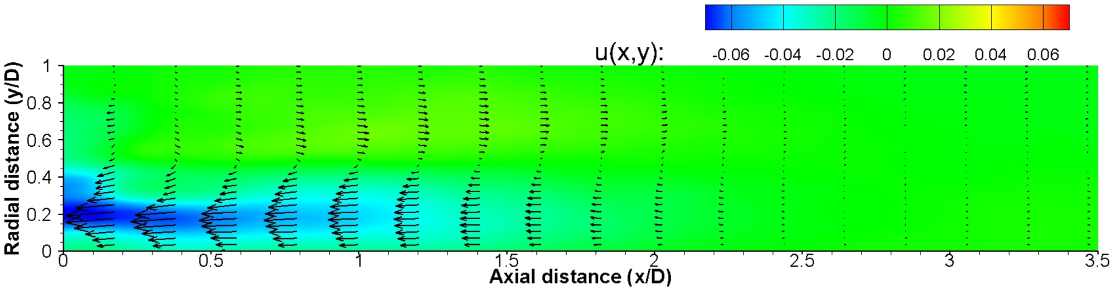

(b) Mode 2, Energy-10.9%

Figure 7.21: Modes 1 and 2 and their corresponding energy contribution. The contours show the normalized axial-velocity magnitude $u(x, y)$. Flow enters the 7-hole multiple-hole orifice PIV-M1 ($\beta = 19\%, t/d_h = 1.07$) at $1\ m/sec$ ($Re_P = 8350$).

The interpretation of higher modes become more difficult as the the size of the flow structures they represent become smaller. Thus, in the current section, the discussion is confined to the first two modes.

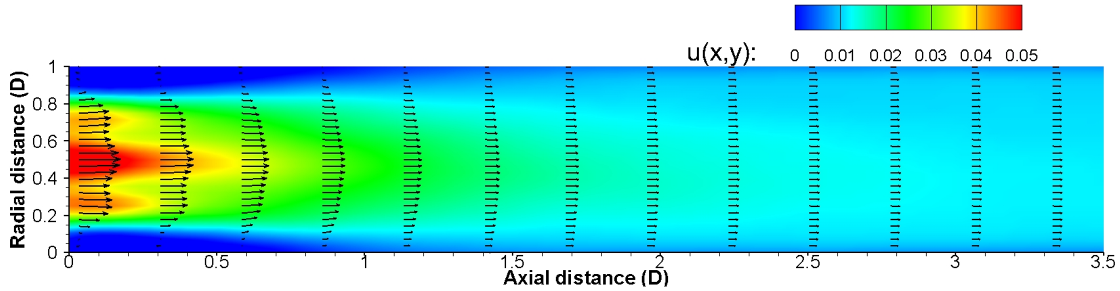

(a) Mode-0, mean flow

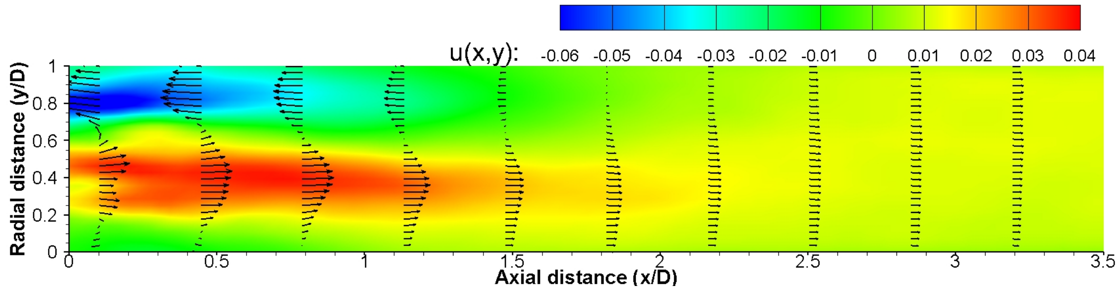

(b) Mode-0 + Mode-1

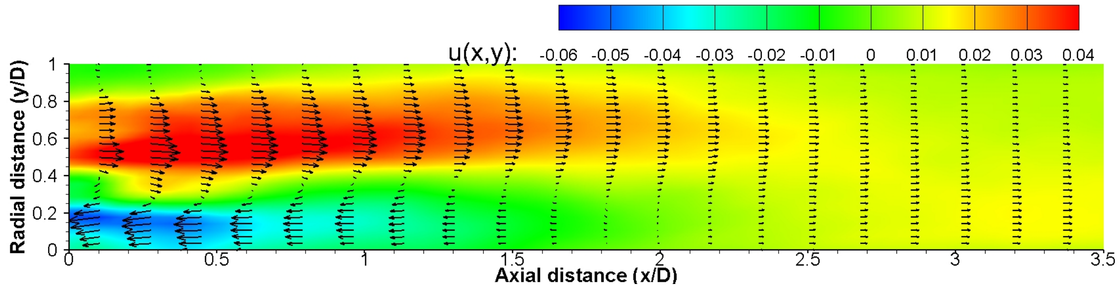

(c) Mode-0 + Mode-2

Figure 7.22: Figures illustrating the effect of the mode on the mean flow field. Each normalized mode is added to the normalized mean. The contours show the normalized axial-velocity magnitude $u(x, y)$. Note, these contours are not physical and are used to assist the interpretation of the modes shown in figure 7.21.

7.7 Conclusion

This chapter discussed results from PIV measurements on single and multiple-hole orifice plates. The instantaneous and mean characteristics of the flow through single hole orifices was presented. The results indicate that the velocity fluctuations are the highest in regions where the two shear layers interact with each other, in the upstream vicinity of the mean reattachment point.

Results from the multiple hole orifice tested showed that the RMS of the velocity fluctuations are the highest in regions very close to the orifice. This was consistent with the behaviour of P'_{rms} obtained from pressure measurements in chapter 5.

The mean reattachment point of the flow through single and multiple hole orifices were quantified and for a given orifice plate, were found to remain fairly independent of the Reynolds number. It was observed that for the single-hole orifice plates that were discussed, the mean reattachment point occurred at about 6-8 equivalent step-heights $(0.5 \times (D_p - d_h))$ from the orifice.

Proper orthogonal decomposition was implemented to extract the most dominant flow structures present in the flow. It was observed that for the single hole orifice (section 7.6.1), the first POD-mode is indicative of a flapping motion of the orifice jet. The frequency associated with this phenomenon forms a central part of the discussion in chapter 8. The subsequent modes, 2 and 3, represent modulations of the jet flow along the axial direction.

The first two POD modes of the multiple hole orifice (section 7.6.2), that contribute to about 28% of the total fluctuations, indicate a suppression of each of the off-axis jets which also appears as a lateral swaying of the merged orifice jets.

Chapter 8

Results: Unsteady flow characteristics

8.1 Introduction

Results from pressure and PIV measurements were discussed independently in chapters 5 and 7. This chapter consolidates[1] observations from the two experimental approaches.

The first section presents some features of the flow that are noticeable through a visual inspection of a continuous velocity vector series. These are presented for both the single and multiple hole orifice. The experimental techniques used in the present investigations performed time resolved measurements that capture the unsteady features of the flow. The latter sections of this chapter are dedicated to understanding some of these time-varying characteristics.

8.2 Flow features

The evolution and dynamics of the orifice jet can be visualized by the vector fields resulting from the single-frame time-series. Though these characteristics are clearer while observing a time series in the form of a video, in this section, some features of the unsteady flow field will be described with the aid of instantaneous velocity fields.

8.2.1 Single hole orifice

Figure 8.1 illustrates the complex and unsteady nature of the orifice jet, using 8 instantaneous vector fields each separated by 20 images.

---

[1] A comparison is made between single-hole orifices of the same geometrical properties, which were used in both PIV and pressure measurements. These are S2 and PIV-S2, S3 and PIV-S3 and lastly, S4 and PIV-S4.

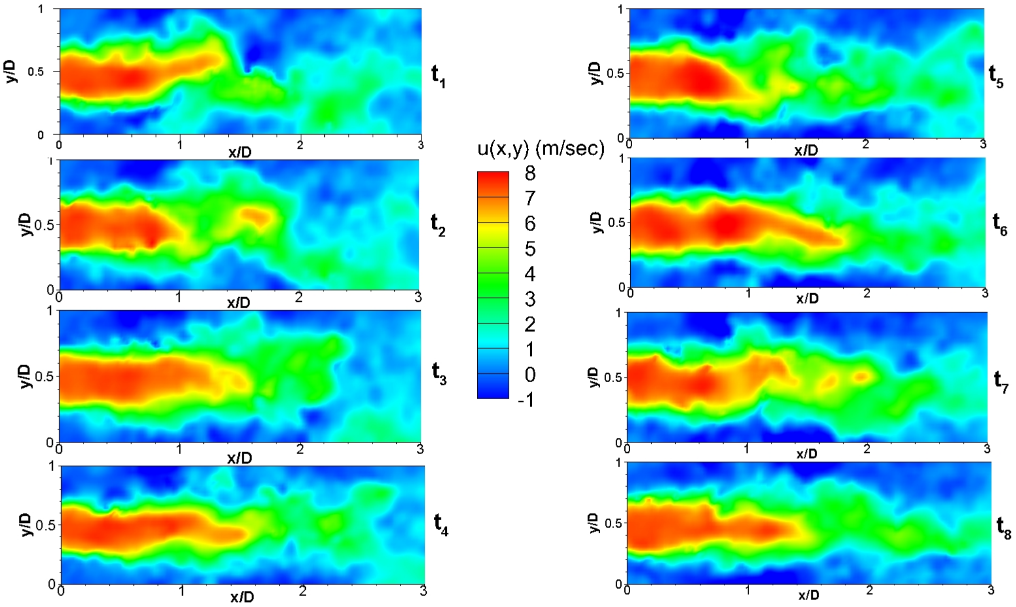

Figure 8.1: Figures illustrating the unsteady flow field, downstream of a single hole orifice with $\beta = 20\%, t/d_h = 0.5$. Flow enters the orifice at $1\ m/sec$ ($Re_p = 8383$). Each image corresponds to an instantaneous flow field at a given time instant t_i. The images are arranged from top to bottom (starting on the left) as $\{t_1 t_2 \cdots t_8\}$, with a difference of 20 images between consecutive images. Vector fields computed using sliding sum of correlation with ± 3 images on data sampled at 12500 Hz.

Some of its time varying features can be visualized using these images. For instance, its length varies in time. It appears that the shear layers grow (extend) till a certain extent after which a portion of the fluid breaks-off and the jet length decreases. Another noticeable feature is the constriction of the jet. These images also illustrate the lateral deviations of the jet and its shear layers with respect to the pipe centerline, which appear as a flapping motion in the recorded time-series.

Rockwell and Naudascher (1979) point out that oscillations occur when a shear layer is bounded by a recirculation zone. Maurel et al. (1996) mention that confined jets exhibit well-organized oscillation patterns which are a result of a feedback effect. This feedback refers to the upstream propagation of disturbances from the impingement region to the sensitive area of the free shear layer near separation. Flow oscillations in a confined nozzle jet immersed in a rectangular cavity were also reported by Lawson and Davidson (2001).

The above mentioned instability can be seen using the first POD mode and by observing its effect on the mean flow features. Following the approach of Schrijer et al. (2014), figure 8.2 illustrates a possible mechanism of oscillations that involve the growth and shrinking of the recirculation regions surrounding the orifice jet.

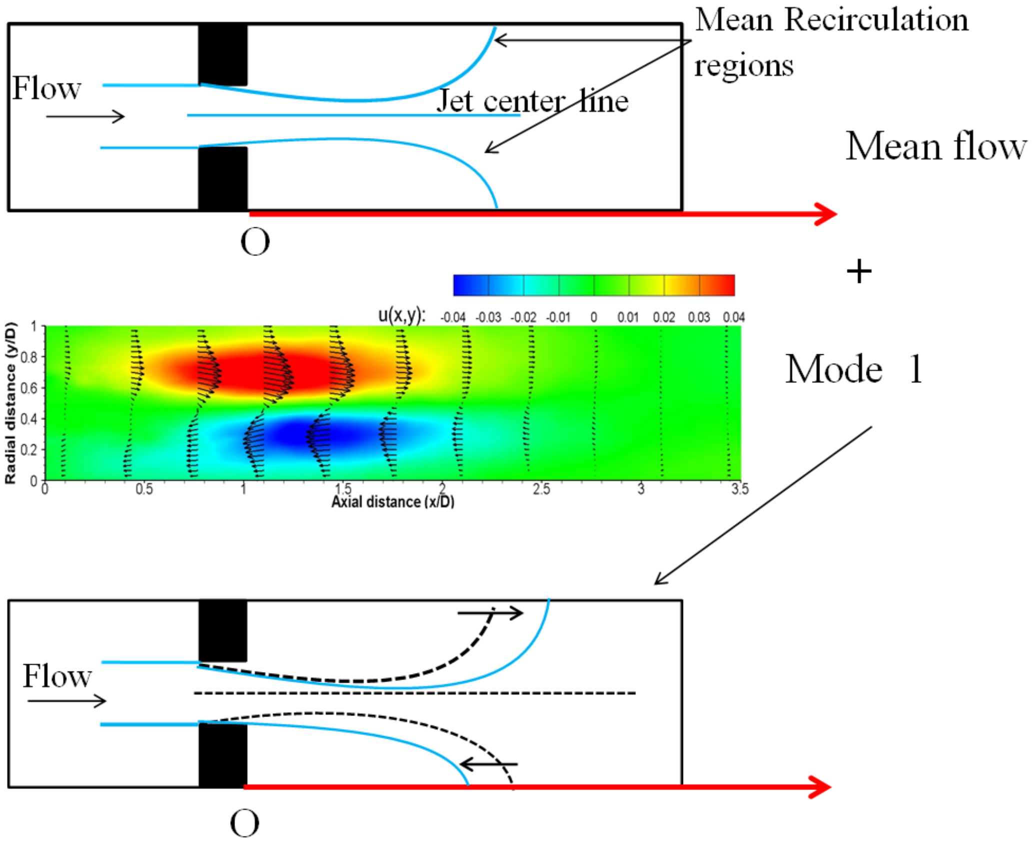

Figure 8.2: Figures illustrating the nature of the first major flow instability that effects the recirculation regions. The top image denote the mean flow features. The first POD mode is shown in the middle. The effect of the mode on the recirculation regions is illustrated in the last figure, where the mean features are shown with dotted lines.

8.2.2 Multiple hole orifice

The nature of the flow at the exit of a multiple-hole orifice is illustrated in figure 8.3. Each of the 8 instantaneous vector fields shown below are separated by 20 images between them.

The multiple hole orifice has the same porosity as the single hole orifice shown in section 8.2.1, though the thickness-ratio and the entrance flow conditions are mildly different. Keeping in mind that the porosity is the most dominant factor that effects the flow through orifices, it appears that the length scales of the flow are considerably diminished as a result of the multiple-holes in the orifice. This is perhaps why the velocity and pressure-fluctuation levels decay faster (see section 7.4.2 and 5.5 respectively).

The mechanism of the multiple separated jets are more difficult to comprehend. A strong interaction between neighbouring jets is observed, with instances where the 3 jets appear to merge within $0.2D$ from the orifice. This interaction is perhaps responsible for the large RMS values in the velocity fluctuations that are observed in regions close to the orifice (see section 7.4.3).

Since the thickness to hole diameter ratio is in the order of 1, the flow may attach within the holes of the orifice. Observing the recorded vector series indicates that this may be occurring intermittently for the present orifice geometry.

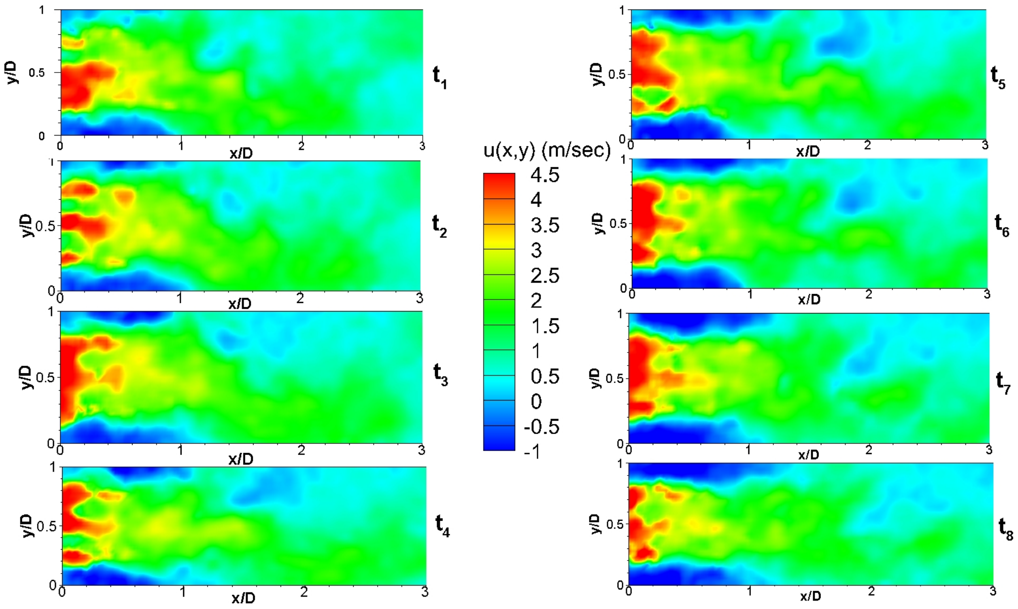

Figure 8.3: Figures illustrating the unsteady flow field, downstream of a 7 hole multiple-hole orifice, with the measurement plane passing through the three central holes (see figure 6.6). Flow enters the orifice ($\beta = 19\%, t/d_h = 1.07$) at $0.75\ m/sec$ ($Re_p = 6287$). Each image corresponds to an instantaneous flow field at a given time instant t_i. The images are arranged from top to bottom (starting on the left) as $\{t_1 t_2 \cdots t_8\}$, with a difference of 20 images between consecutive images. Vector fields computed using sliding sum of correlation using ± 3 images. Data sampled at 12500 Hz.

The remaining section of this chapter will focus on the features of the flow through the single hole orifice.

8.3 Scaling

In situations where oscillations in the flow are present, it is convenient to represent the measured frequency in non-dimensional form using the **Strouhal number** (St) as,

$$St = \frac{f \times L}{U} \tag{8.1}$$

The frequency of oscillations f, are a property of the flow and L and U are suitable length and velocity scales respectively. For a given flow configuration, the Strouhal number is in general a function of the Reynolds number (Batchelor, 2000). The velocity through the orifice jet U_h (using equation 2.3), is a representative scale of the local velocity in the core of the jet and is the velocity-scale used in the results reported here.

The choice for the length-scale however is not trivial. Studies on acoustics of flow through orifice use the plate thickness (Testud et al., 2007; Moussou et al., 2007; Testud et al., 2009). Qing et al. (2006) use the orifice-hole diameter whereas Moussou (2006) proposed using $(D_p - d_h)$. For an orifice, $(D_p - d_h)$ can be regarded as twice the step-height which is a commonly used length scale for backward-facing-step investigations (Kostas et al., 2002). In case of impinging shear-layers leading to self-sustained oscillations, the impingement length (which in the present context is analogous to the mean reattachment length) is regarded as the important length scale (Rockwell & Naudascher, 1979; Maurel et al., 1996).

The motivation for the choice of length scale depends on the flow mechanism to which the frequency of oscillations are associated. In the present case, Strouhal number defined using all the above mentioned length scales are investigated. Note, the average reattachment length (X_r) obtained from the PIV data was presented earlier in table 7.1.

8.4 Spectral analysis

Time-resolved measurements allow analysis of the spectral content of the recorded time series up to the Nyquist frequency. The steps to compute the power-spectral-density were described in section 4.5.

Similar to the pressure-measurements, time-resolved vector fields obtained using PIV can also be used to compute the power-spectral-density. The difference however lies in the fact that each spatial point from the PIV vector-field can be used to construct a time-series. The power-spectral-density of the velocity and POD coefficients are computed using the `pwelch` function available in MATLAB. The power-spectral-density of the wall pressure sensor data are computed using the PAK 5.8 data processing software (see section 4.2.2).

In this section, the pressure and velocity spectra are analysed together. For clarity, a detailed description using one orifice is presented. Corresponding results from other orifices are described, albeit in brief (sections 8.4.2 and 8.4.3). The final section compares results from different orifices (see section 8.4.4).

8.4.1 Single hole orifice with $\beta = 20\%$ and $t/d_h = 0.5$

Figure 8.4 illustrates typical PSD curves computed from the time-series recorded by all six-sensors. The flow enters the orifice at 2 m/sec ($Re_p = 18000$). The following observations can be made from figure 8.4:

- The magnitude of the wall pressure-fluctuations at positions 1D and 2D downstream from the orifice are higher than all other positions. The PSD curves at these two locations, show very similar behavior till about 100 Hz (see figure 8.4a). Beyond this, the 1D curve lies slightly above $2D$ over the entire spectrum.
- A clear peak corresponding to the most energetic frequency is observed at 43.75 Hz at both sensors 1D and 2D. The entire spectrum at these two locations show an increasing trend till about 60 Hz after which they start to decay.
- On moving downstream, the fluctuation levels drop (compare 2D to 3D). By $3D$ the orifice jet is expected to have reattached to the pipe wall.
- Further downstream at $6D$ and $10D$, the PSD of the sensors measure fluctuations associated with boundary layer development as well as the acoustic field (Norton & Bull, 1984).

Effect of Reynolds number

The above analysis of the pressure-spectra showed existence of a dominant frequency observed at 1D. The R.M.S of the pressure-fluctuations discussed earlier in section 5.3.3 showed that the fluctuation levels, reach their maximum value at 1D from the orifice-S3.

The PSD of the pressure fluctuations measured at $1D$ from the orifice, under different flow-conditions are shown in figure 8.5. Each of the curves show a behavior similar to the one discussed above with a distinct peak.

Figure 8.6a presents the variation of the frequency component with the highest energy content measured at sensor $1D$, as a function of the flow speed. Note that this graph has been constructed by running a script that computes the PSD at each flow condition and returns this frequency value.

It is interesting to note that the most dominant frequency component appears to scale linearly with the flow velocity in the current measurement range. This is illustrated in figure 8.6b, which presents these values in non-dimensional form. Note, the Strouhal number has been defined using the length scales discussed earlier (see section 8.3). The hole velocity (U_h), is the velocity scale used in all the definitions.

Next, the velocity spectra are analysed with the aim of determining the flow mechanism that could be accountable for this frequency. Since a flow condition corresponding to $Re_p = 18000$ is not available in the PIV data, the upcoming results are shown at $Re_p = 8383$. At this Reynolds number, the pressure sensor at $1D$ presents a peak at 21 Hz (see figure 8.6b for the St number).

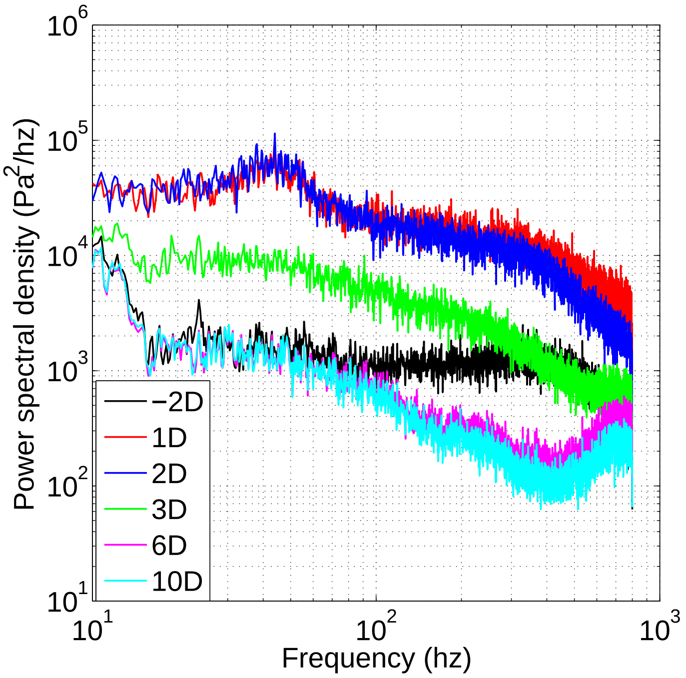

(a) PSD, complete spectrum in logarithmic scale

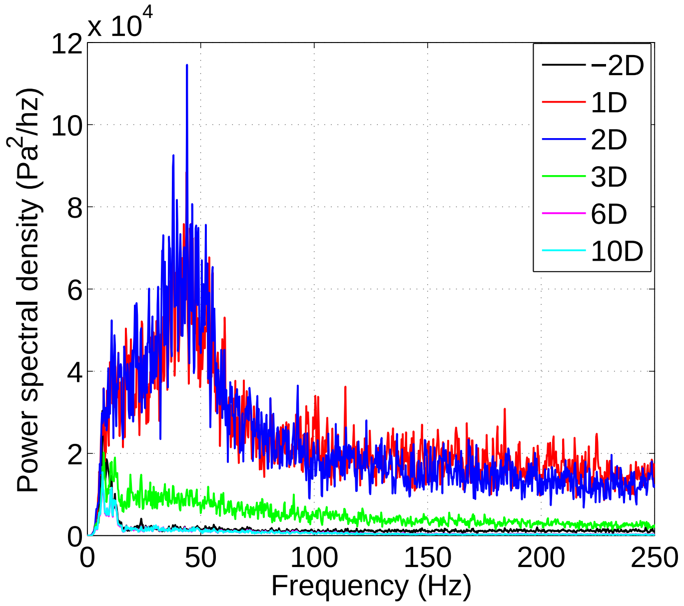

(b) PSD, reduced spectrum in linear scale

Figure 8.4: Power spectral density (PSD) of the pressure-fluctuations as a function of frequency; computed at different axial locations from the orifice. Flow enters orifice S3 ($\beta = 20\%, t/d_h = 0.5$) at $2\ m/sec$ ($Re_p = 18000$). Legend shows sensor positions with respect to the orifice plate.

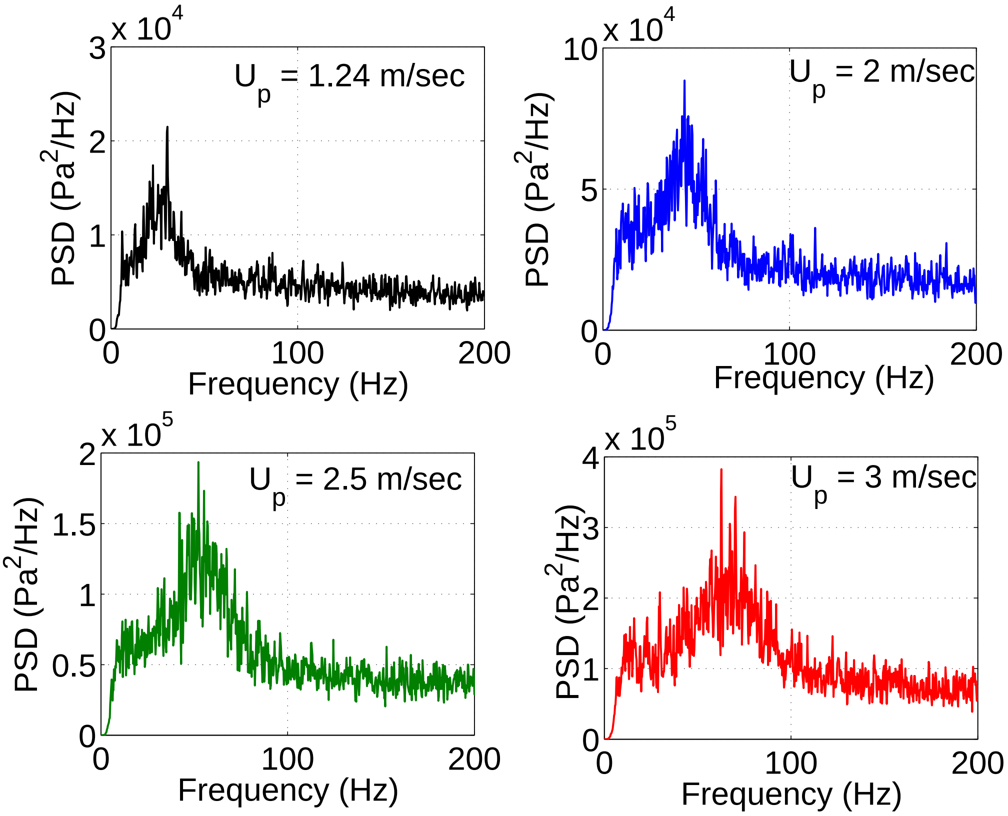

Figure 8.5: PSD of the wall pressure-fluctuations as a function of frequency at the mentioned flow-speeds measured at 1D downstream from the orifice S3 ($\beta = 20\%, t/d_h = 0.5$).

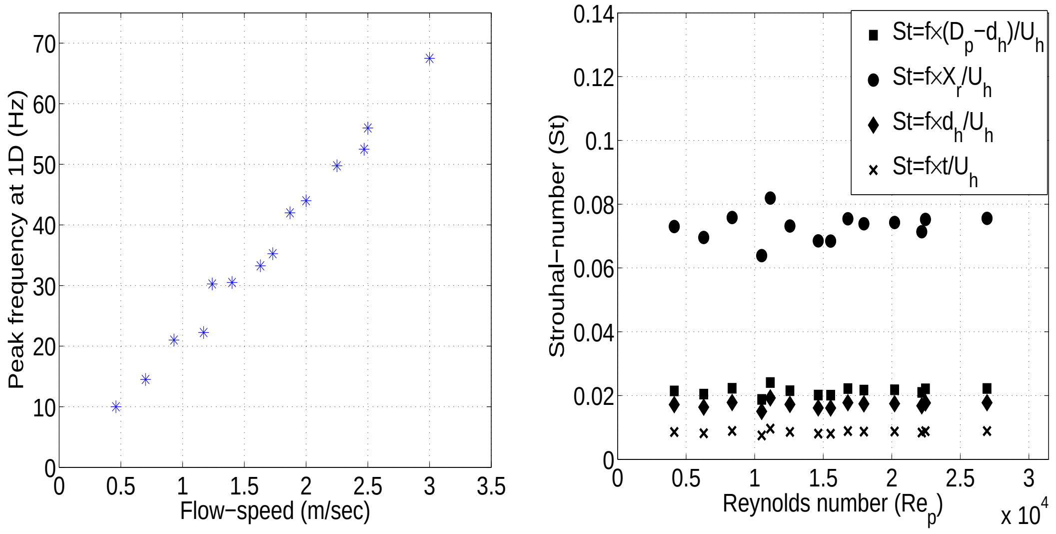

(a) Peak frequency at all flow-conditions tested. **(b)** Peak-frequency in non-dimensional form.

Figure 8.6: Figures illustrating the behaviour of the distinct low-frequency peak measured by the wall pressure-sensor at 1D downstream from the orifice S3 ($\beta = 20\%, t/d_h = 0.5$)

Power-spectral-density: Axial velocity

The wall pressure sensors measured a distinct low-frequency peak. To establish its origins, the PSD of the velocity at several locations are computed.

Figure 8.7 presents the PSD of the axial velocity fluctuations ($u'(x, y)$), computed at several radial positions (y/D) at a distance of $1D$ from the orifice. The flow enters the orifice at 1 m/sec ($Re_p = 8383$). The most dominant frequency appears at 26.37 Hz and is clearly visible in all the sub-figures shown in figure 8.7. These points were selected for comparing the results from the pressure sensor positioned at $1D$ in the pressure-measurements. Note, the peak frequency measured by the pressure-sensor at 1D for analogous flow conditions was 21 Hz[2](see figure 8.6a).

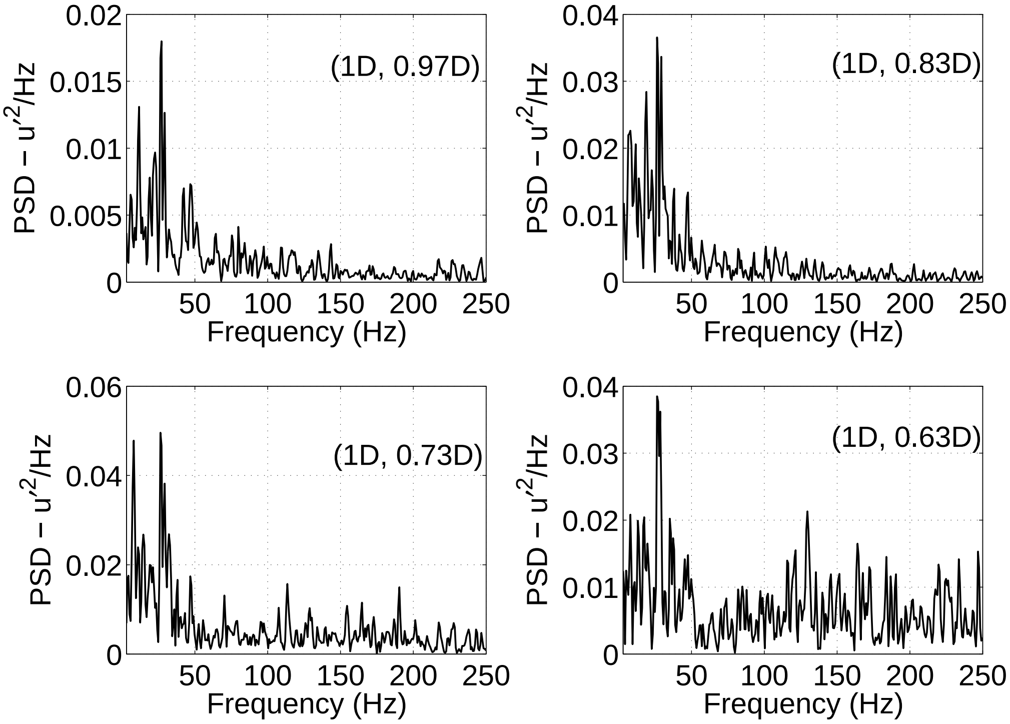

Figure 8.7: PSD of the axial velocity fluctuations ($u'(x, y)$). Each sub-figure corresponds to a different radial position (y), at 1D downstream from the orifice. Flow enters at 1 m/sec ($Re_p = 8383$) through orifice PIV-S3 with $\beta = 20\%$ and $t/d_h = 0.5$.

The above mentioned result motivates the computation of the PSD at several points in the flow field. Figure 8.8 presents the most dominant frequency (obtained using the PSD) as a function of the radial-coordinate (y/D) of the point where it is computed. The calculations are performed at different downstream locations (x/D) which are shown in the legend. The graph is a result of a script which computes the PSD at all points and reports the most energetic frequency at those points.

---

[2] Even though the flow conditions used during both PIV and pressure measurements are similar, minor differences in absolute values of the frequency are expected as the geometries of the setups used are slightly different, see footnote on page 75. A comparison of the non-dimensional frequency or the Strouhal number is presented in figure 8.10.

It is interesting to see that the frequency ($\approx 27\ Hz$) is dominant as far as $3D$ from the orifice. It is primarily discernable at points lying in the recirculation zone surrounding the orifice jet. This result indicates that the phenomenon associated with this frequency is dominant over the entire recirculation region, perhaps indicating its oscillatory behavior. This observation is further analysed using information from POD.

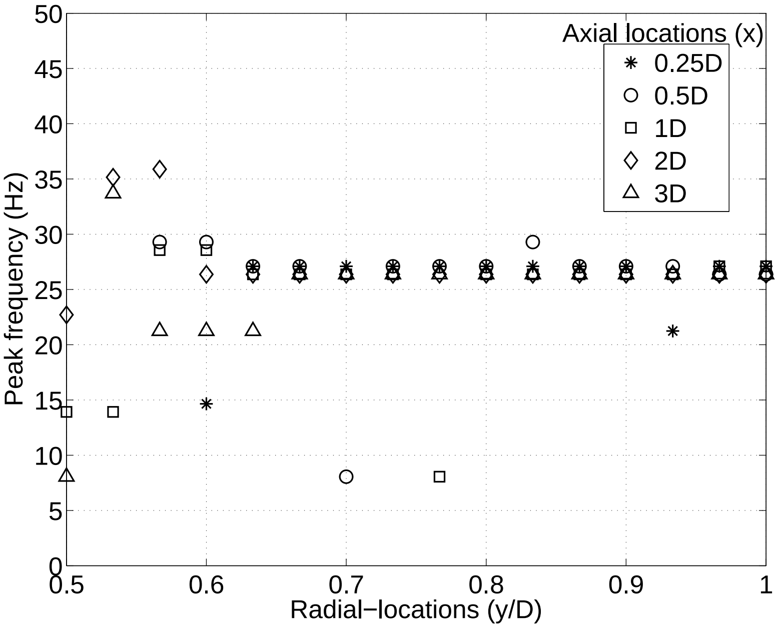

Figure 8.8: Peak frequency extracted from the PSD of the axial velocity fluctuations ($u'(x,y)$) as a function of the spatial co-ordinate of the point. A frequency of $\approx 27\ Hz$ appears over a large region. Flow enters at $1\ m/sec$ ($Re_p = 8383$) through single-hole orifice PIV-S3 with $\beta = 20\%$ and $t/d_h = 0.5$. Pipe centerline is at $y = 0.5D$ and the upper wall at $y = 1D$.

Figure 8.9a presents the first spatial mode for the present flow condition obtained from POD (method description in section 7.6). Notice that this spatial mode is similar to the first mode (see figure 7.16a) presented earlier in section 7.6.1. The temporal information contained in the POD coefficients are transformed to the frequency domain and the resulting temporal mode (*chrono*-mode) is shown in figure 8.9b. In general, each POD mode is associated with several frequencies but in the present case the first *chrono*-mode shows a clear, sharp peak at a frequency of $\approx 27\ Hz$, also obtained earlier from the PSD.

Figure 8.10 presents the low-frequency peak measured using the PIV data in non-dimensional form. It is compared to the results from the pressure-measurements shown earlier (figure 8.6). The values attributed to the PIV data are obtained by analysing the PSD at several radial points (y/D) at a distance of 1 (x/D) from the orifice as well as the first temporal POD mode. At a given Reynolds number, it is clear that the Strouhal number(s) related to the low frequency peak obtained using data from the wall pressure-sensors and the PIV data lie close to each other.

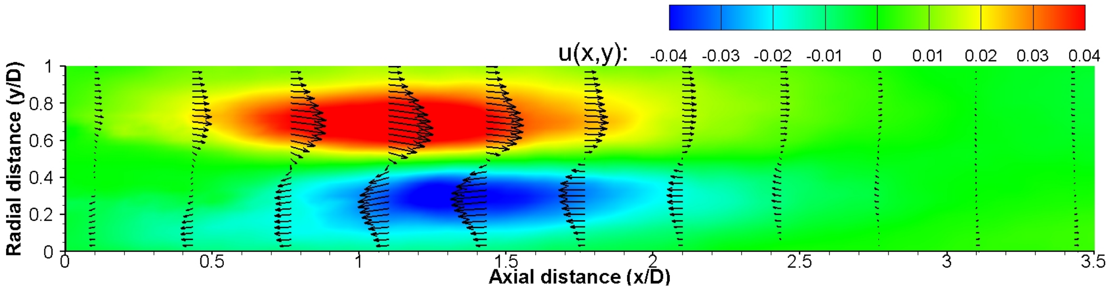

(a) First spatial POD mode showing contours of the normalized axial velocity $u(x,y)$

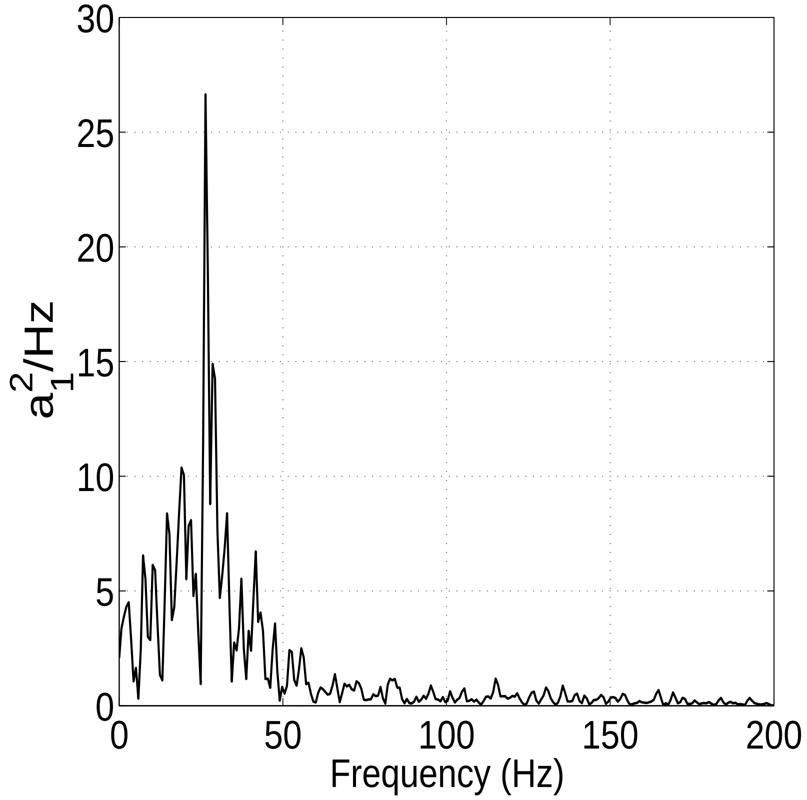

(b) First temporal POD Mode with a distinct peak at $26.37\ Hz$.

Figure 8.9: Figures depicting the first POD spatial mode and the corresponding temporal mode. Computed using a data set of 1000 snapshots with each snapshot separated by $3/1500$ s. Flow enters at $1\ m/sec$ ($Re_p = 8383$) through single-hole orifice PIV-S3 with $\beta = 20\%$ and $t/d_h = 0.5$.

This leads to two important conclusions:

- The results from the PIV and pressure measurements are comparable and support each other.
- The most dominant frequency is a result of the most dominant flow structure (mode-1), which, based on the POD analysis (section 7.6.1) corresponds physically to a flapping motion of the orifice jet.

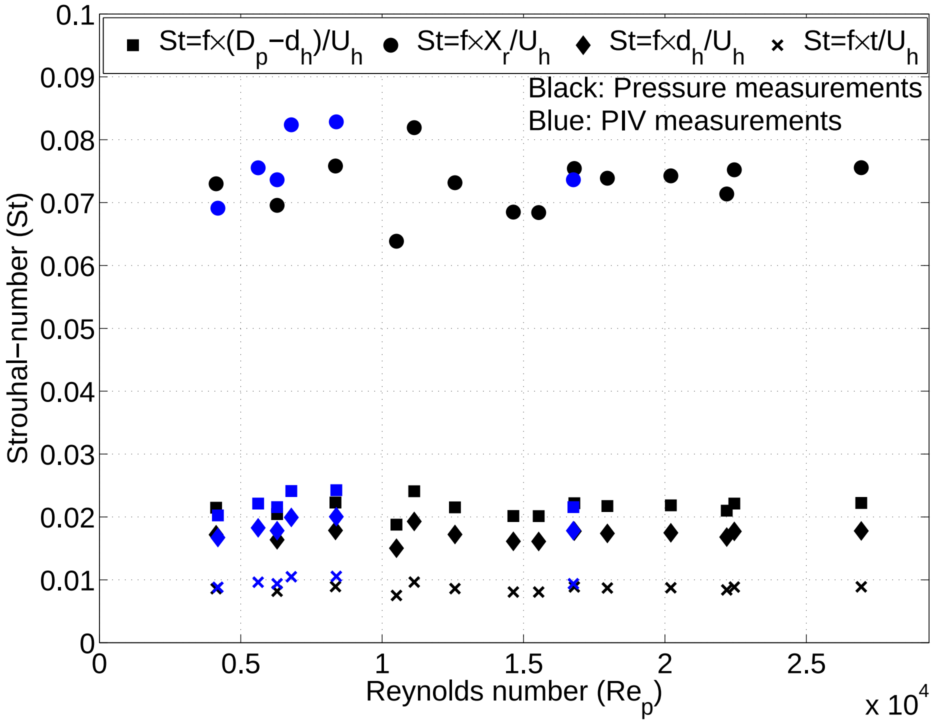

Figure 8.10: Comparison of the Strouhal number corresponding to the low-frequency peak obtained from the PIV data (blue) and data from the wall-pressure sensor at 1D (black). All values are for a single hole orifice with $\beta = 20\%, t/d_h = 0.5$.

It is worth mentioning that data from the wall pressure sensors are more favourable for power-spectral-density computations. The large number of measurement points allow using advanced signal processing techniques (see section 4.5) that minimize noise. Though the present PIV measurements have limited number of samples in time, the availability of information over the entire flow domain is a major advantage over the point-wise pressure data. Furthermore, it allows using advanced data analysis techniques like POD.

8.4.2 Single hole orifice with $\beta = 11\%$ and $t/d_h = 0.5$

The steps described in the previous section have been repeated for the single hole orifice with $\beta = 11\%$ and $t/d_h = 0.5$. For the present case, the magnitude of the pressure fluctuations (and $P'_{rms}/0.5\rho U_p^2$) were highest at 2D from the orifice (see figure 5.6a). Thus, the pressure and velocity spectra are analysed at a distance of $2D$ downstream from the orifice.

On analysing the PSD of the wall pressure fluctuations and axial velocity, distinct peaks similar to those described in the previous section were identified. However, in many of the flow cases these peaks are not clearly recognizable. Thus, only those flow conditions in which the fluctuating pressure PSD curves show a clear and identifiable peak are reported below. Figure 8.11 presents the corresponding Strouhal numbers. In addition, the peak frequency measured using PIV data (velocity spectra and 1st temporal mode) are also shown in figure 8.11.

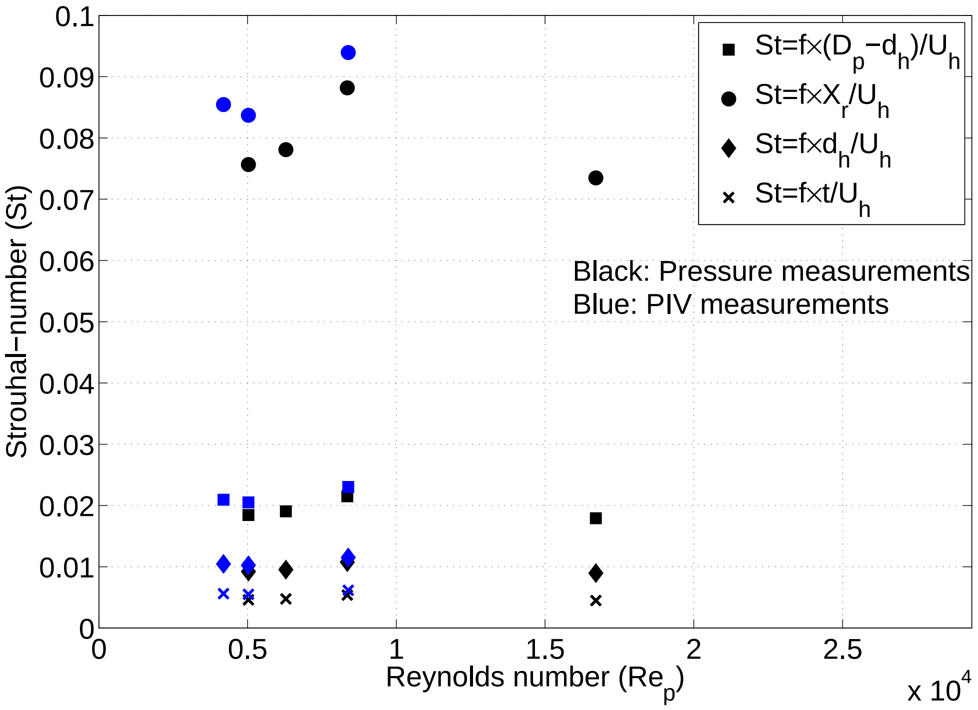

Figure 8.11: Comparison of the Strouhal number corresponding to the low-frequency peak obtained from the PIV data (blue) and data from the wall-pressure sensor at 2D (black). All values are for a single hole orifice with $\beta = 11\%, t/d_h = 0.5$.

8.4.3 Single hole orifice with $\beta = 30\%$ and $t/d_h = 0.5$

A similar analysis is performed on the single hole orifice with $\beta = 30\%$ and $t/d_h = 0.5$. On analysing the wall pressure PSD, distinct peaks (similar to figure 8.4b) were again identified.

Figure 8.12a presents this low frequency peak measured by the wall pressure sensor at 1D for all the flow conditions tested and figure 8.12b presents them in non-dimensional form. Similar to the orifice discussed in section 8.4.1, the magnitude of the frequency increases with the flow speed.

The PSD computed from the wall pressure sensor data at 1D show a clear and identifiable peak (similar to figure 8.5) however, information from the PIV data are inconclusive. For example, figure 8.13 presents the first spatial and temporal mode. Note that the spatial mode which is indicative of the flapping jet, is similar to the one discussed earlier in figure 8.9a. However, the temporal mode does not present a clear peak, like seen in figure 8.9b. The velocity power-spectral-density also show similar characteristics. Thus, for this orifice, only results from the wall pressure sensors are shown in figure 8.12.

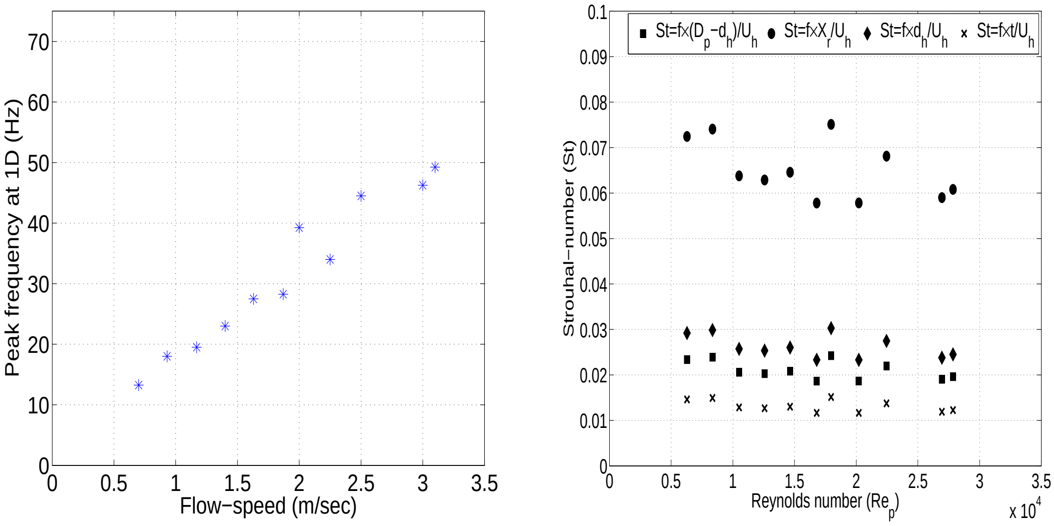

(a) Peak frequency at all flow-conditions tested. **(b)** Peak-frequency in non-dimensional form.

Figure 8.12: Figures illustrating the behaviour of the distinct low-frequency peak measured by the wall pressure-sensor at 1D downstream from orifice S4 ($\beta = 30\%, t/d_h = 0.5$); (left) as a function of the flow-speed, (right) in non-dimensional form using different length-scales for the Strouhal number.

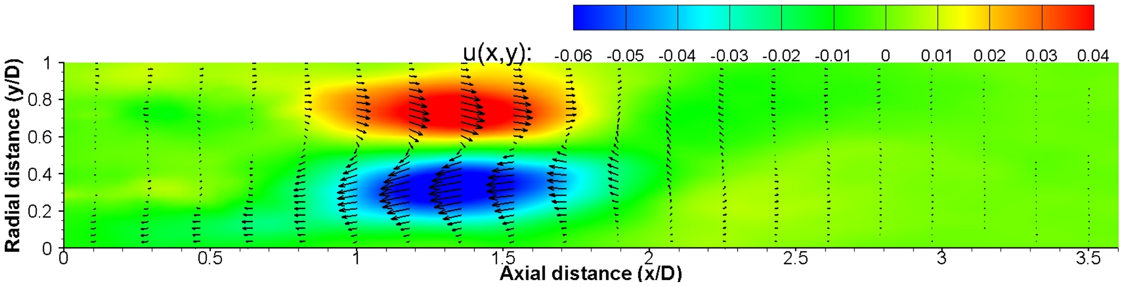

(a) First spatial POD mode showing contours of the normalized axial velocity $u(x, y)$

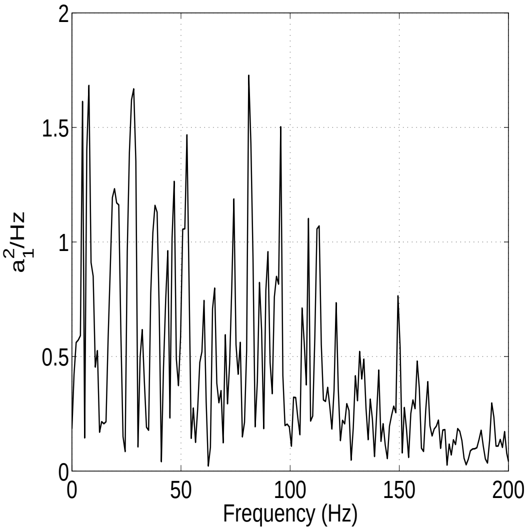

(b) First temporal POD Mode, with no clear distinguishable peak.

Figure 8.13: Figures depicting the first POD spatial mode and the PSD of the POD coefficients. Computed using a data set of 1000 snapshots with each snapshot separated by $3/1500\ s$. Flow enters at $1\ m/sec$ ($Re_p = 8383$) through single-hole orifice PIV-S4 with $\beta = 30\%$ and $t/d_h = 0.5$.

8.4.4 Comparison of orifices: Choice of length scale

On comparing figures 8.12, 8.11 and 8.10, it appears that the flapping frequency presents similarities in its behaviour over different orifice geometries. In order to identify this, it is imperative that a suitable length scale for the Strouhal number be determined. As discussed earlier in section 8.3, several candidates exist.

The results discussed in the previous sections for different orifices are now presented together in figure 8.14 and 8.15. For clarity, only results from the wall pressure sensor measurements are shown. Note that the Strouhal number based on the hole diameter has been dropped as it clearly showed large variations from one orifice to the other. In the figure, symbols are used to differentiate length scales and colours are used to differentiate orifices. All the single-hole orifices have different porosities (β) but have the same thickness ratio (t/d_h).

The Strouhal number based on ($D_p - d_h$) seems to show the least variations between different orifices. The plate thickness (t) works as a suitable length scale for acoustic phenomenon, like the whistling of orifices (see section 5.3.3). However, in the present situation it doesn't lead to a collapse of different measurement values.

Table 8.1 presents the mean Strouhal number $\bar{St}$, for each orifice individually with the last column specifying that for all the orifices (using points shown in figures 8.14 and 8.15). The relative variation is defined as the ratio of the RMS to the mean. Note that for a given orifice, the relative variation using different length scales is the same and this is shown in the last row of the table (σ_o).

On observing all the orifices tested, it appears that the relative variation in the Strouhal number based on ($D_p - d_h$) is the least (8.25%), closely followed by that based on the mean reattachment length (10.01%).

Parameter	S2	S3	S4	ALL
$\bar{St}_{Xr}$	0.079	0.073	0.065	0.071 $\sigma_{St} = 10.01\%$
$\bar{St}_t$	0.0048	0.0085	0.0131	0.010 $\sigma_{St} = 31.36\%$
$\bar{St}_{(d_p-d_h)}$	0.0192	0.0214	0.0210	0.021 $\sigma_{St} = 8.25\%$
σ_o	7.13%	5.75%	9.3%	

Table 8.1: Mean Strouhal numbers $\bar{St}$ with the subscript denoting the length scale. Each column of the table represents an individual orifice with the last column for all the orifices. The σ_{St} value shown in the last column denotes the relative variation (R.M.S/mean) of that Strouhal number definition. The last row denotes the relative variation of the Strouhal number of individual orifices.

It is important to note that these results are for a constant thickness ratio ($t/d_h = 0.5$). As discussed earlier, the t/d_h ratio influences the nature of the flow inside the orifice. The present results do not quantify its effect. That being said, it is interesting to note that for a given t/d_h, the non-dimensional flapping frequency based on $(D_p - d_h)$ remains close to $St \approx 0.02$ for different plate porosities in the range of Reynolds number that were investigated.

As a final remark, it is noticed that the Strouhal numbers that are seen here (in terms of order of magnitude) are similar to those reported for turbulent flows over a backward facing step. For instance Heenan and Morrison (1998) report the non-dimensional flapping frequency based on the reattachment length for the backward facing step appearing close to 0.1 and Spazzini et al. (2001) report the same at $St < 0.1$ while mentioning that it seemed to approach 0.1 at higher Reynolds number.

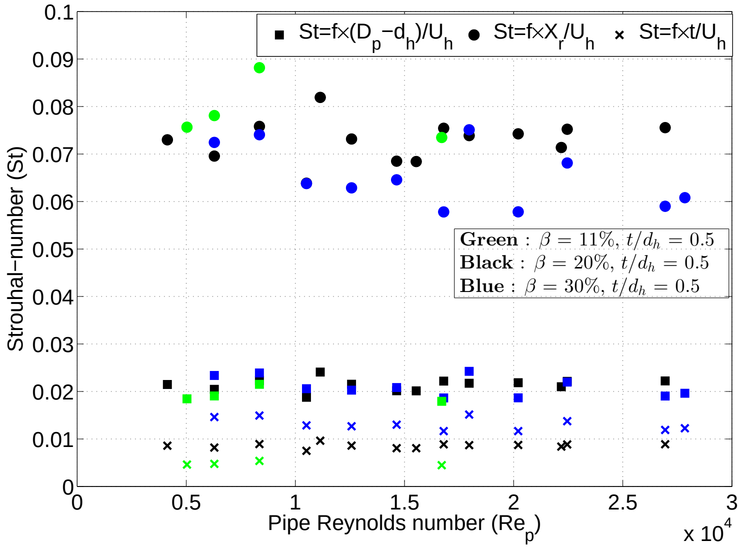

Figure 8.14: Comparison of different Strouhal numbers as a function of pipe Reynolds-number (Re_p), corresponding to the low-frequency peak using data from the wall-pressure sensors. The symbols used are for different length scales, square-$(D_p - d_h)$, circle-X_r and cross-t. The colours differentiate the orifices, green-$\beta = 11\%$, black-$\beta = 20\%$ and blue-$\beta = 30\%$. All data are for single hole orifices with $t/d_h = 0.5$.

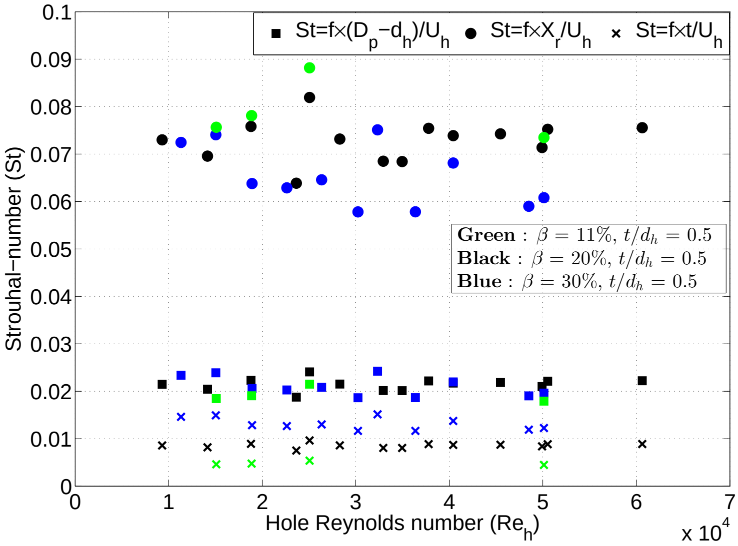

Figure 8.15: Comparison of different Strouhal numbers as a function of hole Reynolds-number (Re_h), corresponding to the low-frequency peak using data from the wall-pressure sensors. The symbols used are for different length scales, square-($D_p - d_h$), circle-X_r and cross-t. The colours differentiate the orifices, green-$\beta = 11\%$, black-$\beta = 20\%$ and blue-$\beta = 30\%$. All data are for single hole orifices with $t/d_h = 0.5$.

8.5 Conclusion

This chapter described the unsteady characteristics exhibited by the flow issuing through an orifice. Some features of the flow were discussed using instantaneous vector fields in section 8.2.

The power spectral density of the wall pressure fluctuations indicated the presence of a low frequency flow phenomenon whose frequency increased with increasing flow speed. This low frequency was also observed in the velocity spectra and the first temporal POD mode obtained from the PIV measurements. It was concluded that the results from PIV and pressure measurements support each other.

The comparison of the PIV and pressure measurements leads to the conclusion that the orifice jet exhibits a low frequency flapping motion, sustained by the recirculation region. Among the orifice plates tested, the non-dimensional frequency based on the hole velocity and $(D_p - d_h)$ was found to be $St \approx 0.02$ or by using the reattachment length (X_r), $St \approx 0.07$. The effect of t/d_h on this frequency was not reported in this chapter.

Chapter 9

Conclusion & scope for future work

9.1 Introduction

As closing remarks, this chapter summarizes some conclusions that were drawn from the results of the present investigations. The final section proposes additional work that could aid in the understanding of flows through orifices.

9.2 Summary of observations

Discussed below, are some conclusions that were drawn from the present study. These observations are based on data and results from the measurements described in this document at flow conditions outlined in chapters 4 and 6. Section 3.4 of chapter 3 highlighted some research questions motivating the present study.

- Turbulent flow of water through a sharp-edged, thin, single-hole orifice contained in a pipe results in a strong unsteady jet (section 8.2.1 and 7.3). It is surrounded by large recirculation regions (section 7.3.2) whose extent is a function of the orifice geometry (section 7.5).
- The variation of the orifice pressure loss coefficient as a function of its geometrical properties and flow conditions were discussed in section 5.3 and 5.4. It was observed that the loss coefficient of the majority of the orifices tested belonged to the non-cavitating, self-similar region and the results obtained here matched fairly well with those reported in literature.
- Despite having significantly different flow features (see section 8.2), single-hole and multiple-hole orifices having the same porosity β, and thickness to hole diameter ratio can achieve comparable pressure losses (section 5.5).
- A cavitating single-hole orifice emanated whistling sounds whose frequency was found to occur at $St \approx 0.2$ (section 5.3.3).

- The pressure fluctuations occurring in the flow downstream of orifices (both single and multiple-hole) were found to scale with the square of the incoming flow speed. The location of the peak fluctuation levels are a function of the orifice geometry and for the present measurement conditions were within $0 - 2D$ from the orifice.

- For a single-hole orifice, a comparison of PIV and pressure measurements showed that the peak velocity and pressure fluctuations occur in the upstream vicinity of the point of reattachment, in regions where the shear layers of the orifice jet interact with each other (section 7.3.3). For a multiple hole orifice, the flow fluctuations were higher much closer to the orifice exit ($x \leq 1D$).

- The decay in the pressure fluctuation levels in the flow downstream of multiple hole orifices was observed to be over a much shorter distance compared to an equivalent single hole orifice, even though the peak pressure fluctuation levels incurred could be similar (section 5.5). This is perhaps due to a reduction in the size of fluid scales that are associated with the former (see sections 8.2.2 and 7.4.3).

- The mean reattachment length of the separated flow through a single-hole orifice was observed to be rather insensitive to Reynolds number and was within $6 - 8$ equivalent step heights ($0.5 \times (D_p - d_h)$) for the orifices tested. In that sense, the flow is analogous to a turbulent flow past a planar backward-facing step and axisymmetric pipe expansions. This distance can be used as a basis to estimate the position of a downstream orifice while using a multi-stage orifice system.

- The velocity and fluctuating pressure PSD showed indications of a dominant low frequency. The POD analysis showed that this frequency corresponds to a flapping motion of the orifice jet which is sustained by the surrounding recirculation regions (section 7.6). For the orifices tested, the non-dimensional flapping frequency based on the hole velocity U_h and $(D_p - d_h)$ was found to be $St \approx 0.02$ or based on the reattachment length (X_r) as $St \approx 0.075$ (section 8.4). The effect of t/d_h on this frequency was not ascertained.

9.3 Scope for future work

The measurement campaigns part of the present project acquired large amounts of data with still room for further analysis. For instance, the application of dynamic-mode-decomposition (Schmid, 2010) on the time-resolved velocity fields could yield additional information about the frequency associated with different flow structures.

Though the present study focussed on the hydrodynamic disturbances in the flow, data from the present pressure measurements can be analysed using the multiple-microphone-method to further understand the behaviour of acoustic field (Jones & Parrott, 1989). Norton and Bull (1984) mention that at large distances downstream of a disturbance in a pipe ($> 20D$), the flow returns to the undisturbed fluid dynamic state of fully developed turbulent pipe flow but has superimposed on it an acoustic field.

The successful application of planar-PIV to the current case substantiates the application of a three-dimensional, Tomographic-PIV measurement (Elsinga et al., 2006).

Tomographic-PIV has shown promising results for a wide range of flow cases (Scarano, 2013b) with recent developments that also allow the generation of instantaneous pressure fields from the three-dimensional velocity fields (Van Oudheusden, 2013).

Measurement of forces exerted on the structure by the flow would be the next step in verifying the added value of using multiple-hole orifices as a replacement for single-hole orifices.

A numerical validation of the present experimental data motivates similar CFD studies (for example Ahuja et al. (2013)) that will aid the understanding of the complex nature of separated flows issuing through orifices.

References

Adams, E., & Johnston, J. P. (1988). Effects of the separating shear layer on the reattachment flow structure. *Experiments in Fluids*, *6*, 493-499.

Adrian, R., & Westerweel, J. (2011). *Particle Image Velocimetry.* Cambridge University Press.

Ahuja, V., Hosangadi, A., Hitt, M., & Lineberry, D. (2013). Numerical Simulations of Instabilities in Single-Hole Orifice Elements. In 49^{th} *aiaa/asme/sae/asee joint propulsion conference.*

Armaly, B., Durst, F., Pereira, J., & Schonung, B. (1983). Experimental and theoretical investigation of backward-facing step flow. *Journal of Fluid Mechanics*, *127*, 473-496.

Batchelor, G. (2000). *An Introduction to Fluid Dynamics.* Cambridge University Press.

Blevins, R. (1984). *Applied Fluid Dynamics Handbook.* Van Nostrand Reinhold Company, New York.

Bruun, H. (1995). *Hot-Wire Anemometry: Principles and Signal Analysis.* Oxford University Press.

Budwig, R. (1994). Refractive index matching methods for liquid flow investigations. *Experiments in Fluids*, *17*, 350-355.

Cengel, Y., & Cimbala, J. (2006). *Fluid mechanics- fundamentals and applications.* McGraw-Hill.

Davidson, P. (2004). *Turbulence : An Introduction for Scientists and Engineers.* Oxford University Press.

Elsinga, G. E., Scarano, F., Wieneke, B., & van Oudheusden, B. W. (2006). Tomographic particle image velocimetry. *Experiments in Fluids*, *41*, 933-947.

Erdal, A. (1997). A numerical investigation of different parameters that affect the performance of a flow conditioner. *Flow Measurement and Instrumentation*, *8*, 93-102.

Frattolillo, A., & Massarotti, N. (2002). Flow conditioners efficiency a comparison based on numerical approach. *Flow Measurement and Instrumentation*, *13*, 1-11.

Haimin, W., Shujuan, X., Qingyi, S., Caimin, Z., Hao, L., & Eryun, C. (2013). Experiment study on pressure drop of a multistage letdownorifice tube. *Nuclear Engineering and Design*, *265*, 633-638.

Heenan, A., & Morrison, J. (1998). Passive Control of Pressure Fluctuations Generated by Separated Flow. *AIAA Journal*, *36*, 1014-1022.

Howes, B., & Greenfield, D. (2002). Guidelines in pulsation studies for reciprocating compressors. In *4th international pipeline conference.*

Idelchik, I. (2008). *Handbook of hydraulic resistance* (4^{th} ed.). Begell House.

Jones, M., & Parrott, T. (1989). Evaluation of a multi-point method for determining acoustic impedence. *Mechanical systems and signal processing*, *3*, 15-35.

Jovic, S., & Driver, D. (1995). Reynolds number effect on the skin friction in separated flows behind a backward-facing step. *Experiments in Fluids*, *18*, 464-467.

Kolodzie, P., & Winkle, M. (1957). Discharge coefficients through perforated plates. *American Institute of Chemical Engineers*, *3*, 305-312.

Kostas, J., Soria, J., & Chong, M. (2002). Particle image velocimetry measurements of a backward-facing step flow. *Experiments in Fluids*, *33*, 838-853.

Kuehn, D. M. (1980). Effects of Adverse Pressure Gradient on the Incompressible Reattaching Flow over a Rearward-Facing Step. *AIAA Journal*, *18*, 343-344.

Kundu, P., Cohen, I., & Dowling, D. (2011). *Fluid Mechanics* (5^{th}, Ed.). Elsevier.

Lacombe, R., Föller, S., Jasor, G., Polifke, W., Aurégan, Y., & Moussou, P. (2013). Identification of aero-acoustic scattering matrices from large eddy simulation: Application to whistling orifices in duct. *Journal of Sound and Vibration.*

Laws, E. (1990). Flow conditioning: A new development. *Flow Measurement and Instrumentation*, *1*.

Laws, E. M., & Ouazzane, A. K. (1994). Compact installations for differential flowmeters. *Flow Measurement and Instrumentation*, *5*, 79-85.

Lawson, N., & Davidson, M. (2001). Self-sustained oscillations of a submerged jet in a thin rectangular cavity. *Journal of Fluids and Structures*, *15*, 59-81.

Le, H., Moin, P., & Kim, J. (1997). Direct numerical simulation of turbulent flow over a backward-facing step. *Journal of Fluid Mechanics*, *330*, 349-374.

Lee, I., & Sung, H. (2001). Characteristics of wall pressure fluctuations in separated and reattaching flows over a backward-facing step. *Experiments in Fluids*, *30*, 262-272.

Lumley, J. (1967). The structure of inhomogeneous turbulent flow. *In Atmospheric Turbulence and Radio Wave Propagation*, 166-178.

Malavasi, S., & Messa, G. (2011). Dissipation and cavitation characteristics of single-hole orifices. *Journal of Fluids Engineering*, *133*.

Malavasi, S., Messa, G., Fratino, U., & Pagano, A. (2012). On the pressure losses through perforated plates. *Flow Measurement and Instrumentation*, *28*, 57-66.

Maurel, A., Ern, P., Zielinska, B. J. A., & Wesfreid, J. E. (1996). Experimental study of self-sustained oscillations in a confined jet. *Physical Review E*, *54*.

Maynes, D., Holt, G. J., & Blotter, J. (2013). Cavitation inception and head loss due to liquid flow through perforated plates of varying thickness. *Journal of Fluids Engineering*, *135*.

Melling, A. (1997). Tracer particles and seeding for Particle Image Velocimetry. *Measurement Science and Technology*, *8*, 1406-1416.

Meyer, K., Pederson, J. M., & Özcan, O. (2007). A turbulent jet in crossflow analysed with proper orthogonal decomposition. *Journal of Fluid Mechanics*, *583*, 197-227.

Mi, J., Kalt, P., Nathan, G., & Wong, C. (2007). PIV measurements of a turbulent jet issuing from round sharp-edged plate. *Experiments in Fluids*, *42*, 625-637.

Miller, D. (1990). *Internal flow systems* (2^{nd} ed.). Miller Innovations.

Moussou, P. (2006). An attempt to scale the vibrations of water pipes. *Journal of pressure vessel technology*, *128*, 670-676.

Moussou, P., Testud, P., Aurégan, Y., & Hirschberg, A. (2007). An acoustic criterion for the whistling of orifices in pipes. *ASME Pressure Vessels and Piping*.

Nicolleau, F., Salim, S., & Nowakowski, A. (2011). Experimental study of a turbulent pipe flow through a fractal plate. *Journal of turbulence*, *12*, 1-20.

Norton, M., & Bull, M. (1984). Mechanism of the generation of external acoustic radiation from pipes due to internal flow disturbances. *Journal of Sound and Vibration*, *94*, 105-146.

Perçin, M., Hu, Y., Oudheusden, B., Remes, B., & Scarano, F. (2011). Wing flexibility effects in clap-and-fling. *International Journal of Micro Air Vehicles*, *3*, 217-227.

Pope, S. (2000). *Turbulent flows.* Cambridge university press.

Qing, M., Jinghui, Z., Yushan, L., Haijun, W., & Quan, D. (2006). Experimental studies of orifice-induced wall pressure fluctuations and pipe vibration. *International Journal of Pressure Vessels and Piping*, *83*, 505-511.

Raffel, M., Willert, C., Wereley, S., & Kompenhans, J. (2007). *Particle image velocimetry: a practical guide* (2^{nd} ed.). Springer.

Reethof, G. (1978). Turbulence generated noise in pipe flow. *Annual Review Fluid Mechanics*, *10*, 333-367.

Rockwell, D., & Naudascher, E. (1979). Self-Sustained Oscillations of Impinging Free Shear Layers. *Annual Review of Fluid Mechanics*, *11*, 67-94.

Scarano, F. (2003). Theory of non-isotropic spatial resolution in PIV. *Experiments in Fluids*, *35*, 268-277.

Scarano, F. (2013a). *Course reader for AE-4180 Flow Measurement Techniques, Faculty of Aerospace Engineering, Delft University of Technology.*

Scarano, F. (2013b). Tomographic PIV: principles and practice. *Measurement Science and Technology*, *24*, 1-28.

Scarano, F., Benocci, C., & Riethmuller, M. L. (1999). Pattern recognition analysis of the turbulent flow past a backward facing step. *Physics of Fluids*, *11*, 3808-3818.

Scarano, F., Bryon, K., & Violato, D. (2010). Time-resolved analysis of circular and chevron jets transition by tomo-PIV. In *15th international symposium on applications of laser techniques to fluid mechanics lisbon, portugal,.*

Schetz, J., & Fuhs, A. (Eds.). (1999). *Fundamentals of fluid mechanics.* Wiley.

Schmid, P. (2010). Dynamic mode decomposition of numerical and experimental data. *Journal of Fluid Mechanics*, *656*, 5-28.

Scholz, P., Reuter, I., & Heitmann, D. (2012). PIV measurements of the flow through an intake port using refractive index matching. In *16th int symp on applications of laser techniques to fluid mechanics lisbon, portugal.*

Schrijer, F., Sciacchitano, A., & Scarano, F. (2014). Spatio-temporal and modal analysis of unsteady fluctuations in a high-subsonic base flow. *Physics of fluids*, *26*.

Schröder, A., Schanz, D., Heine, B., & Dierksheide, U. (2013). Investigation of transitional flow structures downstream of a backward-facing-step by using 2D-2C- and high resolution 3D-3C- Tomo- PIV. *New Results in Numerical and Experimental Fluid Mechanics VIII*, 219-226.

Sciacchitano, A., Scarano, F., & Wieneke, B. (2012). Multi-frame pyramid correlation for time-resolved PIV. *Experiments in Fluids*, *53*, 1087-1105.

Semeraro, O., Bellani, G., & Lundell, F. (2012). Analysis of time-resolved PIV measurements of a confined turbulent jet using POD and Koopman modes. *Experiments in Fluids*, *53*, 1203-1220.

Sirovich, L. (1987). Turbulence and the dynamics of coherent structures. Part I: Coherent structures. *Quarterly of Applied Mathematics*, *45*, 561-571.

Spazzini, P., Iuso, G., Onorato, M., Zurlo, N., & Di Cicca, G. (2001). Unsteady behaviour of back-facing step flow. *Experiments in fluids*, *30*, 551-561.

Spearman, E., Sattary, J., & Reader-Harris, M. (1996). Comparison of velocity and turbulence profiles downstream of perforated plate flow conditioners. *Flow Measurement and Instrumentation*, *7*, 181-199.

Testud, P., Aurégan, Y., Moussou, P., & Hirschberg, A. (2009). The whistling potentiality of an orifice in a confined flow using an energetic criterion. *Journal of Sound and Vibration*, *325*, 769-780.

Testud, P., Moussou, P., Hirschberg, A., & Aurégan, Y. (2007). Noise generated by cavitating single-hole and multi-hole orifices in a water pipe. *Journal of Fluids and Structures*, *23*, 163-189.

Tropea, C., Yarin, A., & Foss, J. (Eds.). (2007). *Handbook of experimental fluid-mechanics.* Springer.

Uzol, O., Chow, Y., Katz, J., & Meneveau, C. (2002). Unobstructed particle image velocimetry measurements within an axial turbo-pump using liquid and blades with matched refractive indices. *Experiments in Fluids*, *33*, 909-919.

van Doorne, C., & Westerweel, J. (2007). Measurement of laminar, transitional and turbulent pipe flow using Stereoscopic-PIV. *Experiments in Fluids*, *42*, 259-279.

Van Oudheusden, B. W. (2013). PIV-based pressure measurement. *Measurement Science and Technology*, *24*.

Van Oudheusden, B. W., Scarano, F., van Hinsberg, N. P., & Watt, D. W. (2005). Phase-resolved characterization of vortex shedding in the near wake of a square-section cylinder at incidence. *Experiments in Fluids*, *39*, 86-98.

Violato, D., & Scarano, F. (2011). Three-dimensional evolution of flow structures in transitional circular and chevron jets. *Physics of fluids*, *23*, 124104-1-25.

Weaver, D. S., Ziada, S., Au-Yang, M. K., Chen, S. S., Païdoussis, M. P., & Pettigrew, M. J. (2000). Flow-induced vibrations in power and process plant components-progress and prospects. *Journal of Pressure Vessel Technology*, *122*, 339-348.

Westerweel, J., Draad, A. A., van der Hoeven, J. G. T., & van Oord, I. (1996). Measurement of fully-developed turbulent pipe flow with digital particle image velocimetry. *Experiments in Fluids*, *20*, 165-177.

Westerweel, J., Elsinga, G., & Adrian, R. (2013). Particle image velocimetry for complex and turbulent flows. *Annual Review of Fluid Mechanics*, *45*, 409-436.

Westerweel, J., & Scarano, F. (2005). Universal outlier detection for PIV data. *Experiments in Fluids*, *39*, 1096-1100.

White, F. (2006). *Viscous fluid flow.* McGraw-Hill.

Yuki, K., Hasegawa, S., Sato, T., Hashizume, H., Aizawa, K., & Yamano, H. (2011). Matched refractive-index PIV visualization of complex flow structure in a three-dimentionally connected dual elbow. *Nuclear Engineering and Design*, *241*, 4544-4550.

Zhao, T., Zhang, J., & Ma, L. (2011). A general structural design methodology for multi-hole orifices and its experimental application. *Journal of Mechanical Science and Technology*, *25*, 2237-2246.

Appendix A

Errors & uncertainty

This appendix discusses the various sources of errors in the present measurements and their effect on the measured data. Errors in experiments can be classified as:

- **Systematic errors:**
  Factors that make the measured value deviate constantly from the actual value are sources of systematic errors or bias erros. They can be reduced or even removed by changing the measurement approach.

- **Random errors:**
  These errors are random deviations from the true value. Random errors usually decrease by increasing the number of samples in a measurement.

A.1 Systematic errors

In the present PIV investigations, there are two main sources of systematic errors which are primarily a result of manufacturing constraints.

Effect of glass-pipe wall-curvature
For measurements in geometries with curved inner and outer surfaces, the difference in refractive index of the glass wall and water leads to an error in particle positions recorded on the camera due to refraction at the glass-water interface. To minimize this, pipe-geometries with extremely thin-walls are employed (van Doorne & Westerweel, 2007; Westerweel et al., 1996). This ensures that errors due to wall curvature are confined to regions very close to the boundary of the glass

Figure A.1 illustrates refraction due at the glass-water interface. If a light ray from a particle positioned at the central plane of the glass pipe makes an angle of incidence i_1 with respect to the normal, then from Snell's law:

$$\begin{aligned} n_1 \sin i_1 &= n_2 \sin r_1 \\ n_2 \sin r_1 &= n_1 \sin r_2 \end{aligned} \tag{A.1}$$

Where, n_1 and n_2 are the refractive indices of water and glass respectively. r_1 is the angle of refraction at the first water-glass interface and is also the angle of incidence at the glass-water interface. r_2 is the angle of the refracted ray at the glass-water interface. From the two equations it can be seen that the refracted ray is parallel to the original incident ray from the particle (i_1=r_2). However, there is a lateral shift between the two. The extent of this shift depends on the pipe-thickness and can be estimated easily using simple trigonometric relations.

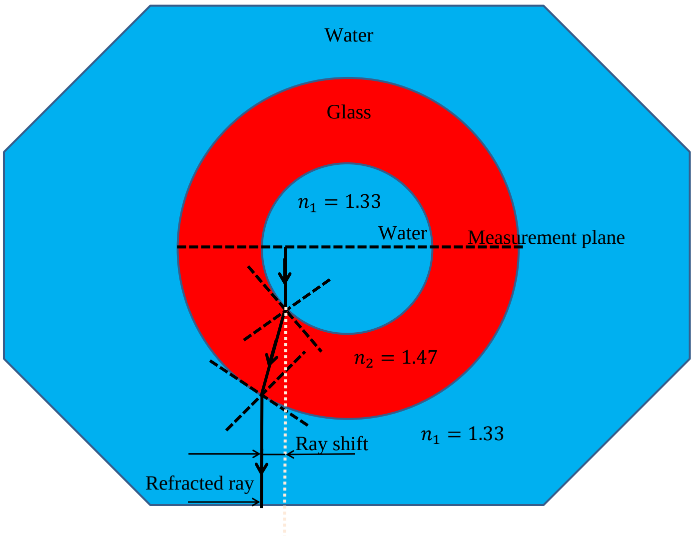

Figure A.1: Figure illustrating refraction of a light ray at the glass-water interface. Glass thickness exaggerated for illustration.

Assuming that the particles are present in the central plane of the glass pipe, then the lateral shift in the light rays arriving from the particles positioned at different radial locations can be computed. Figure A.2 shows this lateral shift as a function of the radial coordinate where the light ray originates. As expected, this deviation is less than the particle image size for about 95% of the pipe diameter. Errors due to refraction become prominent only very close to the glass wall (at a distance of 0.4 mm from the wall).

Effect of machining accuracy and user expertise

In experiments, the quality of results obtained depend strongly on the machining-accuracy with which different components of the setup are built. In addition to this, the ability of the experimentalist to ensure perfect experimental conditions are critical to a successful measurement.

In the present investigations, this condition is even more stringent as the order of magnitude of the components involved are very small (pipe diameter of 8.4 mm). This

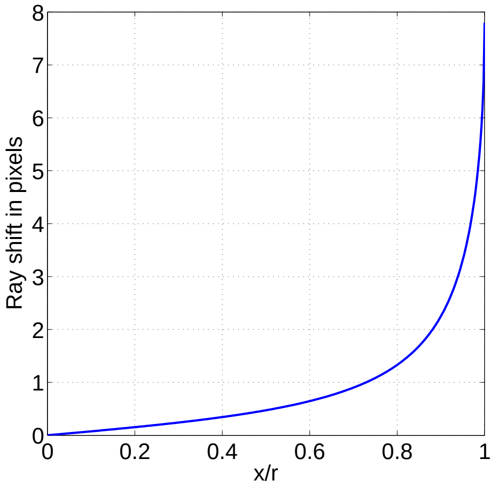

Figure A.2: Lateral shift (in pixels) of a light-ray as a function of the radial point it originates from, assuming all light rays originate from the pipe centerline as illustrated earlier in figure A.1.

means even a slight misalignment or improper positioning could lead to large errors, or an imperfectly manufactured orifice could yield incorrect results.

For example, figure A.3 presents the mean flow field downstream of orifice PIV-S10. Notice the large asymmetry in the mean flow field which is likely due to imperfect positioning of the orifice hole with respect to the pipe center line. In the present investigation, results from orifices indicating a large degree of asymmetry (namely orifice PIV-S10 and PIV-S11) haven't been reported.

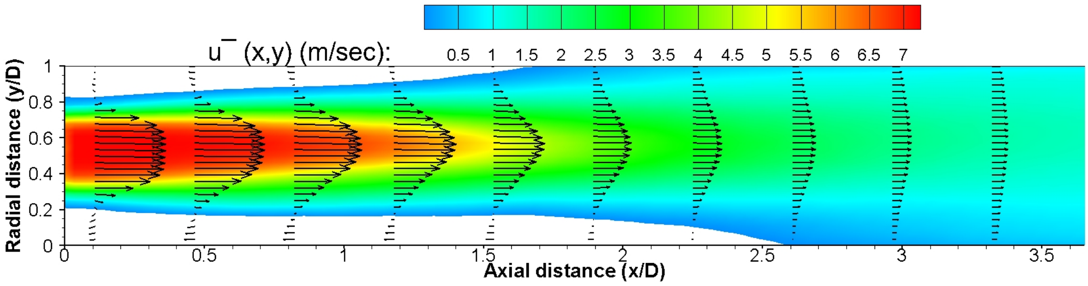

Figure A.3: Figure illustrating an asymmetric flow field. Regions with $\bar{u} < 0$ have been disabled to show the asymmetry in the reattachment points on the top and lower portion of the glass wall. Flow enters orifice PIV-S10 at $1\ m/sec$.

A.2 Random errors

This section discusses some sources of random-errors that effect the PIV data.

Peak locking
When images of the particles become too small ($d_p < 1$ pixel, then their displacements can not be measured with sub-pixel accuracy. As a result the measured displacements are biased towards integer values with position errors up to 0.5 pixels.

In the present study, its effect is determined by plotting a displacement histogram on *DaVis*. The peak locking effect was found to be negligible with the value of peak-lock$<<$ 0.1. Since the particle images are pre-processed before cross correlation, the effect of peak locking is reduced.

Effect of three-dimensionality (Out of plane motion)
An important source of error in planar PIV measurements of highly three-dimensional flows occurs due to out of plane motion of the particles. This causes the particles to escape from the interrogation windows during cross-correlation and the correlation peak signal strength decreases.

In the current experiments, it was observed that loss of particles occur near the shear layers of the orifice jet. Though the time-separation is kept sufficiently small, a few particle-pairs are inevitably lost due to the extremely high flow speed in the orifice jet. This is also reflected in the relatively low values of signal to noise ratio in these regions. Using elliptical shaped correlation windows along with sufficiently high seeding density, ensures that there are still sufficient number of particle pairs present. In places where spurious vectors are calculated, they are ultimately corrected using advanced post-processing techniques.

The effect of three-dimensionality is more severe on multiple hole orifices where 7 independent jets are present. The two dimensional nature of the present measurement does not take the out of plane motion into account.

A.3 Measurement uncertainty in PIV

A.3.1 Uncertainty in velocity

The underlying principle by which PIV operates, is that the velocity U in each interrogation window is determined using the displacement of particles Δx in time Δt, or

$$U = \frac{\Delta x}{\Delta t} \tag{A.2}$$

Using the error propagation formula, the total uncertainty for the velocity may be computed as:

$$\epsilon_U = \sqrt{(\epsilon_{lag})^2 + (\epsilon_{\delta x}.\partial U/\partial x)^2 + (\epsilon_{\delta t}.\partial U/\partial t)^2} \tag{A.3}$$

Where, the first term in equation A.3 is the error due to velocity lag between the fluid and the particle (see equation 2.17), and which for the present seeding particle, in water is sufficiently small to ignore. The last term in equation A.3 is the uncertainty in timing. For modern cameras and laser systems that were used in the present study, the time lag in synchronization of the laser and camera systems are in the order of nanoseconds and can thus be ignored as well.

The second term in equation A.3 represents the uncertainty in displacement, which result from the uncertainty in the determination of the magnification factor and uncertainty in the determination of displacement in pixels.

$$\epsilon_{\delta x} = \sqrt{\left(M.\epsilon_{\delta_{px}}\right)^2 + \left(\delta_{px}.\epsilon_M\right)^2} \tag{A.4}$$

The magnification factor was determined using a calibration plate (see section 6.4.2) with markings of size 0.1 mm which have a width of about 3 pixels. Thus, over a distance of 37 mm (or 1000 pixels), the total uncertainty is 6 pixels. This results in the uncertainty in magnification to be 1.47×10^{-4} $mm/pixel$ or a relative uncertainty of 0.6%.

Assuming that the particle image diameter is about 2-3 pixels, the uncertainty in determining the displacements is about 0.1 pixels (using uncertainty estimates provided by Raffel et al. (2007) for interrogation windows of size 32 × 32 pixels). For example, using the instantaneous result presented in section 7.3.1, in the core of the jet (where the displacements are the highest), displacements as high as 10 pixels are reached, or the relative uncertainty in displacements is 1% of the full-scale velocity.

By combining all these factors, this leads to a total uncertainty of $0.122 m/sec$ which is about 1.16% of the velocity in the core of the jet.

In the recirculation region, where the displacements are much lower $\approx 1 - 3$ pixels, the relative uncertainty in displacements ranges from 3% to 10%. This results in the total uncertainty of 3.05% to 10.01%.

A.3.2 Uncertainty in statistics

The relative uncertainty in the measured mean and fluctuation data can be estimated using the expressions given below:

$$\epsilon_\mu = k\frac{T.I}{\sqrt{N}} \tag{A.5}$$

$$\epsilon_\sigma = \frac{k}{\sqrt{N}} \tag{A.6}$$

Where $T.I$ is the turbulence intensity and N is the number of samples used. The variable k is the coverage factor that is related to the confidence level of the uncertainty estimate. On assuming that the velocity distribution is Gaussian with a confidence level of 95%, then $k = 1.96$.

Applying the above estimate in the results shown in section 7.3.2 where the mean is computed using 300 samples and the turbulence intensity is found to be 24%, results in a relative uncertainty $\epsilon_\mu = 2.7\%$ in the mean and the corresponding uncertainty in the estimation of RMS as $\epsilon_\sigma = 11\%$.

In the mean-reattachment calculations (section 7.5), the mean values are computed using all 3000 samples. In the auto-correlation function shown in figure 7.3, it was observed that in regions very close to the wall (radial distance $0.1D$) and at axial distances in the order of the mean reattachment length (2D-3D), the auto-correlation function falls below 0 only after about 20 samples. This means effectively only 1 in 20 samples contribute to the mean as statistically independent samples, or the effective data set size is 150 samples. Thus, the measurement uncertainty of the statistics in these regions are higher.

Appendix B

Testing conditions: Pressure measurements

This appendix lists the testing conditions used in pressure-measurements of orifice-plates. The last column of each table lists the pressure loss measured by the manometer. Note, the pressure losses occurring over the test section (see section 5.2) must be subtracted from these values before arriving at the loss-coefficient results presented in section 5.3 and 5.4.

B.1 Single-hole orifice plate testing conditions

Trial number	Flow speed, U_p (m/sec)	Re_p	Re_h	Pressure loss (bar)
1	0.46	4132	18593	0.626
2	0.62	5569	25060	1.249
3	0.7	6287	28293	1.45
4	0.8	7186	32335	1.875
5	0.87	7814	35165	2.433
6	0.93	8353	37590	2.88
7	1	8982	40419	3.5
8	1.1	9880	44461	4.33
9	1.17	10509	47290	5.075
10	1.24	11138	50120	5.75

Table B.1: Testing conditions and pressure loss values of plate S1 with $\beta = 5\%$ and $t/d_h = 0.5$.

Trial number	Flow speed, U_p (m/sec)	Re_p	Re_h	Pressure loss (bar)
1	0.46	4132	12395	0.227
2	0.56	5030	15090	0.333
3	0.7	6287	18862	0.53
4	0.93	8353	25060	0.931
5	1.17	10509	31527	1.462
6	1.3	11677	35030	1.803
7	1.4	12575	37725	2.081
8	1.63	14641	43922	2.81
9	1.86	16707	50120	3.64
10	1.87	16796	50389	3.692
11	2	17964	53892	4.201
12	2.25	20210	60629	4.886
13	2.5	22455	67365	5.823

Table B.2: Testing conditions and pressure loss values of plate S2 with $\beta = 11\%$ and $t/d_h = 0.5$.

Trial number	Flow speed, U_p (m/sec)	Re_p	Re_h	Pressure loss (bar)
1	0.46	4132	9296	0.15
2	0.7	6287	14147	0.329
3	0.74	6647	14955	0.361
4	0.93	8353	18795	0.544
5	1.17	10509	23645	0.838
6	1.24	11138	25060	0.926
7	1.4	12575	28293	1.149
8	1.63	14641	32942	1.533
9	1.73	15539	34963	1.718
10	1.87	16796	37792	1.988
11	2	17964	40419	2.245
12	2.25	20210	45472	2.793
13	2.47	22186	49918	3.318
14	2.5	22455	50524	3.4
15	3	26946	60629	4.767

Table B.3: Testing conditions and pressure loss values of plate S3 with $\beta = 20\%$ and $t/d_h = 0.5$.

Trial number	Flow speed, U_p (m/sec)	Re_p	Re_h	Pressure loss (bar)
1	0.7	6287	11317	0.274
2	0.93	8353	15036	0.451
3	1.17	10509	18916	0.691
4	1.4	12575	22635	0.955
5	1.55	13922	25060	1.153
6	1.63	14641	26353	1.258
7	1.87	16796	30234	1.608
8	2	17964	32335	1.811
9	2.17	19491	35084	2.129
10	2.25	20210	36377	2.259
11	2.5	22455	40419	2.722
12	3	26946	48503	3.751
13	3.1	27844	50120	3.905

Table B.4: Testing conditions and pressure loss values of plate S4 with $\beta = 31\%$ and $t/d_h = 0.5$.

Trial number	Flow speed, U_p (m/sec)	Re_p	Re_h	Pressure loss (bar)
1	0.46	4132	9296	0.149
2	0.7	6287	14147	0.338
3	0.93	8353	18795	0.58
4	1.17	10509	23645	0.873
5	1.4	12575	28293	1.194
6	1.63	14641	32942	1.598
7	1.87	16796	37792	2.07
8	2	17964	40419	2.343
9	2.25	20210	45472	2.901
10	2.5	22455	50524	3.513
11	2.75	24701	55576	4.199
12	3	26946	60629	4.935

Table B.5: Testing conditions and pressure loss values of plate S6 with $\beta = 20\%$ and $t/d_h = 0.125$.

Trial number	Flow speed, U_p (m/sec)	Re_p	Re_h	Pressure loss (bar)
1	0.46	4132	9296	0.152
2	0.7	6287	14147	0.314
3	0.93	8353	18795	0.51
4	1.17	10509	23645	0.77
5	1.4	12575	28293	1.069
6	1.63	14641	32942	1.402
7	1.87	16796	37792	1.82
8	2	17964	40419	2.053
9	2.25	20210	45472	2.568
10	2.5	22455	50524	3.097
11	2.75	24701	55576	3.671
12	3	26946	60629	4.332

Table B.6: Testing conditions and pressure loss values of plate S7 with $\beta = 20\%$ and $t/d_h = 0.625$.

B.2 Multi-hole orifice plate testing conditions

Trial number	Flow speed, U_p (m/sec)	Re_p	Re_h	Pressure loss (bar)
1	0.7	6287	5389	0.315
2	0.93	8353	7160	0.538
3	1.17	10509	9008	0.831
4	1.4	12575	10778	1.135
5	1.63	14641	12549	1.503
6	1.87	16796	14397	1.935
7	1.95	17515	15013	2.073
8	2	17964	15398	2.17
9	2.25	20210	17322	2.748
10	2.5	22455	19247	3.368
11	2.6	23353	20017	3.602
12	2.75	24701	21172	4.028
13	2.92	26228	22481	4.48
14	3	26946	23097	4.75

Table B.7: Testing conditions and pressure loss values of plate M3 with $\beta = 19.4\%$ and $t/d_h = 0.5$.

Trial number	Flow speed, U_p (m/sec)	Re_p	Re_h	Pressure loss (bar)
1	0.7	6287	4042	0.264
2	0.93	8353	5370	0.442
3	1.17	10509	6756	0.66
4	1.4	12575	8084	0.916
5	1.63	14641	9412	1.211
6	1.87	16796	10798	1.558
7	2	17964	11548	1.762
8	2.25	20210	12992	2.154
9	2.5	22455	14435	2.596
10	2.6	23353	15013	2.799
11	2.75	24701	15879	3.069
12	3	26946	17322	3.603
13	3.5	31437	20210	4.798

Table B.8: Testing conditions and pressure loss values of plate M4 with $\beta = 35\%$ and $t/d_h = 0.5$.

Trial number	Flow speed, U_p (m/sec)	Re_p	Re_h	Pressure loss (bar)
1	0.7	6287	5389	0.338
2	0.93	8353	7160	0.576
3	1.17	10509	9008	0.886
4	1.4	12575	10778	1.235
5	1.63	14641	12549	1.622
6	1.87	16796	14397	2.112
7	1.95	17515	15013	2.279
8	2	17964	15398	2.402
9	2.25	20210	17322	2.971
10	2.5	22455	19247	3.62
11	2.6	23353	20017	3.898
12	2.75	24701	21172	4.346
13	2.92	26228	22481	4.856
14	3	26946	23097	5.106

Table B.9: Testing conditions and pressure loss values of plate M5 with $\beta = 19\%$ and $t/d_h = 0.33$.

Trial number	Flow speed, U_p (m/sec)	Re_p	Re_h	Pressure loss (bar)
1	0.7	6287	5389	0.308
2	0.93	8353	7160	0.522
3	1.17	10509	9008	0.783
4	1.4	12575	10778	1.082
5	1.63	14641	12549	1.432
6	1.87	16796	14397	1.848
7	1.95	17515	15013	1.984
8	2	17964	15398	2.089
9	2.25	20210	17322	2.585
10	2.5	22455	19247	3.121
11	2.6	23353	20017	3.37
12	2.75	24701	21172	3.727
13	2.92	26228	22481	4.155
14	3	26946	23097	4.352

Table B.10: Testing conditions and pressure loss values of plate M6 with $\beta = 19\%$ and $t/d_h = 1.33$.

Trial number	Flow speed, U_p (m/sec)	Re_p	Re_h	Pressure loss (bar)
1	0.7	6287	3309	0.322
2	0.93	8353	4396	0.534
3	1.17	10509	5531	0.82
4	1.4	12575	6618	1.126
5	1.63	14641	7706	1.49
6	1.87	16796	8840	1.909
7	2	17964	9455	2.162
8	2.25	20210	10637	2.703
9	2.5	22455	11818	3.29
10	2.75	24701	13000	3.873
11	3	26946	14182	4.529
12	3.2	28743	15128	5.133

Table B.11: Testing conditions and pressure loss values of plate M10 with $\beta = 19\%$ and $t/d_h = 1.33$.

Trial number	Flow speed, U_p (m/sec)	Re_p	Re_h	Pressure loss (bar)
1	0.7	6287	3309	0.315
2	0.93	8353	4396	0.537
3	1.17	10509	5531	0.82
4	1.4	12575	6618	1.13
5	1.63	14641	7706	1.495
6	1.87	16796	8840	1.92
7	2	17964	9455	2.157
8	2.25	20210	10637	2.682
9	2.5	22455	11818	3.255
10	2.75	24701	13000	3.852
11	3	26946	14182	4.473
12	3.2	28743	15128	5.06

Table B.12: Testing conditions and pressure loss values of plate M11 with $\beta = 19\%$ and $t/d_h = 3.33$.

Appendix C

Testing conditions: Velocity measurements

This appendix lists the testing conditions of all orifice plates that were used during the PIV investigations.

C.1 Single-hole orifice plate testing conditions

Double-frame, frame-straddling mode (DF) at 1500 Hz

Trial Number	Flow speed, U_p (m/sec)	Re_p	Hole velocity, U_h (m/sec)	Re_h	Time separation Δt (μs)
1	0.5	4192	4.5	12575	66
2	0.6	5030	5.4	15090	55
3	0.75	6287	6.75	18862	44
4	1	8383	9	25150	33

Table C.1: Testing conditions for the plate PIV-S2 with $\beta = 11\%$ and $t/d_h = 0.5$.

Trial Number	Flow speed, U_p (m/sec)	Re_p	Hole velocity, U_h (m/sec)	Re_h	Time separation Δt (μs)
1	0.5	4192	2.44	9266	121
2	0.67	5617	3.27	12416	91
3	0.75	6287	3.66	13899	81
4	0.81	6790	3.96	15010	75
5	1	8383	4.89	18531	61
6	1.25	10479	6.11	23164	49
7	1.5	12575	7.33	27797	40
8	1.75	14671	8.55	32430	35
9	2	16766	9.77	37063	30

Table C.2: Testing conditions for the plate PIV-S3 with $\beta = 20\%$ and $t/d_h = 0.5$.

Trial Number	Flow speed, U_p (m/sec)	Re_p	Hole velocity, U_h (m/sec)	Re_h	Time separation Δt (μs)
1	0.5	4192	1.67	7654	178
2	0.75	6287	2.50	11481	118
3	0.82	6874	2.73	12553	108
4	0.98	8216	3.27	15002	91
5	1	8383	3.33	15309	89
6	1.21	10144	4.03	18523	73
7	1.25	10479	4.17	19136	71
8	1.5	12575	5.00	22963	59
9	1.63	13665	5.44	24953	55
10	1.75	14671	5.84	26790	51
11	2	16766	6.67	30617	44
12	2.25	18862	7.50	34444	39

Table C.3: Testing conditions for the plate PIV-S4 with $\beta = 30\%$ and $t/d_h = 0.5$.

Trial Number	Flow speed, U_p (m/sec)	Re_p	Hole velocity, U_h (m/sec)	Re_h	Time separation Δt (μs)
1	1	8383	1.67	10834	177
2	1.15	9641	1.92	12459	154
3	1.39	11653	2.32	15059	128
4	1.5	12575	2.51	16251	118
5	1.71	14335	2.86	18526	104
6	2	16766	3.34	21667	89

Table C.4: Testing conditions for the plate PIV-S5 with $\beta = 60\%$ and $t/d_h = 0.5$.

C.2 Multiple-hole orifice plate testing conditions

Double-frame, frame-straddling mode (DF) at 1500 Hz

Trial Number	Flow speed, U_p (m/sec)	Re_p	Hole velocity, U_h (m/sec)	Re_h	Time separation Δt (μs)
1	0.50	4192	2.57	3593	115
2	0.75	6287	3.86	5389	77
3	1	8383	5.14	7186	58
4	1.25	10479	6.43	8982	46
5	1.5	12575	7.71	10778	38
6	1.75	14671	9.0	12575	33
7	2	16766	10.29	14371	29

Table C.5: Testing conditions for the 7-hole, multi-hole orifice plate PIV-M1 with $\beta = 19\%$ and $t/d_h = 1.07$.

C.3 Additional test conditions

Single-frame, time-series mode (SF)

Plate label	Flow speed, U_p (m/sec)	Re_p	Hole velocity, U_h (m/sec)	Re_h	Sampling frequency, f_s (kHz)
PIV-S3	0.5	4192	2.44	9266	10
PIV-S3	0.75	6287	3.66	13900	10
PIV-S3	1	8383	4.88	18531	12.5
PIV-S4	0.5	4192	1.67	7654	6
PIV-M1	0.5	4192	2.57	3593	9
PIV-M1	7.5	6287	3.86	5389	12.5

Table C.6: Sampling frequency for flow conditions where images were acquired using single-frame, time-series mode.